



Nanostructured electrodes for high-performance and durable solid oxide cells

Tong, Xiaofeng

Publication date:
2019

Document Version
Publisher's PDF, also known as Version of record

[Link back to DTU Orbit](#)

Citation (APA):
Tong, X. (2019). *Nanostructured electrodes for high-performance and durable solid oxide cells*. Technical University of Denmark.

General rights

Copyright and moral rights for the publications made accessible in the public portal are retained by the authors and/or other copyright owners and it is a condition of accessing publications that users recognise and abide by the legal requirements associated with these rights.

- Users may download and print one copy of any publication from the public portal for the purpose of private study or research.
- You may not further distribute the material or use it for any profit-making activity or commercial gain
- You may freely distribute the URL identifying the publication in the public portal

If you believe that this document breaches copyright please contact us providing details, and we will remove access to the work immediately and investigate your claim.

Nanostructured electrodes for high-performance and durable solid oxide cells

Xiaofeng Tong

October 2019

Frederiksborgvej 399
DK - 4000 Roskilde
Denmark
www.energy.dtu.dk

Technical University
of Denmark



Author

Xiaofeng Tong

Department of Energy Conversion and Storage

Technical University of Denmark

Main Supervisor

Ming Chen

Senior scientist

Department of Energy Conversion and Storage

Technical University of Denmark

Co-supervisors

Peter Vang Hendriksen

Professor, Head of section

Department of Energy Conversion and Storage

Technical University of Denmark

Simona Ovtar[‡]

Postdoc

Department of Energy Conversion and Storage

Technical University of Denmark

[‡]Engineer, OFS Fitel Denmark

Preface

This thesis is submitted to the Technical University of Denmark as partial fulfillment of the requirements for obtaining the Ph.D. degree. The work was carried out from November 2016 to October 2019 at the Department of Energy Conversion and Storage (DTU Energy), under the main supervision of Senior Scientist Ming Chen, and the co-supervision of Prof. Peter Vang Hendriksen and Dr. Simona Ovtar. The work was partly funded by EUDP through the project “Efficient Power2Gas Combining SOEC and Biomass Gasification” (EUDP no. 64017-0011) and Innovation Fund Denmark through the project “Synfuel” (4106-00006B). The Ph.D. project was also supported by DTU Energy and the China Scholarship Council. A three-month external stay from March 2019 to May 2019 took place at the University of Twente in the group of Prof. Henny J.M. Bouwmeester thanks to the additional funding provided by the Otto Mønstedts Fond.

DTU Risø Campus, Roskilde, October 31, 2019

 Xiaofeng Tong

Acknowledgements

I would like to express my sincere gratitude to those who contributed to this thesis and/or supported me in this amazing “journey”.

First and foremost, I would like to thank my principal supervisor Dr. Ming Chen for making it all happen; for picking me up at the airport on the first day; for guiding, supporting, and encouraging me in these three years. In particular, Ming helped a lot with planning the study while also giving me plenty of room to explore. I have really learned and enjoyed under Ming’s supervision.

Similar gratitude shall go to my co-supervisors: Prof. Peter Vang Hendriksen and Dr. Simona Ovtar. Thank Peter for his guidance and support on my experiments, and driving a push to improve English. Peter always gave constructive and comprehensive advice on the manuscripts I sent and made many descriptions more professional and precise. Thank Simona for teaching me how to do experiments hand by hand in the lab especially for infiltration, and providing me an interesting research topic to continue.

Special thanks go to Prof. Anne Hauch, who helped me greatly in many aspects, from teaching me the course of “SOFC and SOEC introduction” at the beginning of my Ph.D. to sharing with me the use of software “Ravdav” for electrochemical data analysis and her expertise in cell degradation analysis based on electrochemical impedance spectroscopy. I would also like to thank Dr. Christopher R. Graves and Dr. Theis Løye Skafte for assistance in using “Ravdav”.

Besides, I thank the following colleagues at DTU for supporting my experiments and for insightful discussions.

- Karen Brodersen, Lene Knudsen, and Yu Xu — for help with cell fabrication. Karen supplied me with half-cells; Lene printed the oxygen electrodes and contact layers for me. Yu synthesized the amazing CGO nanoparticles for me.

- Henrik Henriksen, Søren Koch, Mahbooba Davodi, and Jens F. S. Borchsenius — for help with cell testing. Especially Henrik, he supported all of my tests and was always around when I needed help.
- Ebtisam Abdellahi, Janet Jonna Bentzen, and Søren Bredmose Simonsen — for help with microscopy characterization.
- Jette Iversen — for help with Brunauer-Emmett-Teller measurement.
- Dordije Tripkovic — for help with electrical conductivity relaxation measurements.
- Annelise Mikkelsen, June Ruddie, and Henrik Paulsen — for other support in the lab.
- Mogens Bjerg Mogensen, Bhaskar Reddy Sudireddy, Xiufu Sun, Belma Talic, Astri Bjørnetun Haugen — for insightful discussions.

Without their contributions, many of the outcomes in this thesis would not have been achieved.

Many thanks to Prof. Henny J.M. Bouwmeester at the University of Twente for hosting me as a guest for three months and to Jason and Zainab who are very helpful during my staying there.

I would especially like to thank our awesome secretary Heidi Adler Berggren, who greatly helped with the distracting things and enabled me to focus on scientific work. There is always a big smile and encouragement from Heidi every time when she comes by my office.

Finally, I owe my deepest thanks to my family; my grandparents for taking care of me when I was a child; my parents for supporting and encouraging me to do what I like even though they have no idea about my research; my beloved wife Yongfang for love, patience, and support, and for joining me from China to Denmark.

Abstract

Electrical energy is essential for maintaining our standard of living. The rapid growth in electricity generation from intermittent renewable solar and wind sources creates a need for affordable large-scale energy storage to balance the supply-demand mismatch in the grid. One promising technology to address this energy storage challenge is solid oxide cells (SOCs). They can be operated either in electrolysis mode (as solid oxide electrolysis cells, SOECs) to convert H₂O and/or CO₂ into H₂ and/or CO using renewable electricity, or in fuel-cell mode (as solid oxide fuel cells, SOFC) to generate electricity on demand using the fuels produced. However, the widespread commercialization of the SOC technology is still impeded by high cost and insufficient long-term durability. In particular, the technology of operating SOCs in electrolysis mode is less mature, in which the electrodes of SOC cells often suffer from considerable degradation during continuous electrolysis operation.

The focus of this thesis is the development of high-performance and durable SOCs by designing nanostructured electrodes via infiltration. Efforts are devoted to three aspects: i) improving the performance of electrodes for intermediate-temperature (600–750 °C) operation. Operating SOCs at intermediate temperatures can not only provide choice for using cheaper interconnects and seals thus reducing system cost but also avoid some issues related to materials incompatibility and heat management; ii) enhancing the durability of electrodes, particularly for the fuel electrodes during electrolysis operation under high current densities. The high current density enables a high gas production rate and lowers the capital costs; iii) the scale-up of the above progress, which is very important for practical applications. Throughout the thesis, the electrochemical performance and durability of the developed electrodes were mainly evaluated on full cells through electrochemical impedance spectroscopy (EIS), polarization curves, and galvanostatic tests. The analysis of EIS data was performed by fitting with equivalent circuit model using complex-nonlinear-least-squares (CNLS) regression and calculating the distribution of relaxation time (DRT).

First, different from most studies on infiltrated SOCs carried out on button cells with a small active area, 12.5 × 12.5 cm² fuel-electrode-supported SOCs with La_{0.6}Sr_{0.4}CoO_{3-δ} (LSC) infiltrated gadolinia-doped ceria (CGO) oxygen electrodes were prepared. The

electrochemical performance of the resulting SOCs was examined at $4 \times 4 \text{ cm}^2$ level (active area). The cell delivered favorable performance at $750 \text{ }^\circ\text{C}$ under high gas/steam utilization, e.g., a power density of 1.08 W cm^{-2} at 0.6 V in fuel cell mode and a current density of -1.07 A cm^{-2} at 1.3 V in electrolysis mode. These results highlight the potential of using infiltration to produce large-size, high-performance SOCs. However, the cell showed significant degradation when operated at -0.5 A cm^{-2} for steam electrolysis, and the major degradation was found to be from the Ni/ yttria-stabilized zirconia (YSZ) fuel electrode.

The Ni/YSZ electrode is the most commonly used and best-performing fuel electrode in SOCs, while its degradation during electrolysis operation has been an ongoing challenge. Secondly, in order to enhance the durability of Ni/YSZ electrode, an approach of surface modification of the Ni/YSZ electrode by coating nano-sized CGO electrocatalysts via infiltration was developed. After modification, the cell durability was dramatically improved, reducing degradation rate from 0.565 to 0.024 V kh^{-1} , when tested at -1.00 A cm^{-2} and $750 \text{ }^\circ\text{C}$ for steam electrolysis. The mechanisms of the Ni/YSZ electrode degradation and of the mitigation via surface modification at these conditions were discussed and speculated. To enable a sufficient porosity in the Ni/YSZ electrode structure for infiltration and to avoid the chemical expansion of the CGO barrier layer and the decomposition of oxygen electrode material during reduction, the full cell was pre-reduced with a “two-atmosphere-reduction”, i.e., the fuel electrode side was exposed to reducing atmosphere while the oxygen electrode was exposed to air. This was achieved using an in-house built test rig which is well suited for the purpose if only a small number of cells is considered, but not well suited for mass production. To fit the upscaling requirement, the aforementioned infiltration approach was further simplified by replacing the complicated “two-atmosphere-reduction” procedure with a facile “one-atmosphere-reduction”, which can well be carried out in furnace during the cooling of the cell after the final sintering step.

Finally, considering that cobalt-containing materials often suffer from various issues when employed as oxygen electrodes, a nanoengineered $\text{La}_{0.6}\text{Sr}_{0.4}\text{FeO}_{3-\delta}$ (LSF)-based oxygen electrode was developed by applying a nanoporous hybrid catalyst coating composed of nanoparticles of CGO and PrO_x . Different from the conventional infiltration with a precursor of metal nitrate, here a mixture solution of colloidal CGO nanocrystals and $\text{Pr}(\text{NO}_3)_3$ was used for infiltration to enable this designed nanoengineered architecture. The excellent activity and durability of the resulting hybrid-catalyst-coated LSF electrode were

demonstrated for both fuel-cell and electrolysis operation. In particular, when applying this oxygen electrode on a CGO-modified Ni/YSZ fuel-electrode-supported cell, stable operation at 650 °C under -0.5 A cm^{-2} with cell voltage close to 1.3 V was achieved. The results achieved in this thesis demonstrate the great potential of boosting the performance and durability of SOCs via surface modification with nano electrocatalysts.

Papers included in the thesis

Paper I. Large-area Reversible Planar Solid Oxide Cells with $\text{La}_{0.6}\text{Sr}_{0.4}\text{CoO}_{3-\delta}$ Infiltrated Oxygen Electrodes for Electricity Generation and Hydrogen Production

Xiaofeng Tong, Simona Ovtar, Karen Brodersen, Peter Vang Hendriksen, Ming Chen

As manuscript to be submitted

Paper II. A $4 \times 4 \text{ cm}^2$ Nano-Engineered Solid Oxide Electrolysis Cell for Efficient and Durable Hydrogen Production

Xiaofeng Tong, Simona Ovtar, Karen Brodersen, Peter Vang Hendriksen, Ming Chen

ACS Appl. Mater. Interfaces, 2019,11, 29, 25996-26004

Paper III. Development of Solid Oxide Electrolysis Cells for Hydrogen Production at High Current Densities

Xiaofeng Tong, Peter Vang Hendriksen, Anne Hauch, Ming Chen

ECS Transactions 91.1 (2019): 2433-2442.

Paper IV. A Scalable, Infiltration-Based Approach to Improving the Durability of Ni/YSZ Electrodes for Solid Oxide Cells

Xiaofeng Tong, Peter Vang Hendriksen, Anne Hauch, Xiufu Sun, Ming Chen

As manuscript to be submitted

Paper V. Promotion of Oxygen Reduction and Evolution by Applying a Nanoengineered Hybrid Catalyst on Cobalt free Electrodes for Solid Oxide Cells

Xiaofeng Tong, Yu Xu, Dordije Tripkovic, Peter Vang Hendriksen, Wolff-Ragnar Kiebach, Ming Chen

As manuscript to be submitted

Contents

Preface	i
Acknowledgements	ii
Abstract	v
Papers included in the thesis	viii
Contents	ix
Chapter 1 Introduction	1
1.1 Motivation	1
1.2 Solid oxide cells	3
1.3 Infiltration in SOCs.....	7
1.4 Electrochemical impedance spectroscopy	8
1.5 Objective and scope of the thesis	13
Chapter 2 Solid oxide cells with $\text{La}_{0.6}\text{Sr}_{0.4}\text{CoO}_{3-\delta}$ infiltrated oxygen electrodes for electricity generation and hydrogen production	21
Abstract	21
2.1 Introduction.....	21
2.2 Experimental	24
2.3 Results and discussion.....	26
2.4 Conclusion	38
Supplementary information.....	39
Chapter 3 Nanoengineered solid oxide electrolysis cells for efficient and durable hydrogen production	41
Abstract	41
3.1 Introduction.....	41
3.2 Results and discussion.....	44
3.3 Conclusion	58
3.4 Experimental	58
Supplementary information.....	61

Chapter 4 An up-scalable, infiltration-based approach for improving the durability of Ni/YSZ electrodes for solid oxide cells	71
Abstract	71
4.1 Introduction.....	72
4.2 Experimental	74
4.3 Results and discussion.....	75
4.4 Conclusion	89
Chapter 5 Promotion of oxygen reduction and evolution by applying a nanoengineered hybrid catalyst on cobalt free electrodes for solid oxide cells	91
Abstract	91
5.1 Introduction.....	92
5.2 Results and discussion.....	94
5.3 Conclusion	106
5.4 Experimental	107
Supplementary information.....	110
Chapter 6 Conclusion and outlook	113
6.1 Conclusion	113
6.2 Outlook.....	115
Bibliography.....	117

CHAPTER 1

Introduction

1.1 Motivation

Electrical energy is essential for maintaining our standard of living. The global electricity generation has increased by ~20% from 20,131 billion kWh in 2010 to 24,104 billion kWh in 2017, with more than 60 % of electricity generated from fossil fuels (**Figure 1.1**). [1] This ongoing domination of fossil fuels in global electricity generation has contributed significantly to global greenhouse gas emissions. For example, considering only the coal-fired electricity generation, it is responsible for ~30% of global CO₂ emissions in 2018, reported by International Energy Agency. [2] The depletion of fossil fuels and the climate changes related to greenhouse gas emissions drives a transition towards fossil-free electricity generation, in which renewable energy sources such as solar and wind are expected to play an important role. As a result, the share of solar and wind-based renewables generation increased from ~6 % in 2016 to ~8 % in 2017, and it is expected to further increase to 34% in 2050. In particular, share of electricity from solar and wind energy achieved high levels in several countries in 2018, e.g., Denmark (51%), Uruguay (36%), Ireland (29%), Germany (26%) and Portugal (24%). [3]

It has been widely recognized that with the rising share of electricity generation from intermittent renewable solar and wind sources, affordable large-scale energy storage will be needed to balance the supply-demand mismatch in the grid. [4] Currently, world's total installed energy storage capacity is only 166.6 GW. More than 96% (160 GW) of capacity is provided by pumped-hydro, which can not be available widely due to the site-specific characteristic. [3] The rest of ~ 4 % is provided by electrochemical storage and thermal storage. Among the electrochemical storage, ~3 GW is provided by batteries, which are suited for short-term (e.g., hourly or daily) energy storage but less suited for longer-term

(e.g., seasonal). [3, 5] Therefore, a variety of other energy storage technologies are under development.

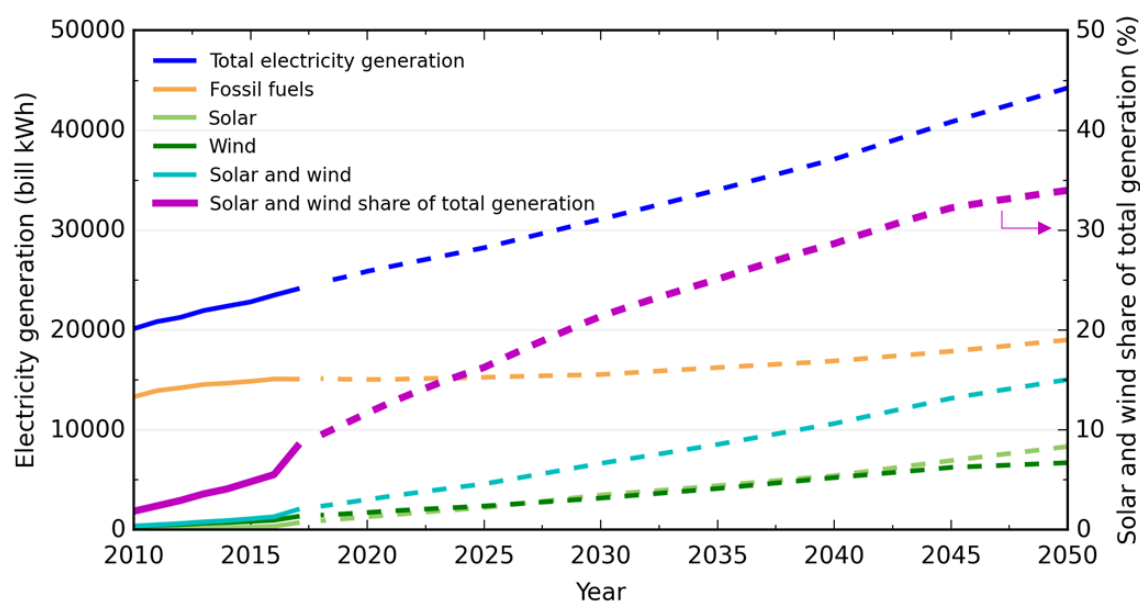


Figure 1.1: Global electricity generation, 2010-2050. Solid lines are the actual production quantities and dash lines are projections. Replotted from the International Energy Outlook 2019 database. [1]

As a promising technology to address the seasonal energy storage challenge, reversible solid oxide cells (SOCs) have received increasing attention in recent years. [5-8] They can be operated either in electrolysis mode (as solid oxide electrolysis cells, SOECs) to convert H_2O and/or CO_2 into H_2 and/or CO using excess renewable electricity, or in fuel-cell mode (as solid oxide fuel cells, SOFC) to generate electricity on demand using the fuels produced (**Figure 1.2**). [5, 9] Additionally, the produced H_2 and CO can be catalytically converted using well-known processes to produce easily storable fuels such as methanol and gasoline for the transportation sector. [10, 11] Compared to other electrochemical cells operated at low temperatures (typically 50–100 °C) such as alkaline electrochemical cells (AECs) and polymer electrolyte membrane cells (PEMCs), SOCs possess several attractive advantages because of their elevated operating temperatures (typically 600–900 °C). For example, when operated as electrolysis cells, high-temperature SOEC operation enables high efficiency at high fuel production rate. Besides, high operating temperature avoids using noble metal based catalysts (as for PEMCs) and enables utilizing a variety of waste heat sources. Despite these advantages, the commercialization of SOC technology is still impeded by high cost

and insufficient long-term durability. In particular, the development of SOCs for SOEC operation is much less mature than for SOFC operation.

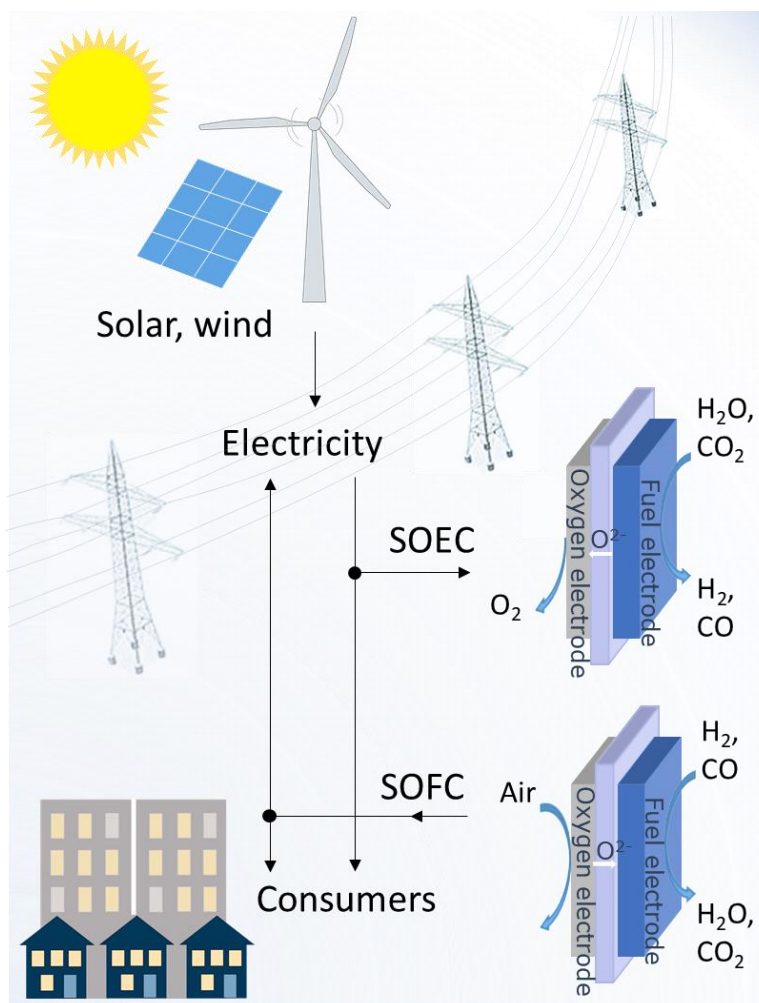


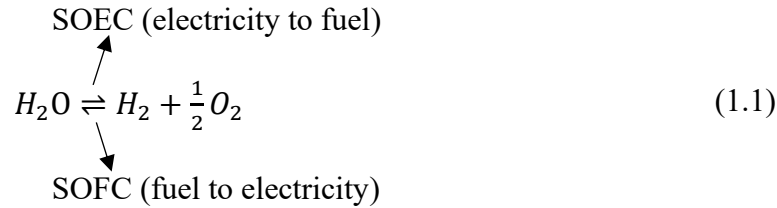
Figure 1.2: Schematic of the renewable electricity storage system based on solid oxide cells (SOCs).

1.2 Solid oxide cells

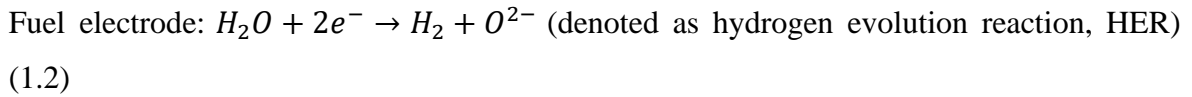
1.2.1 Principle of SOCs

A basic SOC cell consists of porous fuel and oxygen electrodes, separated by a dense, oxide ion conducting electrolyte (**Figure 1.2**). Yttria-stabilized zirconia (YSZ) is the most common electrolyte material; scandia-stabilized zirconia (SSZ), gadolinia-doped ceria (CGO or GDC) and perovskite structure oxides of strontium- and magnesium-doped lanthanum gallate

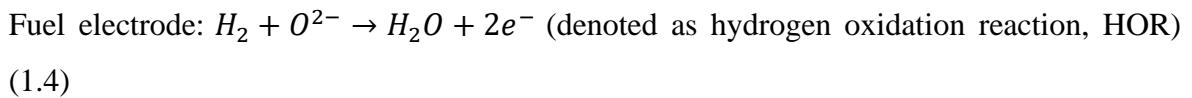
(LSGM) have also been investigated as electrolyte materials. [12] The principle of a reversible SOC operating on H_2O , O_2 , H_2 for either producing fuel or generating electricity can be described in generic terms as equation (1.1).



In SOEC mode, when the required potential is applied, H_2O molecules are split into H_2 and oxygen anions (O^{2-}) at the fuel electrode, and then oxygen anions pass through the electrolyte toward the oxygen electrode where they are subsequently oxidized to O_2 . The reactions in the fuel and oxygen electrodes can be expressed as:



In SOFC mode, O_2 molecules are reduced to O^{2-} anions at the oxygen electrode, and then O^{2-} anions pass through the electrolyte to the fuel electrode, where H_2 molecules are oxidized by these O^{2-} anions and the electrons are released, thus generating electricity. The reactions in the fuel and oxygen electrodes are reversed as compared to those in SOEC operation, and can be expressed as:



1.2.2 Oxygen electrode materials

The most studied oxygen electrodes in SOC are based on strontium-doped lanthanum manganite (LSM). These LSM-based electrodes have been reported with poor activity for both ORR and OER, limited by the pure electronic conducting nature of the LSM. Though LSM is usually mixed with YSZ to form a composite LSM/YSZ electrode, the cells with

such LSM/YSZ electrodes still require high operation temperatures (≥ 850 °C) to achieve applicable performance. As shown in **Table 1.1** (Page 15), when operated in SOEC mode, ~ -1.00 A cm⁻² is almost the highest reported current density for such cells at 1.3 V and 850 °C, and they have only limited performance below 800 °C. This high operating temperature results in several serious barriers for the practical application of SOC technology, such as high system and operating costs, as well as materials compatibility challenges. [13]

Beyond this performance limitation, the LSM-based electrodes also suffer from significant degradation when operated at high current densities in SOEC mode. For example, on a cell with a LSM/YSZ oxygen electrode, Graves et al. [7] reported a degradation rate of 0.952 V kh⁻¹ for a 420 h testing period at -1 A cm⁻² (the cell voltage increased from 1.33 V to 1.73 V, corresponding to an efficiency decrease from 96% to 75%). For a similar cell, even at -0.7 A cm⁻², Hartvigsen et al. [14] found an increase in the cell resistance from 0.50 to 0.62 Ω cm² for 300 h operation, corresponding to a cell voltage increase of approximately 20 % kh⁻¹. Regarding the degradation phenomena, a microstructural deterioration near the LSM/YSZ electrode – YSZ electrolyte interface, associated with cavity formation in the vicinity of the interface, oxidation of manganese ions and formation of manganese cation vacancies at LSM grains, has been reported [7, 15-22]. Graves et al. [7] found that this microstructural damage can be eliminated by using a reversible cycle with periods of 1 h in SOEC mode and 5 h in SOFC mode, but such a cycle does not fit the flexibility required for practical applications.

During the past decades, substantial efforts have been made in developing alternative oxygen electrode materials, leading to a shift from the electronic conducting LSM to mixed ionic-electronic conductors (MIECs). In particular, many cobalt-containing perovskite-type oxides, such as La_{0.6}Sr_{0.4}Co_{0.2}Fe_{0.8}O_{3- δ} (LSCF) [23, 24], La_{0.6}Sr_{0.4}CoO_{3- δ} (LSC) [25], Sm_{0.5}Sr_{0.5}CoO_{3- δ} (SSC) [26], Ba_{0.5}Sr_{0.5}Co_{0.8}Fe_{0.2}O_{3- δ} (BSCF) [27], and PrBa_{0.5}Sr_{0.5}Co_{1.5}Fe_{0.5}O_{5+ δ} (PBSCF) [28], have been developed, and showed favorable catalytic activity at intermediate temperatures (**Table 1.2**, Page 16). For example, a peak power density of 1.05 W cm⁻² in SOFC mode and a current density of -0.90 A cm⁻² at 1.3 V in SOEC mode were reported on a cell with LSCF/gadolinia-doped ceria (CGO) composite electrode at 750 °C. [29] However, these cobalt-containing materials often suffer from

various problems, such as large thermal expansion mismatch with commonly used electrolytes, chemical instability for long-term operation and the volatility and diffusivity of cobalt during the high-temperature sintering process causing various cell fabrication issues.[30-32] For example, electrode performance degradation has been observed on LSCF electrode due to Sr segregation near surfaces or interfaces, attributed to the electrostatic attraction of the negatively charged A-site dopants by the positively charged oxygen vacancies enriched on the surface. [30, 33] There have also been numerous reports on using Ruddlesden-Popper type oxides such as $\text{Ln}_2\text{NiO}_{4+\delta}$ ($\text{Ln} = \text{La}, \text{Nd}, \text{Pr}$) as oxygen electrode materials. [34-38] However, these Ruddlesden-Popper materials can be unstable under SOEC operation, which causes the degradation of electrodes. [38] For instance, the decomposition of $\text{La}_2\text{NiO}_{4+\delta}$ to high-order Ruddlesden-Popper $\text{La}_3\text{Ni}_2\text{O}_{7+\delta}$ and $\text{La}_4\text{Ni}_3\text{O}_{10+\delta}$ oxides has been reported during polarization at -500 mA cm^{-2} and $750 \text{ }^\circ\text{C}$ in SOEC mode. [38]

1.2.3 Fuel electrode materials

The most studied fuel electrode in SOCs is Ni/yttria-stabilized zirconia (YSZ) composite, which displays excellent activity for both the hydrogen oxidation reaction (HOR) in SOFC mode and hydrogen evolution reaction (HER) in SOEC mode. This Ni/YSZ electrode is now used successfully for SOFC operation with not only good performance but also satisfactory durability by a number of developers. However, the Ni/YSZ electrode experiences considerable degradation during continuous SOEC operation, particularly at high current densities. For state-of-the-art SOCs, with a configuration of the Ni/YSZ support | Ni/YSZ fuel electrode | YSZ electrolyte | CGO barrier layer | LSCF/CGO oxygen electrode, a degradation rate of 0.006 V kh^{-1} was observed during SOFC operation at 1 A cm^2 and $800 \text{ }^\circ\text{C}$, while more than one order of magnitude higher degradation rate of 0.105 V kh^{-1} was observed during SOEC operation under same conditions but at -1 A cm^2 . [39] Furthermore, even high degradation rate of 0.713 V kh^{-1} was reported at higher current density of -1.25 A cm^2 . [40] Regarding the degradation phenomena on Ni/YSZ electrodes, several different microstructural deteriorations have been reported, including poisoning by impurities, Ni coarsening and migration, destruction of the Ni-YSZ interface, and even formation of ZrO_2 nanoparticles on the Ni surface due to the reduction of YSZ. [41-52] In addition,

poisoning by silica containing impurities at the triple-phase boundaries (TPBs) of the Ni/YSZ electrode has also been reported. [6, 52]

Though MIEC oxides, such as $\text{La}_x\text{Sr}_{1-x}\text{Cr}_{0.5}\text{Mn}_{0.5}\text{O}_{3-\delta}$, [53-55] $\text{La}_{0.2}\text{Sr}_{0.8}\text{TiO}_{3+\delta}$, [56] $\text{La}_{0.4}\text{Sr}_{0.4}\text{Ni}_{0.06}\text{Ti}_{0.94}\text{O}_{3-\delta}$, [57] $\text{La}_{0.43}\text{Ca}_{0.37}\text{Ni}_{0.06}\text{Ti}_{0.94}\text{O}_{3-\delta}$, [58] and $\text{Sr}_2\text{Fe}_{1.5}\text{Mo}_{0.5}\text{O}_{6-\delta}$, [59, 60] have been explored as alternative fuel electrodes, the catalytic activity and electrical conductivity of these MIEC electrodes have not reached the levels observed for those of the Ni/YSZ electrodes, as shown in **Table 1.3** (Page 17). Accordingly, Ni/YSZ is still the most commonly used fuel electrode material, and it is thus important to enhance the durability of Ni/YSZ electrodes. Recently, Hauch et al. demonstrated that the Ni migration in Ni/YSZ electrode during SOEC operation can be effectively mitigated by a microstructure optimization, reducing the cell degradation rate from $\sim 0.250 \text{ V kh}^{-1}$ to $\sim 0.060 \text{ V kh}^{-1}$ when operating at -1 A cm^{-2} and $800 \text{ }^\circ\text{C}$. [44] However, further improvement in durability is required for the practical application.

1.3 Infiltration in SOCs

Infiltration, also known as impregnation, is a promising approach for preparing high-performance, nanostructured electrodes for SOCs. [61-63] As is schematically shown in **Figure 1.3**, an infiltration process generally involves three steps: i) preparation of porous electrode backbone, ii) injecting a liquid solution containing the stoichiometric metal salt precursors into the porous backbone, and iii) heat treatment to form desired active phases. [62, 63]

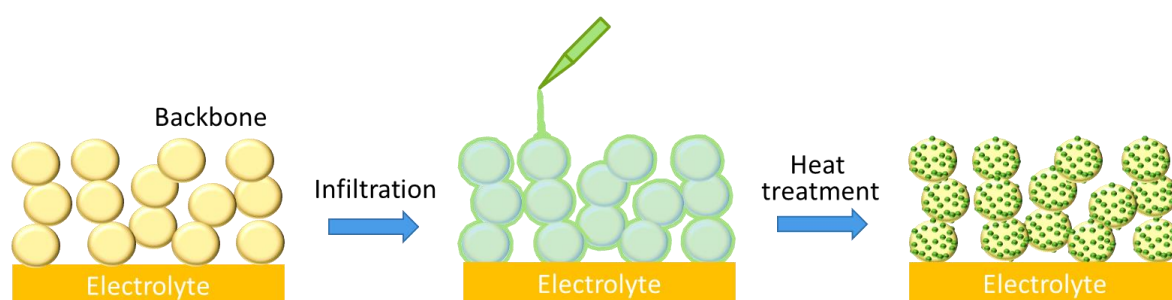


Figure 1.3: A schematic of a typical infiltration process

The mostly reported infiltration strategy is infiltration of MIEC electrode materials into electrolyte-based backbones such as YSZ, CGO, and LSGM. [64-75] This infiltration strategy offers several advantages in comparison with the conventional screen-printing technique which requires a high sintering temperature (typically ≥ 1000 °C) to make a strong bonding between electrolyte and electrode. First, the heat treatment in the infiltration process is generally performed at relatively low temperatures (typically 300–800 °C), issues of chemical compatibility such as detrimental chemical reactions and interdiffusion of MIEC electrode materials with electrolytes can be effectively avoided or significantly reduced. Furthermore, the nanostructure enabled by low-temperature heat treatment can effectively improve the catalytic activity of infiltrated electrodes. Thirdly, the issue of thermal expansion mismatch between the electrolyte and the MIEC electrode materials could also be mitigated because the MIEC catalysts are now deposited on the backbone as the form of nanoparticles.

Another strategy is surface modification of electrode with catalytically-active nanoparticles/coating via infiltration, which has received increasing attention in recent years. [76-81] This surface modification has been reported as an effective approach that can enhance not only the performance of electrodes but also the durability. For example, by modifying LSCF/CGO composite electrode with SSC nano-catalysts, the cell showed an improvement of peak power density from 1.05 to 1.62 W cm⁻² in fuel cell mode and an increase in current density from -0.9 to -1.80 A cm⁻² at 1.3 V in electrolysis mode [29]. A multi-phase catalyst coating not only dramatically reduced the R_p from 2.57 Ω cm² (for bare LSCF) to 0.312 Ω cm² at 600 °C but also enhanced the durability by suppressing surface Sr segregation. [79]

1.4 Electrochemical impedance spectroscopy

Electrochemical impedance spectroscopy (EIS) is a powerful technique for SOC diagnosis. It can be used for not only evaluation of cell performance but also understanding of cell

degradation mechanisms occurring during operation. The EIS principle and data analysis methods will be outlined briefly in the coming text.

1.4.1 EIS principle

Impedance can be defined as a complex resistance. EIS is measured by applying a small excitation to the cell and measuring its response. As shown in **Figure 1.4**, if a sinusoidal potential signal, $E(t) = E_0 \sin(\omega t)$, is applied for exciting a linear time-invariant (LTI) circuit system, the response to this potential will be a current response, $I(t) = I_0 \sin(\omega t + \varphi)$. This $I(t)$ has the same frequency (f) as $E(t)$ but a shifted phase (φ). ω is the radial frequency and the relationship between ω and f is $\omega = 2\pi f$.

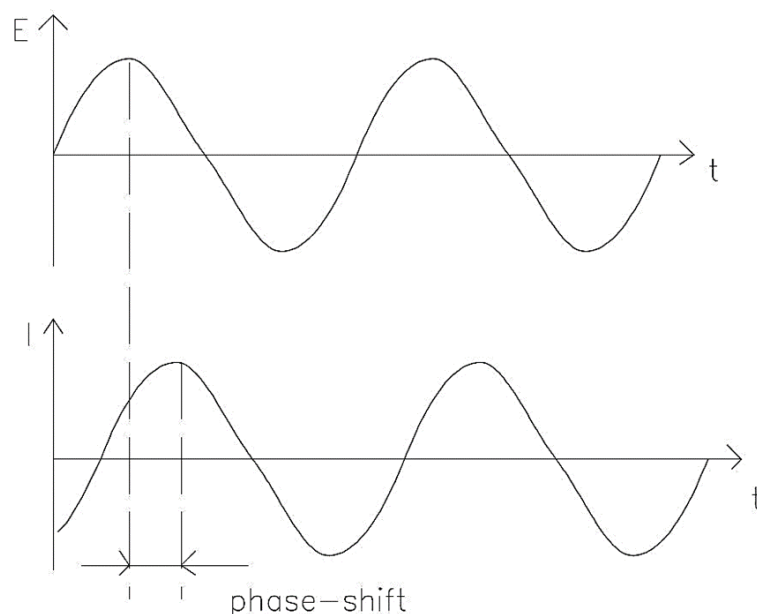


Figure 1.4: Sinusoidal Current Response in a Linear System. Reprinted from ref. [82]

Hence, analogous to Ohm's Law, the impedance is defined as the complex number Z with the expression:

$$Z = \frac{E(t)}{I(t)} = \frac{E_0 \sin(\omega t)}{I_0 \sin(\omega t + \varphi)} \quad (1.6)$$

Based on Euler's relationship, $\exp(j\varphi) = \cos\varphi + j\sin\varphi$, Z can be further expressed as follows: [83]

$$Z = Z_0 \exp(j\varphi) = Z_0(\cos\varphi + j\sin\varphi) = Z_R + jZ_{Im} \quad (1.7)$$

Where Z_R denotes the real part and Z_{Im} denotes the imaginary part. j is defined as $j^2 = -1$.

In SOC studies, the EIS measurement is usually realized by applying AC sinusoidal signals with amplitudes of a few mV or mA in a frequency range of 0.01 Hz to 1.0 MHz. The two most common ways of presenting the EIS data are Nyquist plot and Bode plot shown in **Figure 1.5**. In the Nyquist plot, the intercept with the real axis at high frequency represents the ohmic resistance (R_{ohm}), and the difference between the high and low frequency intercepts represents the total electrode polarization resistance (R_p).

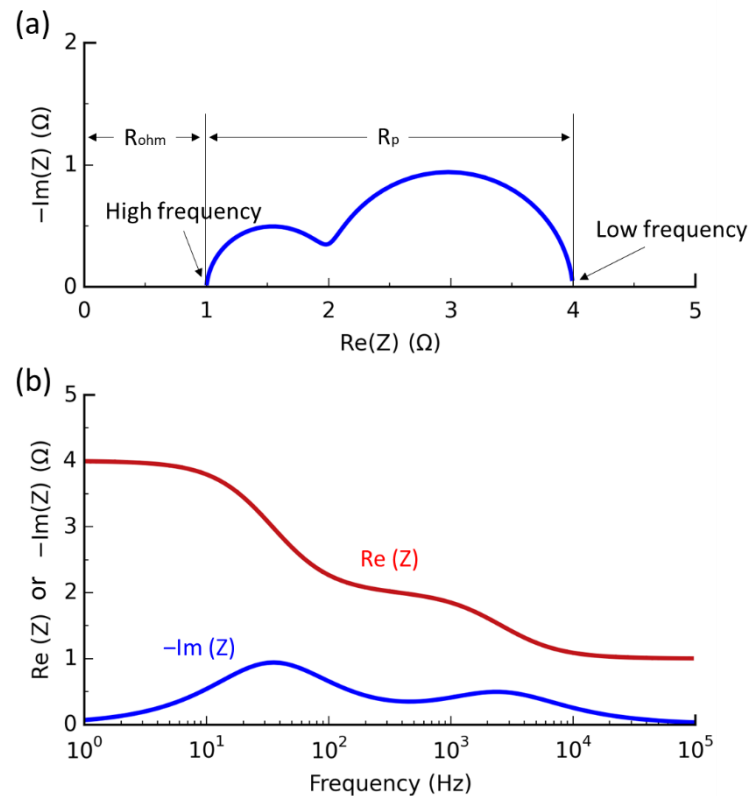


Figure 1.5: (a) Nyquist and (b) Bode plots of EIS data.

1.4.2 EIS analysis methods

EIS analysis is commonly performed by fitting the data with an equivalent circuit model using complex-nonlinear-least-squares (CNLS) regression. The electrical elements used in EIS analysis can be classified into lumped elements (including inductance, resistance, and capacitance) and frequency-dependent elements (including constant-phase element,

Warburg element, Gerisher element, etc...). [83] The equivalent circuit models usually consist of a number of electrical elements in series and/or in parallel, and the models are set based on the physical and chemical processes in the system studied. Thus, the different contributions to impedance can be distinguished. A typical example of impedance fitting is shown in **Figure 1.6**, where the impedance spectrum is fitted with an equivalent circuit model named $L-R_0-R_1Q_1-R_2Q_2$, consisting of an inductor (L) in series with a resistor and in series with two circuits of a resistor in parallel with a constant phase element (Q). The fitting error is shown in **Figure 1.6c**, where low relative residuals and a non-systematic variance are desired.

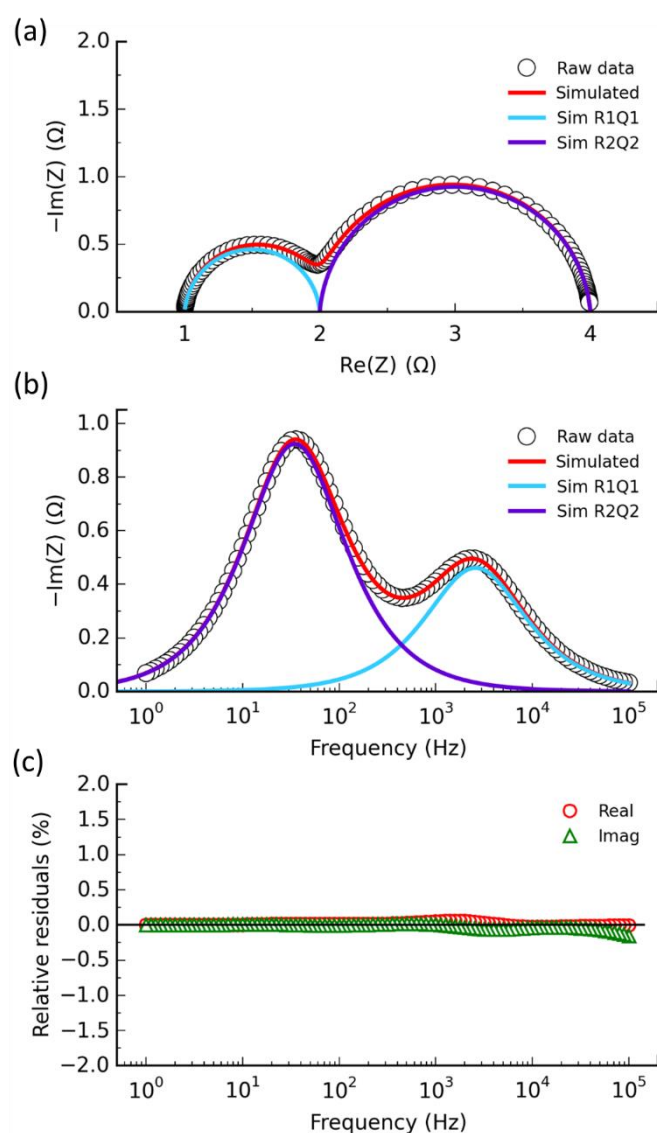


Figure 1.6: An example of impedance fitting. (a) Nyquist, (b) Bode, and (d) relative residual plots.

Distribution of relaxation time (DRT) is another powerful tool for deconvoluting complex impedance data. Ideally, the relation between the impedance $Z(\omega)$ and the distribution function of relaxation times ($\gamma(\tau)$) could be given by a convolution equation as follows: [84, 85]

$$Z(\omega) = R_0 + Z_{pol}(\omega) = R_0 + R_{pol} \int_0^{\infty} \frac{\gamma(\tau)}{1+j\omega\tau} d\tau \quad (1.8)$$

with $\int_0^{\infty} \gamma(\tau) d\tau = 1$

where $Z(\omega)$ is the impedance data, R_0 is the ohmic resistance, $Z_{pol}(\omega)$ is the polarization part of the impedance, and R_{pol} is the polarization resistance. The mathematical problem with this approach arises from the inversion of equation 1.8. First, impedance spectra are recorded over a limited frequency range in practical measurements and thus the convolution equation cannot be solved analytically. Furthermore, erroneous results are obtained with the inversion due to the large amplification of experimental errors. This inversion problem has been well controlled by extrapolating the original data to artificially enlarge the frequency range and applying digital filters to the Fourier transforms to reduce noise. Further theoretical background on DRT is described elsewhere. [84, 85]

To illustrate this method, the impedance spectrum shown in **Figure 1.5** was examined by DRT calculation. The result is shown in **Figure 1.7**, where the impedance response is clearly separated into two peaks at their characteristic frequencies. In DRT plots, the peaks are corresponding to the specific physical or chemical processes in the studied system. [84] Thus, DRT analysis is often used as a pre-identification tool to build a suitable equivalent circuit model for CNLS fitting. [44, 86]

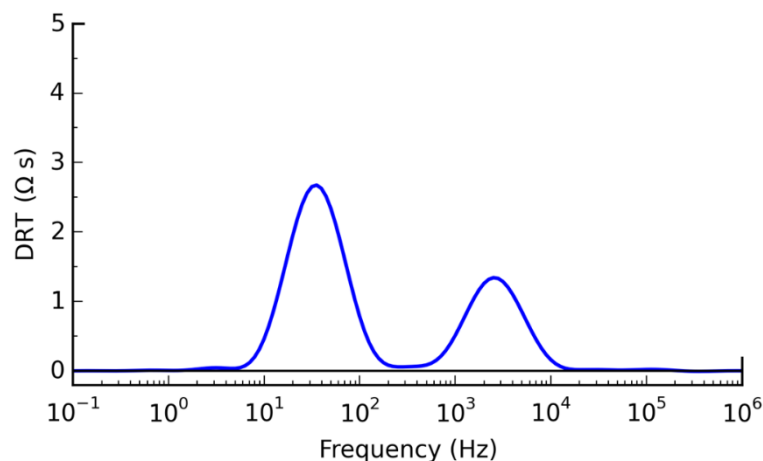


Figure 1.7: An example of DRT plot

1.5 Objective and scope of the thesis

As outlined in this chapter, though the SOC technology has shown potential in energy storage and conversion, the widespread commercialization of this technology is still impeded by high cost and insufficient lifetime. One of the key components determining the performance and reliability of SOCs is the electrodes. The objective of this thesis is to develop cost-effective SOC electrodes with sufficiently high electro-catalytic activity and durability at intermediate temperatures (600–750 °C). The study is based on the use of infiltration to fabricate nanostructured electrodes. The scale-up of the developed electrodes is also considered. Throughout the thesis, electrochemical characterization including electrochemical impedance spectroscopy (EIS), polarization curves, galvanostatic tests, and electrical conductivity relaxation (ECR) are employed. The analysis of EIS data is performed by fitting with equivalent circuit model using complex-nonlinear-least-squares (CNLS) regression and calculating the distribution of relaxation time (DRT). Other characterization techniques include scanning electron microscope (SEM), transmission electron microscopy (TEM), X-ray diffraction (XRD), and Brunauer-Emmett-Teller (BET) for measuring specific surface area. The results are divided into four chapters.

The results in **Chapter 2** highlight the potential of using infiltration to produce large-size, high-performance SOCs. In contrast to most of the previous studies on infiltrated SOCs carried out on button cells with a small active area, $12.5 \times 12.5 \text{ cm}^2$ fuel-electrode-supported SOCs with $\text{La}_{0.6}\text{Sr}_{0.4}\text{CoO}_{3-\delta}$ (LSC) infiltrated gadolinia-doped ceria (CGO) oxygen electrodes were prepared in this work. The electrochemical performance and durability of the resulting SOCs were examined at $4 \times 4 \text{ cm}^2$ level (active area).

The Ni/YSZ composite is the most commonly used fuel electrode in SOCs, and it often suffers from significant degradation during continuous electrolysis operation. To address this technical obstacle, in **Chapter 3**, an effective approach of surface modification of the Ni/YSZ electrode by coating nano-sized CGO electrocatalysts via infiltration was developed. The mechanisms of the Ni/YSZ electrode degradation and of the mitigation via surface modification at these conditions were discussed and speculated. Note that before infiltration the full cell needs to be pre-reduced with a “two-atmosphere-reduction”, i.e., the fuel electrode side is exposed to reducing atmosphere while the oxygen electrode is exposed to air. This was achieved using an in-house built test rig. Afterwards, in **Chapter 4**, the aforementioned infiltration approach was further simplified to fit the upscaling requirement by replacing the complicated “two-atmosphere-reduction” procedure with a facile “one-atmosphere-reduction”, which can be carried out during sintering of the cell.

Considering that cobalt-containing materials often suffer from various problems when employed as oxygen electrodes, in **Chapter 5**, a highly active and robust $\text{La}_{0.6}\text{Sr}_{0.4}\text{FeO}_{3-\delta}$ (LSF)-based oxygen electrode was developed by applying a nanoporous hybrid catalyst coating composed of nanoparticles of CGO and PrO_x . The resulting hybrid-catalyst-coated LSF electrode was investigated for both fuel-cell and electrolysis operation. Combining with the progress in the fuel electrode achieved in **Chapter 3**, a cell with this oxygen electrode and the CGO-modified Ni/YSZ fuel electrode was developed and investigated.

Table 1.1 Performance of Ni/YSZ fuel-electrode supported SOECs with the conventional LSM/YSZ oxygen electrodes. R_p represents the total polarization resistance of the cell.

Cell configuration	Gas supplied to the fuel electrode	Temperature (°C)	Electrolysis current density at 1.3 V ($A\ cm^{-2}$)	R_p ($\Omega\ cm^2$)	Ref.
Ni/YSZ YSZ LSM/YSZ	50% H ₂ O-50% H ₂	750	0.50		[87]
		850	1.00		
Ni/YSZ YSZ LSM/YSZ	50% H ₂ O-10% H ₂ -40% N ₂	950	0.9		[88]
		895	0.75		
		820	0.58		
		750	0.35		
Ni/YSZ YSZ LSM/YSZ	50% H ₂ O-50% H ₂	800	0.3		[89]
Ni/YSZ YSZ LSM/YSZ	50% H ₂ O-50% H ₂	900	0.58	0.44	[90]
		800	0.35	1.0	
Ni/YSZ YSZ LSM/YSZ	54% H ₂ O-23% H ₂ -23% N ₂	850	0.5		[91]
		800	0.33		
		750	0.22		
		700	0.1		

Table 1.2 Performance of Ni/YSZ fuel electrode supported SOECs with screen-printed MIEC oxygen electrodes. R_p represents the total polarization resistance of the cell.

Cell configuration	Gas supplied to the fuel electrode	Temperature (°C)	Electrolysis current density at 1.3 V (A cm ⁻²)	R_p (Ω cm ²)	Ref
Ni/YSZ YSZ SDC LSFCN	50% H ₂ O-50% H ₂	800	1.04		[92]
		750	0.85		
Ni/YSZ YSZ CGO LSCF/CGO	50% H ₂ O-50% H ₂	800	0.99		[93]
Ni/YSZ YSZ CGO LSCF/CGO	50% H ₂ O-50% H ₂	750	0.9	0.21 (1.2 V)	[29]
Ni/YSZ YSZ CGO LSCF/CGO	50% H ₂ O-50% H ₂	800	1.3 (1.25 V)		[94]
Ni/YSZ YSZ CGO LSC/CGO	50% H ₂ O-50% H ₂	800	1.28 (1.25 V)		[94]
Ni/YSZ YSZ CGO LSCF/CGO	50% H ₂ O-50% H ₂	800	0.85	0.15	
		750	0.58	0.22	[23]
		700	0.3		
Ni/YSZ YSZ CGO/PNO PNO	50% H ₂ O-50% H ₂	800	0.8		[34]
		700	0.26		
Ni/YSZ YSZ NNO/YSZ	50% H ₂ O-50% H ₂	800	0.585		[95]
		700	0.38		
Ni/YSZ YSZ CGO STFC-07	50% H ₂ O-50% H ₂	700	1.48	0.115	[96]
Ni/YSZ YSZ CGO SCFG	40% H ₂ O-H ₂ -N ₂	850	1.15		[97]
		800	0.75		

La_{0.5}Sr_{0.5}Fe_{0.8}Cu_{0.15}Nb_{0.05}O_{3-δ} (LSFCN), Ce_{0.9}Gd_{0.1}O_{1.95} (CGO), La_{0.6}Sr_{0.4}Co_{0.2}Fe_{0.8}O_{3-δ} (LSCF), La_{0.6}Sr_{0.4}CoO_{3-δ} (LSC), Pr₂NiO_{4+δ} (PNO), Nd₂NiO_{4+δ} (NNO), SrTi_{0.3}Fe_{0.63}Co_{0.07}O_{3-δ} (STFC-07), SrCo_{0.8}Fe_{0.1}Ga_{0.1}O_{3-δ} (SCFG)

Table 1.3 Performance of SOECs with oxide fuel electrodes instead of the Ni/YSZ. R_p represents the total polarization resistance of the cell.

Cell configuration	Gas supplied to the fuel electrode	Temperature (°C)	Electrolysis current density at 1.3 V (A cm ⁻²)	R_p (Ω cm ²)	Ref.
CMF LSGM BLC	20% H ₂ O-1% H ₂ -79% Ar	900	1.00		
		800	0.35		[98]
		700	0.10		
PBM LSGM LDC PBSCF50/CGO	10% H ₂ O-90% H ₂	750	0.81	0.118	
		700	0.52	0.161	[28]
LSNT YSZ LSM/YSZ	47% H ₂ O-53% N ₂	900	0.13		
		800	0.05		[57]
LST YSZ LSM/YSZ	47% H ₂ O-53% N ₂	900	0.05	1.4	[99]
SFM LSGM SFM	20% H ₂ O-80% H ₂	900	0.38		
		850	0.36		
		800	0.33		
		900	0.59		[100]
		850	0.54		
800	0.48				
K-PSCFN–CFA LSGM BCFN	20% H ₂ O-80% H ₂	800	0.6	0.54	[101]
LSCM-Pd-CZY-YSZ YSZ YSZ-LSF	10% H ₂ O-90% H ₂	700	0.4	0.19	[102]

SFM-YSZ YSZ LSM/YSZ	10%H ₂ O-90%H ₂	800	1.12	0.230	[60]
SFM/SDC LCO LSGM SDC/ LSCF	42%H ₂ O-58%H ₂	850	0.64	0.44	[59]
	42%H ₂ O-58%H ₂	800	0.838		[59]
SFMNi/SDC LCO LSGM S DC/LSCF		750	0.511		
		700	0.269		
LSF LSGM BLC	20%H ₂ O-1%H ₂ - 79%Ar	800	0.59	0.4	[103]
		700	0.21		
PSTF SDC YSZ LSM/YSZ	20%H ₂ O-H ₂ -Ar	800	0.13	0.8	[104]
	40%H ₂ O-H ₂ -Ar		0.16	0.75	
	60%H ₂ O-H ₂ -Ar		0.20	1.1	
LSCM/YSZ YSZ LSM/YSZ La _{0.75} Sr _{0.25} Cr _{0.5} Mn _{0.5} O _{3-δ} (LS CM)	25%H ₂ O	900	0.55		[105]
		850	0.40		
		800	0.30	0.9	
	80%H ₂ O	900	0.72		
		850	0.59		
		800	0.43	1.5	
LSCM/YSZ YSZ LSM/YSZ	60%H ₂ O	900	0.327		[55]
		850	0.280		
		800	0.177		
	20% H ₂ O	850	0.18		

LSCM YbScSZ LSCM	50% H ₂ O-N ₂	850	0.21	[106]
---------------------	-------------------------------------	-----	------	-------

$Ce_{0.6}Mn_{0.3}Fe_{0.1}O_{2-\delta}$ (CMF), $La_{0.9}Sr_{0.1}Ga_{0.8}Mg_{0.2}O_{3-\delta}$ (LSGM), $Ba_{0.6}La_{0.4}CoO_{3-\delta}$ (BLC),
 $PrBaMn_2O_{5+\delta}$ (PBM), $PrBa_{0.5}Sr_{0.5}Co_{1.5}Fe_{0.5}O_{5+\delta}$ (PBSCF50), $La_{0.4}Ce_{0.6}O_{2-\delta}$ (LDC),
 $Sr_2Fe_{1.5}Mo_{0.5}O_{6-\delta}$ (SFM), $Sr_2Fe_{1.3}Ni_{0.2}Mo_{0.5}O_6$ (SFMNi), $La_{0.8}Sr_{0.2}FeO_{3-\delta}$ (LSF),
 $Ba_{0.6}La_{0.4}CoO_{3-\delta}$ (BLC), $Pr_{0.8}Sr_{1.2}(Co,Fe)_{0.8}Nb_{0.2}O_{4+\delta}$ (K-PSCFN), Co-Fe alloy (CFA),
 $Ba_{0.9}Co_{0.7}Fe_{0.2}Nb_{0.1}O_{3-\delta}$ (BCFN), $La_{0.8}Sr_{0.2}FeO_{3-\delta}$ (LSF), $La_{0.8}Sr_{0.2}Cr_{0.5}Mn_{0.5}O_{3-\delta}$ (LSCM),
 $Ce_{0.48}Zr_{0.48}Y_{0.04}O_{2-\delta}$ (CZY), $Pr_{0.3}Sr_{0.7}Ti_{0.3}Fe_{0.7}O_{3-\delta}$ (PSTF), $SrTiO_{3+\delta}$ (ST), $La_{0.3}Sr_{0.7}TiO_{3+\delta}$ (LST),
 $La_{0.4}Sr_{0.4}Ni_{0.06}Ti_{0.94}O_{2.94}$ (LSNT), $(ZrO_2)_{0.9}(Yb_2O_3)_{0.06}(Sc_2O_3)_{0.04}$ (YbScSZ)

CHAPTER 2

Solid oxide cells with $\text{La}_{0.6}\text{Sr}_{0.4}\text{CoO}_{3-\delta}$ infiltrated oxygen electrodes for electricity generation and hydrogen production

Abstract

Infiltration is an effective way to improve the performance of the oxygen electrode for solid oxide cells (SOCs). Most studies on infiltrated SOCs are carried out on button cells with a small active area. Here, we report on the preparation of $12.5 \times 12.5 \text{ cm}^2$ fuel-electrode-supported SOCs with a $\text{La}_{0.6}\text{Sr}_{0.4}\text{CoO}_{3-\delta}$ (LSC) infiltrated gadolinia-doped ceria (CGO) oxygen electrode. The electrochemical performance of the resulting SOCs is examined at $4 \times 4 \text{ cm}^2$ level (active area). The cell delivers a power density of 1.08 W cm^{-2} at 0.6 V and $750 \text{ }^\circ\text{C}$ in fuel cell mode with high fuel and oxygen utilization of 52 and 57 %, respectively; in electrolysis mode, the current density reaches 1.07 A cm^{-2} at 1.3 V and $750 \text{ }^\circ\text{C}$ with a steam utilization of 60%. Additionally, the influence of feed gas composition on cell performance and the short-term durability of the cell in electrolysis mode are studied. Electrochemical impedance spectroscopy (EIS) results and the post-test microstructural characterization demonstrate that there is no visible degradation of the LSC infiltrated CGO oxygen electrode after the durability test. These results highlight the potential of large-scale production of high-performance SOCs by designing nanostructured electrode via infiltration.

2.1 Introduction

Affordable large-scale energy storage is essential for a sustainable energy future with a rising share of solar and wind-based intermittent electricity generation [107]. Solid oxide cells

(SOCs) is a promising technology in this context. They can be operated either in electrolysis mode to convert surplus electricity from these renewable sources into chemical energy stored in various fuels such as H₂ and/or CO, or in fuel cell mode to generate electricity using the fuels produced [6, 7, 9]. One of the key factors limiting the performance of SOCs is the rate of the oxygen electrode reaction processes, i.e., the oxygen reduction reaction (ORR) in fuel cell mode and the oxygen evolution reaction (OER) in electrolysis mode, particularly at temperatures ≤ 750 °C. The most well studied oxygen electrode material is strontium-doped lanthanum manganite (LSM)/yttria-stabilized zirconia (YSZ) composite. However, SOCs with LSM/YSZ electrodes have limited performance at reduced temperatures; at 750 °C, most such cells were reported to show power densities of 0.3-0.65 W cm⁻² at a voltage of 0.7 V in fuel cell mode and current densities of 0.2-0.5 A cm⁻² at 1.3 V in electrolysis mode [87, 88, 91, 108, 109].

Accordingly, mixed ionic-electronic conducting (MIEC) oxides, such as La_{0.6}Sr_{0.4}Co_{0.2}Fe_{0.8}O_{3- δ} (LSCF) [23, 24], La_{0.6}Sr_{0.4}CoO_{3- δ} (LSC) [25], Sm_{0.5}Sr_{0.5}CoO_{3- δ} (SSC) [26], Ba_{0.5}Sr_{0.5}Co_{0.8}Fe_{0.2}O_{3- δ} (BSCF) [27], PrBa_{0.5}Sr_{0.5}Co_{1.5}Fe_{0.5}O_{5+ δ} (PBSCF) [28], Pr₂NiO_{4+ δ} (PNO) [34] and Pr₆O₁₁ [110] have been employed as alternative oxygen electrode materials, resulting in improved performance. Solution infiltration, also known as impregnation, has drawn increasing interests for preparing these MIEC type electrodes [62, 63, 70, 71]. In the infiltration process the active electrocatalysts are introduced into a porous backbone at relatively low temperatures. Typically, the maximum firing temperature for the infiltrated electrode is now the temperature of cell operation. Issues of chemical reactivity and thermal expansion mismatch of such MIEC oxides with the other cell components can be alleviated. The resulting electrodes with nano-scale catalysts have shown improved catalytic activity for the ORR/OER. For example, a power density of 0.78 W cm⁻² at 0.7 V in fuel cell mode and a current density of 0.98 A cm⁻² at 1.3 V in electrolysis mode were reported on a cell with LSCF infiltrated YSZ oxygen electrode at 750 °C [111]. Even better performance was reported on a cell using LSCF/gadolinia-doped ceria (CGO) composite electrode infiltrated with SSC nano-catalysts, exhibiting a power density of 1.39 W cm⁻² at 0.7 V in fuel cell mode and a current density of 1.80 A cm⁻² at 1.3 V in electrolysis mode [29].

However, most reports of infiltrated SOCs were carried out on laboratory-scale button size cells with active areas less than 2 cm². The performance of such button cells does not

necessarily represent the performance of corresponding large-area, commercially relevant cells due to complexities related to the scale up of the manufacture and the influence of operating conditions such as increased gas utilization and non-isothermal operation. There have been only limited reports of successful manufacture of large-area cells using infiltration. In one exception, Jiang et al. reported a fuel-electrode-supported planar SOC with an active area of $9 \times 9 \text{ cm}^2$ and an LSCF infiltrated YSZ oxygen electrode [112]. This SOC was investigated for fuel cell operation, displaying a power density of 0.42 W cm^{-2} at 0.7 V and $750 \text{ }^\circ\text{C}$. More recently, we have developed two types of fuel-electrode-supported SOCs in size of $13 \times 13 \text{ cm}^2$ with either an LSC infiltrated YSZ oxygen electrode or a $\text{LaNi}_{0.6}\text{Co}_{0.4}\text{O}_{3-\delta}$ (LNC) infiltrated YSZ oxygen electrode and evaluated their performance for fuel cell operation at $4 \times 4 \text{ cm}^2$ level (active area) [113]. Even though a CGO coating was infiltrated into the YSZ backbone prior to infiltrating LNC electrocatalysts, the formation of poorly conducting zirconate phases ($\text{La}_2\text{Zr}_2\text{O}_7$ or SrZrO_3) at the interface between the electrocatalyst and YSZ backbone (where the CGO covering is not complete) was observed for 1300 h operation in fuel cell mode at $700 \text{ }^\circ\text{C}$, 0.5 A cm^{-2} .

In this chapter, $12.5 \times 12.5 \text{ cm}^2$ fuel-electrode-supported half cells with porous CGO backbones at the oxide electrode side are produced by scalable and cost-effective processes of tape-casting, lamination, and co-sintering, and then an LSC precursor solution is infiltrated into the CGO backbones to prepare nanostructured LSC-CGO oxygen electrode. A CGO backbone is applied instead of YSZ as CGO has good chemical compatibility with most of the preferred perovskite electrocatalysts (including LSC) and higher ionic conductivity than YSZ. The prepared planar SOCs are investigated at $4 \times 4 \text{ cm}^2$ level (active area) both in fuel cell mode and electrolysis mode. The durability of the cell in the electrolysis mode is investigated under a constant current density of 0.5 A cm^{-2} at $750 \text{ }^\circ\text{C}$

2.2 Experimental

2.2.1 Cell preparation

The $12.5 \times 12.5 \text{ cm}^2$ fuel-electrode-supported cells with a configuration NiO/YSZ support | NiO/YSZ fuel electrode | YSZ electrolyte | CGO barrier | CGO backbone were produced by laminating and co-sintering tape-cast green tapes at $1315 \text{ }^\circ\text{C}$. The green tapes of NiO/YSZ support, NiO/YSZ fuel electrode and CGO backbone were prepared by single layer tape-casting while tapes of YSZ electrolyte and CGO barrier were prepared via a multilayer tape casting (MTC) process. The CGO backbone tape was prepared with the addition of 60-70 % pyrolyseable pore former in the tape-cast slurry to obtain sufficient porosity after sintering. The volume ratio of Ni to YSZ in the Ni/YSZ support and electrode was controlled to be 40/60 after the reduction of NiO. Afterwards, LSC catalyst was coated on the internal surfaces of the porous CGO backbone via the infiltration technique. Specifically, 0.5 M LSC nitrate solution containing $\text{La}(\text{NO}_3)_3$, $\text{Sr}(\text{NO}_3)_2$, and $\text{Co}(\text{NO}_3)_3$ in a molar ratio of 3:2:5 was dropped onto the surface of the CGO backbone. The solution sucked into the pores of the backbone driven by capillary forces. Note that the surfactant Pluoronic[®] P123 (1.7 wt.%) was added into the nitrate solution to improve wetting/penetration of the structure [113]. The infiltrated samples were then calcinated at $350 \text{ }^\circ\text{C}$ in air for 15 min. The infiltration/calcination processes were repeated 9 times to get a loading of $\sim 1300 \text{ mg}$ of LSC catalysts per 1 cm^3 CGO scaffold. After the infiltration, the cells were cut into pieces of $5.3 \times 5.3 \text{ cm}^2$ to fit the in-house constructed cell test houses. Finally, an LSC layer in size of $4 \times 4 \text{ cm}^2$ was screen printed onto the oxygen electrode to enhance the current collection.

2.2.2 Electrochemical characterization

The electrochemical performance and durability of the prepared cells were investigated using in-house constructed test rigs. In each test, a cell was mounted onto an alumina housing and sealed with a gold frame, as described in previous work [114]. The cells were heated to $800 \text{ }^\circ\text{C}$ with a heating rate of $1 \text{ }^\circ\text{C min}^{-1}$ and with pure Ar fed to the fuel electrode and dry air to the oxygen electrode. Afterwards, the cells were held at $800 \text{ }^\circ\text{C}$ for 4 h with the fuel

electrode first fed with 9% H_2 -91% Ar for 2 h, followed by another 2 h in 4% H_2O -96% H_2 to fully reduce all NiO to Ni and form a percolating network. Meanwhile, the oxygen electrode was treated with air to enable the infiltrates to form the desired LSC crystalline phase. The electrochemical performance of the cells was evaluated at 800–700 °C under varying gas feeds to the electrodes, but the flow rates of gases in the fuel and oxygen electrodes were kept at 24 l h^{-1} and 50 l h^{-1} , respectively. Electrochemical impedance spectroscopy (EIS) measurements were conducted using a Solartron 1255 frequency response analyzer in combination with a measurement resistor, at frequencies from 0.0968 to 96850 Hz with an amplitude of 3.75 mA cm^{-2} . The durability of the cell was evaluated in electrolysis mode at 750 °C under a constant current density of 0.5 A cm^{-2} , with 13.4 l h^{-1} 90% H_2O -10% H_2 fed to the fuel electrode and 50 l h^{-1} pure O_2 to the oxygen electrode. EIS data were recorded every 20 h during the durability test under the current of 0.5 A cm^{-2} . All of EIS data analyses were carried out using the Python-based software Ravdav [115].

2.2.3 Microstructure characterization

The cell structure was examined using scanning electron microscopy (SEM) in a Zeiss Merlin microscope. Both polished and fractured cross-sections of the cells were prepared for SEM characterization, corresponding to the SEM micrographs shown in **Figure 2.1** and **Figure 2.8**, respectively. SEM image analysis was carried out with ImageJ software. In order to check the phase composition of the infiltrates deposited on the CGO backbone, powders synthesized by calcinating the above LSC infiltrate solution at 800 °C for 4 h were examined at room temperature using X-ray diffraction (XRD, Bruker D8 Rigaku, $\text{CuK}\alpha$ radiation) with a scanning range of 20–80° and a step size of 0.01°

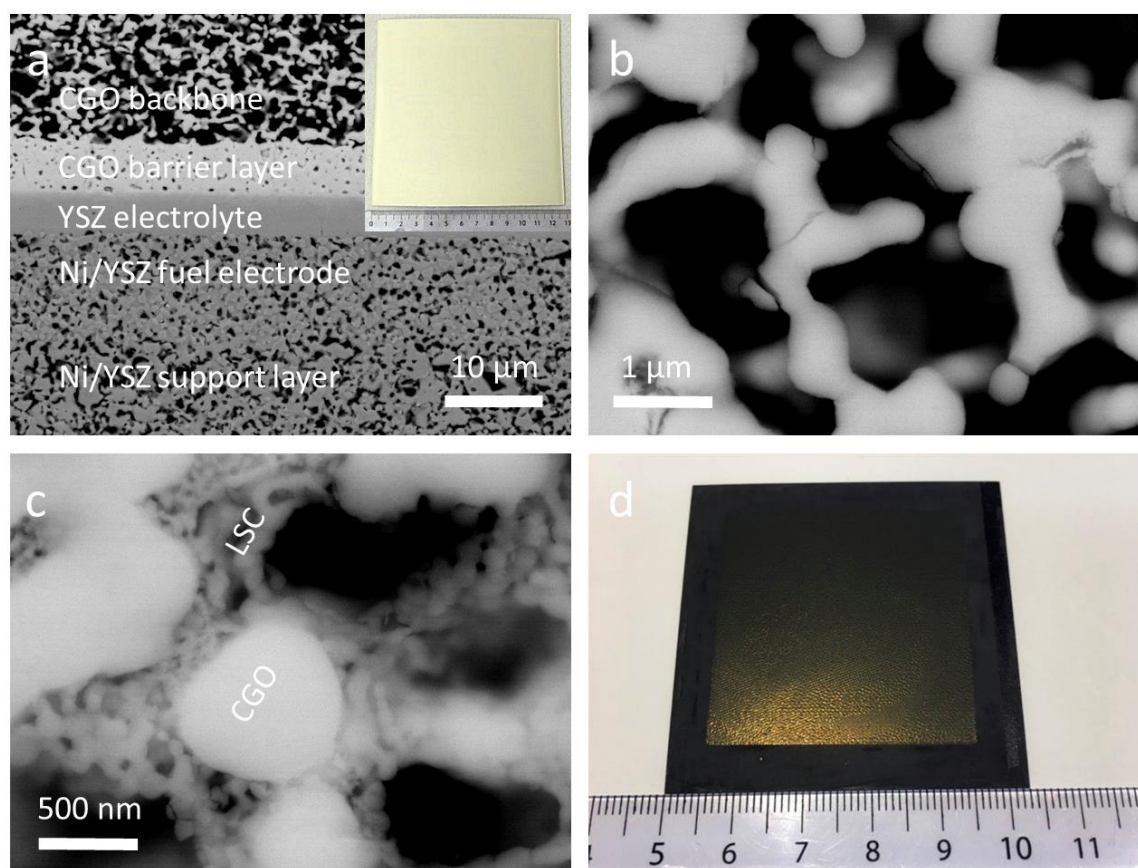


Figure 2.1: Cross-sectional SEM images of (a) a fuel electrode-supported cell prior to the infiltration of LSC (inset showing the photograph of this cell in size of $12.5 \times 12.5 \text{ cm}^2$), (b) porous CGO backbone, and (c) CGO backbone infiltrated with LSC catalysts. (d) Photograph showing the as-prepared planar cell for testing.

2.3 Results and discussion

2.3.1. Microstructure

Figure 2.1a and **Figure 2.S1** show the typical cross-sectional SEM micrographs of the fuel-electrode-supported cell prior to infiltration of LSC catalysts. The cell consists of a Ni/YSZ support ($\sim 300 \mu\text{m}$), a Ni/YSZ fuel electrode ($\sim 15 \mu\text{m}$), a YSZ electrolyte ($\sim 5 \mu\text{m}$), a CGO barrier layer ($\sim 6 \mu\text{m}$), and a porous CGO backbone ($\sim 25 \mu\text{m}$). There is good adherence between different layers as no obvious delamination or crack is observed. The

YSZ electrolyte is fully dense while some closed pores are observed in the CGO barrier layer. The CGO backbone for infiltration has a uniform porous microstructure with a porosity of $\sim 55\%$ and an average pore size of $\sim 1.3\ \mu\text{m}$, estimated based on counting black and gray pixels of the micrograph, which refer to pores and CGO grains, respectively (**Figure 2.1a** and **1b**). The LSC infiltrated CGO oxygen electrode is prepared by infiltration of LSC catalysts and calcination at $800\ \text{°C}$, and its micrograph is shown in **Figure 2.1c**, where the interconnected and nanoporous LSC coatings are well deposited on the internal surfaces of the porous CGO backbone. Formation of LSC in the coatings is confirmed by XRD pattern of powders, synthesized by calcinating the infiltrate solution at $800\ \text{°C}$ (**Figure 2.2**). Note that some second phases including $(\text{La}_{2-x}\text{Sr}_x)\text{CoO}_4$, SrCO_3 , and Co_3O_4 , are also observed in the LSC catalysts. Similar secondary phases of LSC infiltration have also been reported by Samson et al. [74]. **Figure 2.1d** shows a photograph of the as-prepared planar cell that has been cut into the size of $5.3 \times 5.3\ \text{cm}^2$, with a screen-printed $4 \times 4\ \text{cm}^2$ LSC contact layer on top of the LSC infiltrated CGO oxygen electrode.

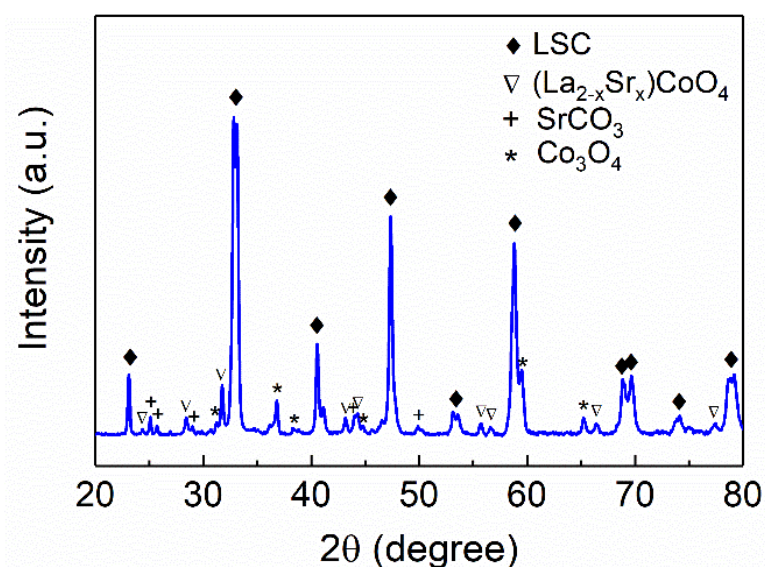


Figure 2.2: XRD pattern of the LSC powders calcinated at $800\ \text{°C}$.

2.3.2. Electrochemical performance

The electrochemical performance of the as-prepared cells was evaluated both in fuel cell mode and electrolysis mode. The active area of the cells is $4 \times 4 \text{ cm}^2$ (the edges are used for sealing, as described in Experimental). **Figure 2.3a** shows typical polarization curves of cell voltage and power density versus current density (I - V - P curves) of fuel cell operation, measured at 700–800 °C with 4% H_2O -96% H_2 fed to the fuel electrode and dry air to the oxygen electrode. The open circuit voltages (OCVs) range between 1.050 V at 800 °C and 1.069 V at 700 °C, and are within 35 mV off the calculated Nernst potentials. Under a voltage output of 0.6 V, the cell delivers power densities of 1.34, 1.08, and 0.70 W cm^{-2} at 800, 750, and 700 °C, respectively. Unlike most of the previous SOC studies, in which the power densities are reported on button cells with active areas less than 2 cm^2 and gas utilization lower than 10 %, the here-reported power densities are accompanied with significant fuel and oxygen utilization, e.g., 65 and 71 % at 800 °C, 52 and 57 % at 750 °C, and 34 and 37 % at 700 °C, respectively (**Figure 2.2b**). A high gas utilization is required for practical applications and leads to lower power out than with negligible utilization due to the loss of Nernst potential along the fuel flow. The effect of fuel utilization on cell performance was further illustrated by feeding H_2O - H_2 mixtures with varying H_2O to H_2 ratios. The OCV decreases from 1.060 to 0.947 V with decreasing H_2 content from 96% to 50% in accordance with the Nernst equation (**Figure 2.3c**). At a voltage of 0.6 V, power densities decrease from 1.08 to 0.78 W cm^{-2} , corresponding to a fuel utilization of 52 % and 72 %, respectively (**Figure 2.3d**).

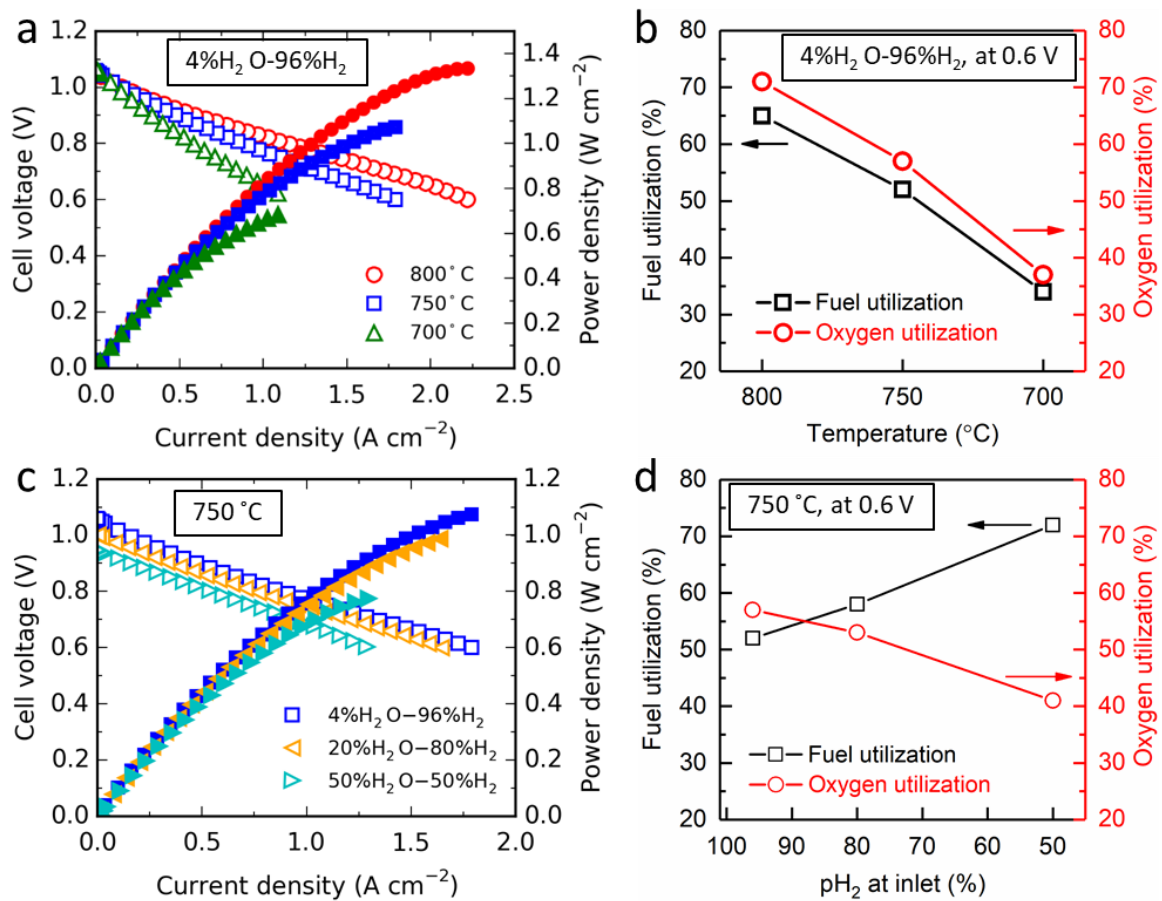


Figure 2.3: Performance in fuel cell mode. Voltage and power density versus current density measured (a) at different temperatures with 4% H₂O-96% H₂ fed to the fuel electrode and dry air to the oxygen electrode, and (c) at 750 °C with different H₂O-H₂ gas mixtures fed to the fuel electrode and dry air to the oxygen electrode. (b, d) Corresponding fuel utilization and oxygen utilization at an operating voltage of 0.6 V on the performance shown in (a) and (c).

Figure 2.4a shows the voltage versus current density (*I-V*) curves in electrolysis mode for H₂ production, measured at 700–800 °C with 50% H₂O-50% H₂ fed to the fuel electrode and dry air to the oxygen electrode. The OCVs at different temperatures are all within 10 mV of the calculated Nernst potentials. At an electrolysis voltage of 1.3 V, current densities of 1.37, 1.07, and 0.69 A cm⁻² are obtained at 800, 750, and 700 °C, respectively, which correspond to the H₂ production rates of 9.53, 7.45, and 4.80 ml min⁻¹ cm⁻², respectively, calculated using Faraday's law. These H₂ production rates are achieved with steam utilization of 76 %, 60%, and 38%, respectively, and the hydrogen content in the outlet gas reaches 88 %, 80%, and 69%. At 800 °C, a significantly nonlinear increase in the voltage at high current densities is observed, which is attributed to the effect of growing concentration

polarization because of the steam starvation in the fuel electrode under high steam utilization [94, 116].

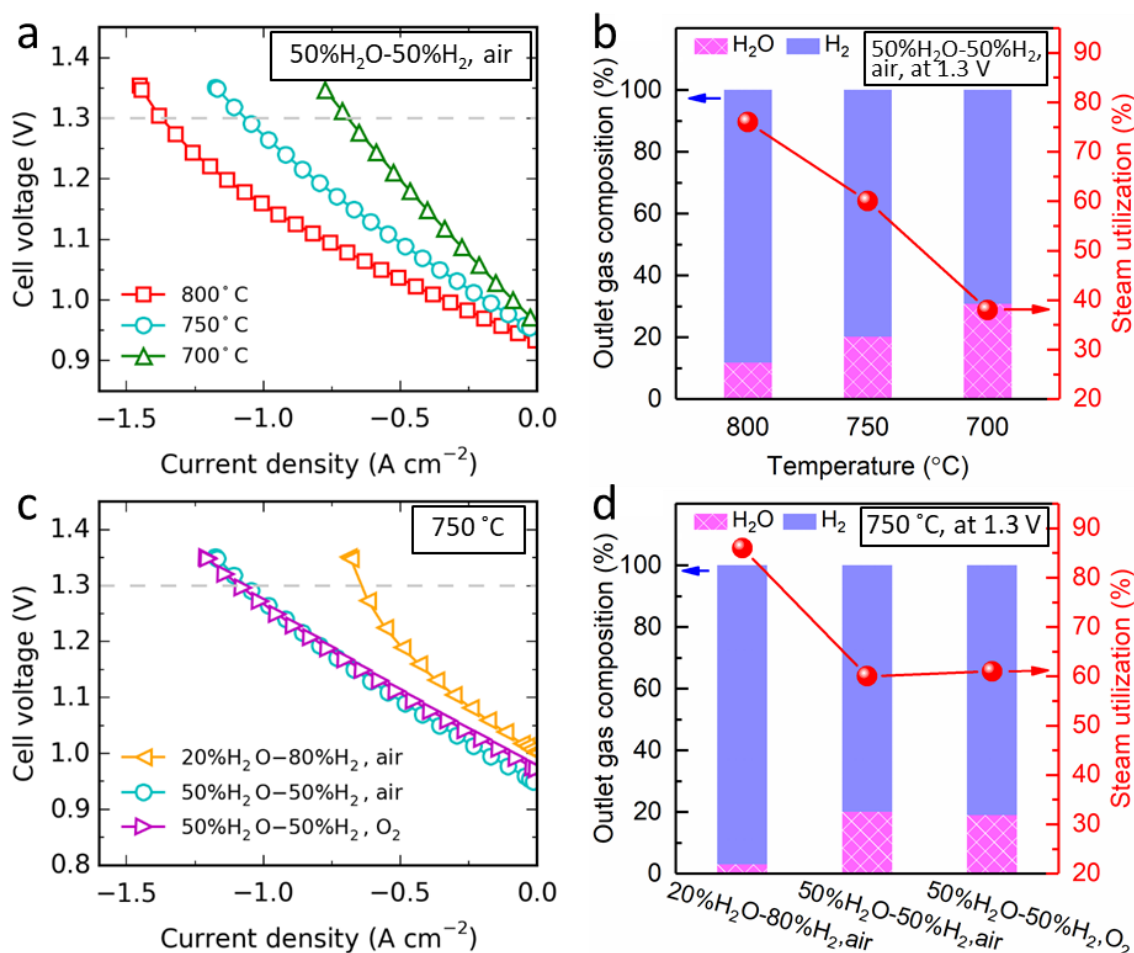


Figure 2.4: Performance in electrolysis cell mode. Voltage versus current density measured (a) at different temperatures with 50% H_2O -50% H_2 fed to the fuel electrode and dry air to the oxygen electrode, and (c) at 750 °C with varying gas feeds to the electrodes. (b, d) Corresponding gas composition at the outlet and overall steam utilization at an operating potential of 1.3 V on the performance shown in (a) and (c).

The electrolysis performance was also investigated under different gas feeds to the fuel and oxygen electrodes at 750 °C. As shown in **Figure 2.4c**, increasing the H_2O content from 20 % to 50 % leads to a decrease in OCV of 54 mV. The cell exhibits a current density of 0.64 A cm^{-2} at 1.3 V with 20% H_2O -80% H_2 fed to the fuel electrode. This performance is strongly limited by the concentration polarization due to the high steam utilization of 86 %, and the corresponding hydrogen content in the outlet gas is as high as 97% (**Figure 2.4d**).

By increasing H₂O content to 50%, the concentration polarization is significantly reduced, resulting in an increase in current density of 67 % (i.e., 0.43 A cm⁻²) at 1.3 V. **Figure 2.4c** also shows that the OCV increases 25 mV when the gas in the oxygen electrode is changed from air to pure O₂, and the current density at 1.3 V has a slight increase of 2 % (i.e., 0.02 A cm⁻²). Hence, the decreased driving force due to the increased OCV is fully compensated for by improved electrode performance in pure O₂. One should note that in principle for technical use, O₂ purge at the oxygen electrode is not likely to be a preferred mode of operation. Either no purge should be applied – “oxygen production mode” or for safety reasons steam, CO₂ or N₂ purge could be considered depending on whether the produced oxygen will be used or discarded. The results show that electrolysis performance is more sensitive to the H₂O content in the fuel electrode and the corresponding steam utilization and less sensitive to the oxygen content in the oxygen electrode, as expected both from the relative thickness of the electrodes and the form of the Nernst expression.

Figures 2.5a-e show the Nyquist plots of EIS data recorded under OCV condition in the temperature range of 700–800 °C with different gas feeds. The intercept with the real axis at high frequency in the Nyquist plot represents the ohmic resistance (R_{ohm}), and the difference between the high and low frequency intercepts represents the total electrode polarization resistance (R_p). R_{ohm} is almost unaltered with the change of gas feeds, and they are around 0.11, 0.16, and 0.25 $\Omega \text{ cm}^2$ at 800, 750, and 700 °C, respectively. These R_{ohm} are much greater than the expected resistances for 5 μm thick YSZ electrolyte and 6 μm thick CGO barrier here. At 700 °C, the observed R_{ohm} of 0.25 $\Omega \text{ cm}^2$ is 5 times the expected ($\sim 0.05 \Omega \text{ cm}^2$) based upon the ionic conductivities of 0.02 S cm⁻¹ for YSZ and 0.03 S cm⁻¹ for CGO [117]. This can be attributed to the interdiffusion of elements at the YSZ electrolyte – CGO barrier interface during the co-sintering process at 1315 °C leading to the formation of solid solution phases with lower ionic conductivity [118-120]. Furthermore, R_{ohm} actually constitute 29–40 % and 56–60 % of the overall resistances of the EIS data shown in **Figures 2.5a** and **5c**, respectively. These results suggest that there is room for further improvement of the cell performance by limiting the YSZ – CGO inter-diffusion via, e.g., lowering the sintering temperature, or more preferably sintering the half-cell (NiO/YSZ support | NiO/YSZ fuel electrode | YSZ electrolyte) first and then sintering CGO barrier and porous CGO layer at lower temperature, such as 1200 °C.

For 4% H₂O-96% H₂ fed to the fuel electrode and air to the oxygen electrode, the R_p values are 0.26, 0.30, and 0.38 $\Omega \text{ cm}^2$ at 800, 750, and 700 °C, respectively (**Figure 2.5a**). These R_p values are lower than those of our previously reported Ni/YSZ fuel electrode supported cell with a thin YSZ electrolyte, a CGO barrier layer applied by pulsed vapor deposition (PVD), and a screen printed LSC/CGO oxygen electrode [47], showing R_p values of 0.44 $\Omega \text{ cm}^2$ at 750 °C and 0.59 $\Omega \text{ cm}^2$ at 700 °C under same gas conditions (**Figure 2.S2**). The R_p values are also lower than many of those previously reported for other cells with Ni/YSZ fuel electrodes and using different oxygen electrodes, e.g., 0.43 $\Omega \text{ cm}^2$ at 750 °C for the commonly used LSCF/CGO composite [29], 0.78 $\Omega \text{ cm}^2$ at 700 °C for SSC infiltrated YSZ [121], and 0.44 $\Omega \text{ cm}^2$ at 700 °C for LaNi_{0.6}Co_{0.4}O_{3- δ} (LNC) infiltrated YSZ [122]. Furthermore, the R_p values are comparable to those reported recently for high-performance cells using Sm_{0.5}Sr_{0.5}CoO_{3- δ} (SSC) infiltrated LSCF/CGO composite (e.g., 0.28 $\Omega \text{ cm}^2$ at 750 °C) [29] and SrTi_{0.3}Fe_{0.63}Co_{0.07}O_{3- δ} (e.g., 0.27 $\Omega \text{ cm}^2$ at 750 °C) [96]. With increasing the H₂O content from 4 % to 50 %, the R_p decreases pronouncedly at corresponding temperatures (**Figures 2.5c** and **5e**), to 0.09, 0.12, and 0.18 $\Omega \text{ cm}^2$, respectively. The observed R_p of 0.18 $\Omega \text{ cm}^2$ at 700 °C is also lower than those reported for Ni/YSZ fuel-electrode-supported cells using different oxygen electrodes under the same condition, including LSCF/CGO composite (0.33 $\Omega \text{ cm}^2$) [23], SSC infiltrated YSZ (0.66 $\Omega \text{ cm}^2$) [121], Nd₂NiO_{4+ δ} (NNO) infiltrated Zr_{0.88}Sc_{0.22}Ce_{0.01}O_{2.11} (SSZ) (0.51 $\Omega \text{ cm}^2$) [123], and LSCF infiltrated YSZ (0.20 $\Omega \text{ cm}^2$) [111]. These EIS results demonstrate the high performance of the LSC infiltrated CGO oxygen electrode, and that this electrode is very suitable for the purpose.

To clarify the type of electrode processes and their contributions to R_p , the method based on calculating the distribution function of relaxation times (DRT) was applied in the EIS analysis. **Figures 2.5b**, **5d**, and **5f** show the DRT plots calculated from the EIS data shown in **Figures 2.5a**, **5c**, and **5e**, respectively. These DRT plots have a set of five distinct peaks denoted P1 to P5 from high to low frequency. Each peak represents an electrode process, and its integral area is a measure of the resistance of that process.

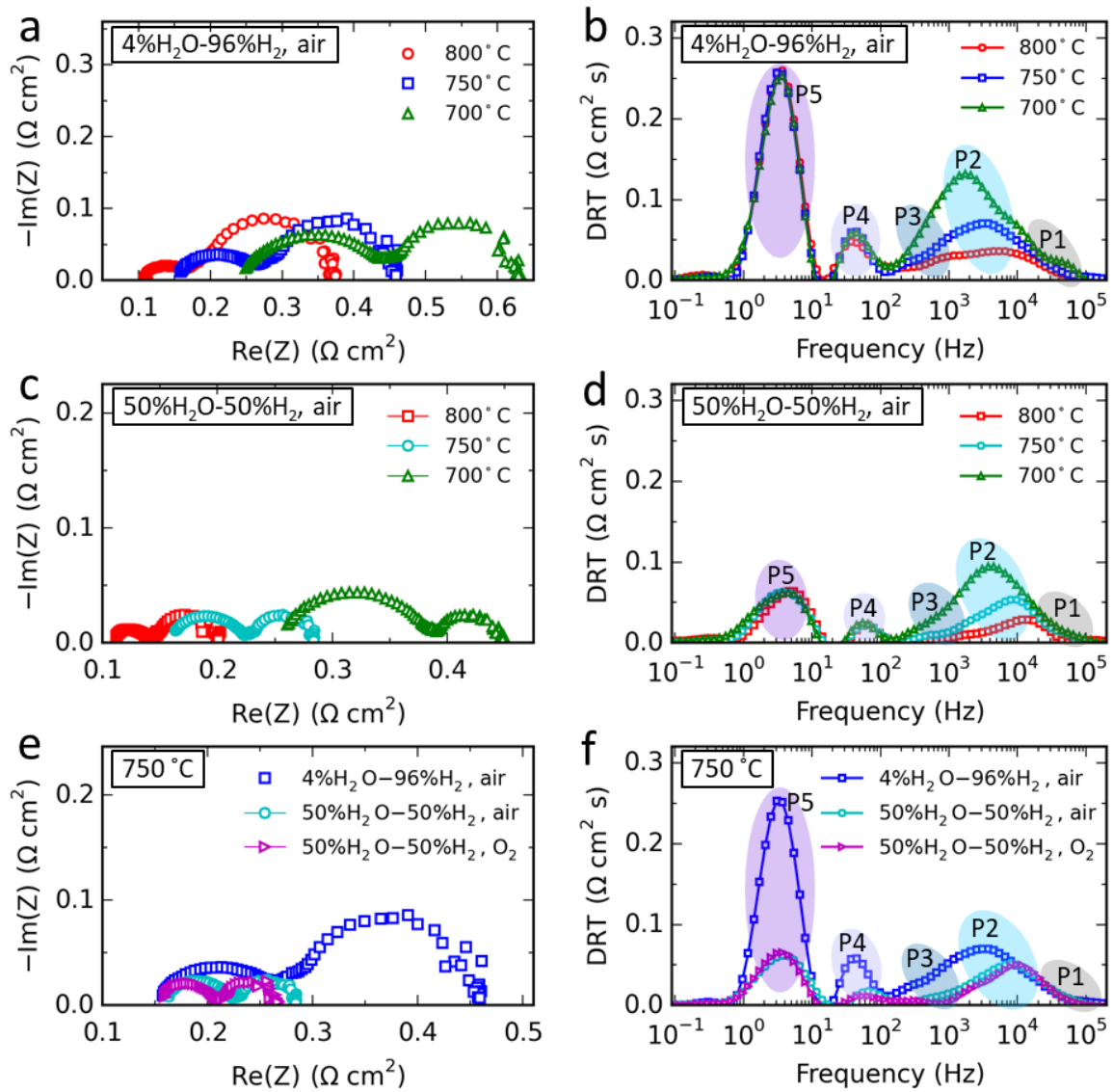


Figure 2.5: Nyquist plots of EIS data recorded under OCV (a) at different temperatures with 4% H₂O-96% H₂ fed to the fuel electrode and dry air to the oxygen electrode, (c) at different temperatures with 50% H₂O-50% H₂ fed to the fuel electrode and dry air to the oxygen electrode, and (e) at 750 °C with varying gas feeds to the electrodes. (b, d, f) Corresponding DRT plots of EIS data shown in (a), (c) and (e).

Evidently from **Figures 2.5b** and **5d** the processes associated with P1 to P3 are characterized by a pronounced thermal activation while P4 and P5 are not sensitive to temperature. This strongly indicates that P1 to P3 correspond to the chemical and electrochemical processes in the electrodes and P4 and P5 are related to gas diffusion and conversion [124]. **Figure 2.5f** shows that P2, P4, and P5 are very sensitive to the ratio of H₂O to H₂ in the fuel electrode compartment while they are almost independent of gas

change in the oxygen electrode. Thus, P2 is most likely associated with charge transfer processes at the triple phase boundaries (TPBs) of the fuel electrode; P4 represents the gas diffusion and the major contribution of P4 is from the fuel electrode; P5 is the gas conversion impedance in the fuel electrode [43, 44]. Furthermore, P1 is independent of any gas changes, and it is likely associated with the transport of oxygen anions through the ionic conducting networks in the electrodes [43, 44, 46]. Since the present cell has a highly ionic conducting CGO backbone based oxygen electrode, the major contribution of P1 is from the fuel electrode that has a YSZ network. The change of gas in the oxygen electrode compartment from air to O₂ leads to a change in P3, indicating that P3 is likely related to the charge transfer processes of oxygen incorporation/evolution at the TPBs of the oxygen electrode [44, 125]. The DRT results suggest that for the present cell with the Ni/YSZ fuel electrode and the nanostructured LSC infiltrated CGO oxygen electrode, the resistance of the fuel electrode dominates the total R_p while the resistance of oxygen electrode is much smaller.

2.3.3. Durability

The durability of the cell was evaluated under electrolysis condition with a constant applied current density of 0.5 A cm⁻², and 90% H₂O-10% H₂ fed to the fuel electrode and pure O₂ to the oxygen electrode. **Figure 2.6a** shows the evolution of cell voltage with time and the trend of cell degradation. Only 86 h of durability data is shown, because the test was terminated involuntarily after 86 h due to a malfunction in the H₂ supply, which led to the redox of the Ni/YSZ support thus damaging the cell structure. The degradation rate increases from ~0.3 to ~0.6 mV h⁻¹ in the first 30 h, then decreases towards ~0.1 mV h⁻¹ in the following 50 h.

Figure 2.6b shows the Nyquist plots of the EIS data recorded under current during the durability test. The almost unaltered R_{ohm} and the pronouncedly increased R_p shows that the cell degradation processes occur mainly on the electrodes. Between each two of the spectra measured at every 20 h, the R_p of EIS data recorded at 20 h and 40 h exhibits the largest difference, in agreement with the evolution of degradation rate shown in **Figure 2.6a**. Furthermore, among the five peaks of the DRT plots shown in **Figure 2.6c**, P2 increases significantly, implying that the major degradation is from the Ni/YSZ fuel electrode. This degradation of Ni/YSZ fuel electrode during electrolysis operation has also been reported previously [42, 45, 47, 126]. It is difficult to precisely determine the evolution of the

resistance of the LSC-CGO oxygen electrode (P3), because the oxygen electrode impedance is relatively small and with respect to time constants it is overlapping with P2.

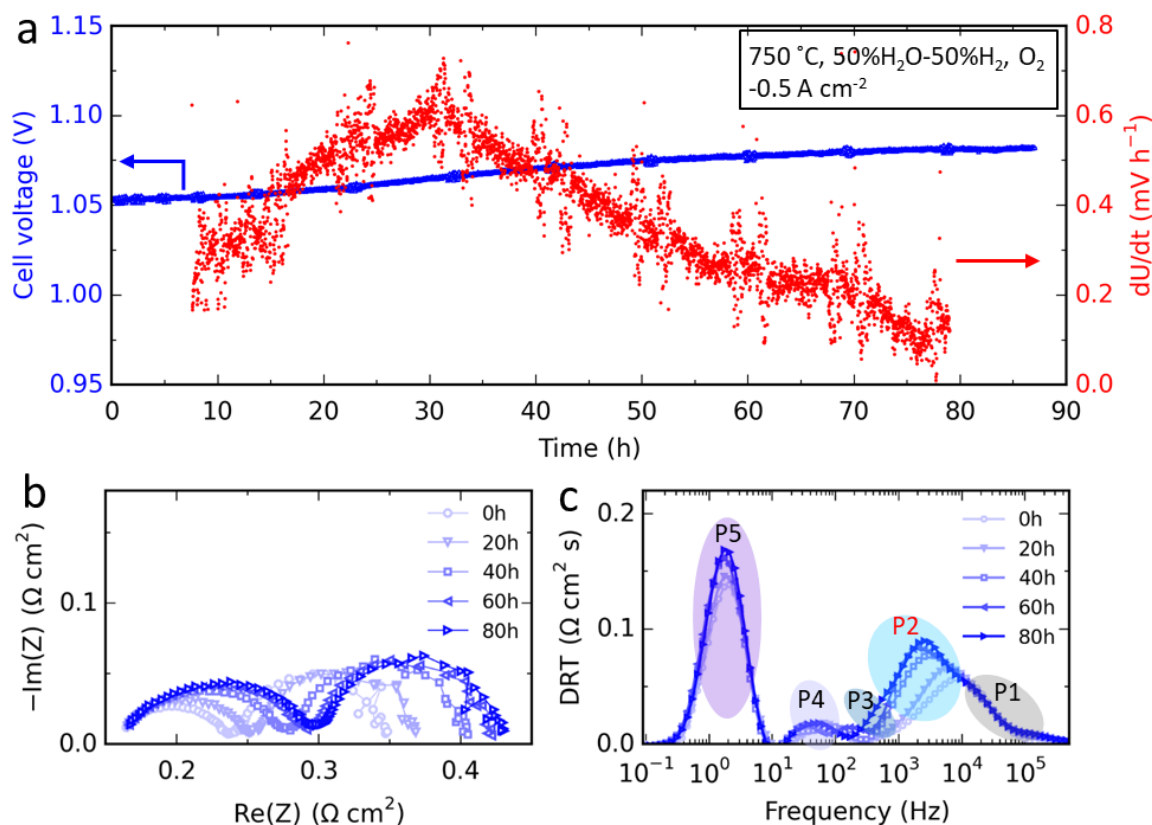


Figure 2.6: Durability for steam electrolysis. (a) Evolution of cell voltage during short-term test under a constant current density of 0.5 A cm^{-2} at 750 °C with $90\% \text{H}_2\text{O}-10\% \text{H}_2$ fed to the fuel electrode and pure oxygen to the oxygen electrode. (b) Nyquist plots and (c) DRT plots of EIS data recorded under -0.5 A cm^{-2} during durability test.

These EIS data were further fitted with an equivalent circuit model shown in **Figure 2.7a**. The model consists of four constant phase elements (RQ) and a modified Gerischer element (G), matching to the five different processes seen by DRT analysis, along with the R_{ohm} and an inductor (L) [46, 47]. The fitted spectra of EIS data measured at 0 h and 80 h are shown in **Figure 2.7b** as examples. **Figure 2.7c** summarizes the resistance values for each circuit element obtained from the fits. The value of R_3 (corresponding to the Gerischer element in the circuit model and the resistance of P3 of which includes the oxygen evolution steps at TPBs in the oxygen electrode, $R_{\text{LSC-CGO TPB}}$) is only $0.010 \text{ } \Omega \text{ cm}^2$ initially, demonstrating the high activity of the LSC infiltrated CGO oxygen electrode for the OER. Furthermore, the R_3 has an increase of $0.002 \text{ } \Omega \text{ cm}^2$ in 80 h, contributing to less than 3% of the total increase of

R_p ($0.078 \Omega \text{ cm}^2$). While the increase of R_1 (corresponding to the resistance for P1 of transport of oxygen anions, R_{ion}) and R_2 (corresponding to the resistance for P2 including the steam splitting processes at the TPBs of the fuel electrode, $R_{\text{Ni/YSZ TPB}}$) are $0.009 \Omega \text{ cm}^2$ and $0.046 \Omega \text{ cm}^2$, respectively, and contributes to $\sim 70\%$ of the total increase of R_p . Albeit being encompassed with some uncertainty of fitting due to overlapping time scales, these results further confirm that the degradation of the cell is mainly from the Ni/YSZ fuel electrode, and demonstrates that also after 80 h the contribution from the LSC-CGO oxygen electrode is negligible.

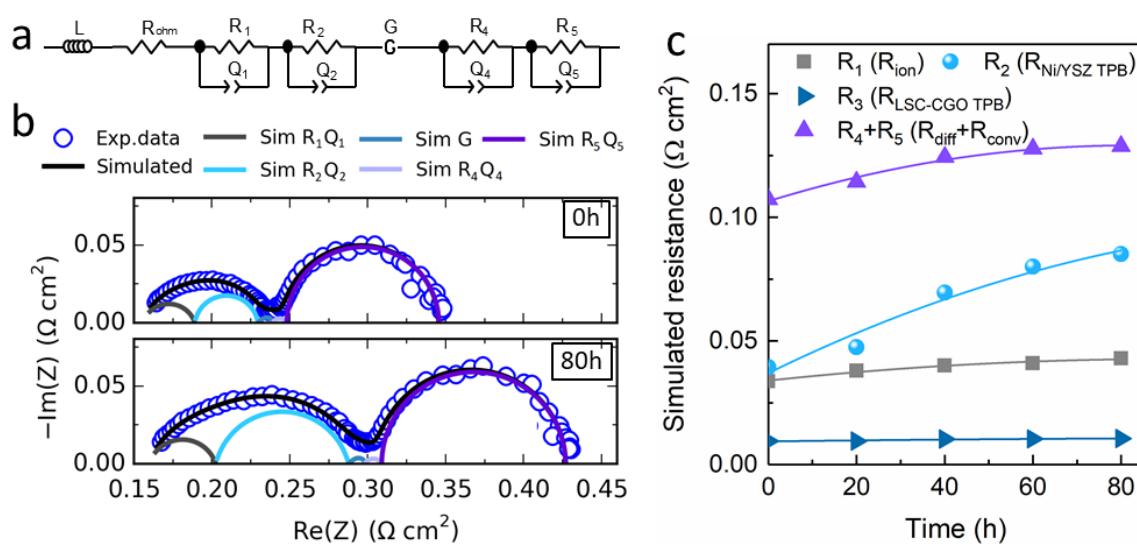


Figure 2.7: (a) Equivalent circuit model for CNLS fit. (b) CNLS fits of EIS data recorded at 0 h and 80 h of durability test under -0.5 A cm^{-2} at $750 \text{ }^\circ\text{C}$ with $90\% \text{ H}_2\text{O}$ - $10\% \text{ H}_2$ fed to the fuel electrode and pure oxygen to the oxygen electrode. (c) Resistances from the fitting results.

SEM micrographs of the LSC-CGO oxygen electrode before and after durability test are shown in **Figure 2.8**. No obvious growth of the LSC nanoparticles is observed, consistent with the EIS results. It is worth noting that recently some encouraging progress has been made in insight into the degradation mechanism of Ni/YSZ fuel electrode during electrolysis and exploring strategies to reduce this degradation [44, 50, 127-130]. For example, our laboratory has found that the durability of Ni/YSZ fuel electrode can be significantly enhanced by optimizing the microstructure of electrode [44].

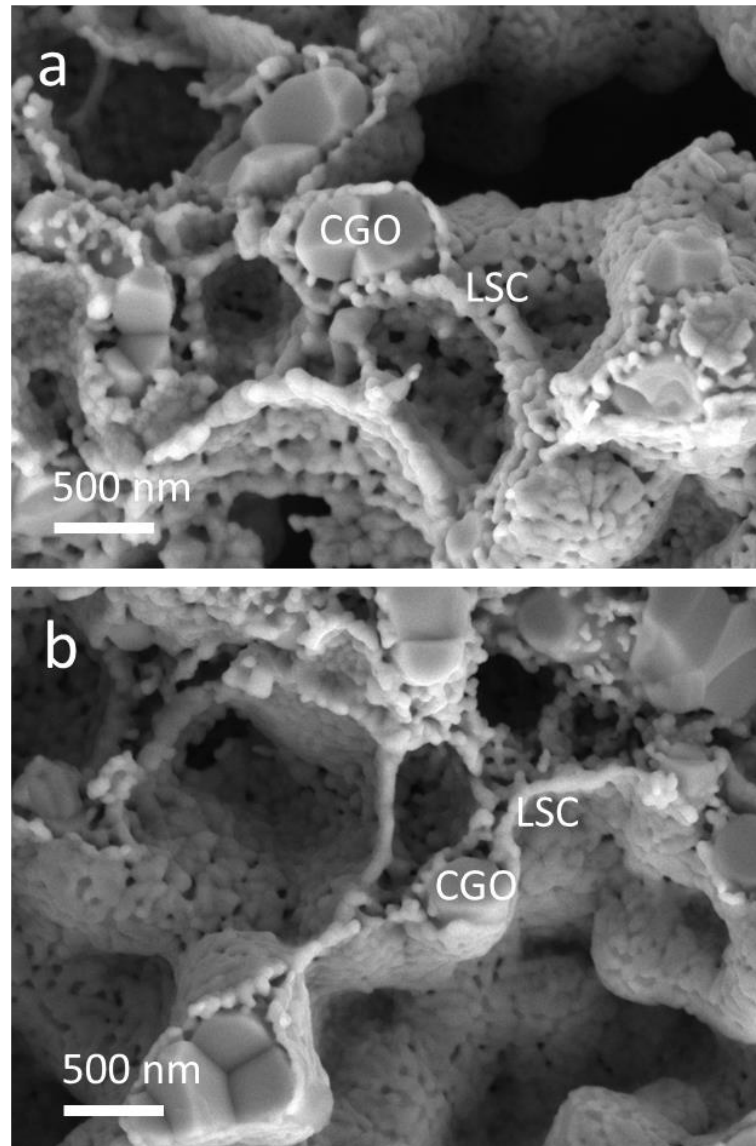


Figure 2.8: Cross-sectional SEM images of LSC infiltrated CGO oxygen electrode for (a) before, and (b) after the durability test.

2.4 Conclusion

In summary, we demonstrated the feasibility of preparing large-area SOCs by conventional ceramic processing techniques involving infiltrating LSC electrocatalysts into a pre-fired CGO porous backbone. The cell was examined at $4 \times 4 \text{ cm}^2$ level (active area). In fuel cell mode, at a voltage of 0.6 V, the cell delivered power densities of 1.34, 1.08, and 0.70 W cm^{-2} at 800, 750, and 700 °C, respectively. These power densities were obtained with fuel and oxygen utilization of 65 and 71 % at 800 °C, 52 and 57 % at 750 °C, and 34 and 37 % at 700 °C, respectively. In electrolysis mode, the current densities at 1.3 V reached 1.37, 1.07, and 0.69 A cm^{-2} at 800, 750, and 700 °C, respectively, corresponding to steam utilization of 76 %, 60%, and 38%. The EIS results suggest that the LSC infiltrated CGO oxygen electrode has excellent activity for both the ORR and the OER and its durability when operated at 0.5 A cm^{-2} for steam electrolysis is good. The $R_{\text{LSC-CGO TPB}}$ is only $0.012 \Omega \text{ cm}^2$ after 80 h operation, constituting less than 5 % of the R_p ($0.267 \Omega \text{ cm}^2$) and 5% ($0.427 \Omega \text{ cm}^2$) of the total cell resistance. The performance of the present cell is limited primarily by ohmic resistance and the resistance for electrochemical processes in the fuel electrode, of which the latter is responsible for the resistance degradation seen over the short durability test. Future work will focus on reducing the ohmic resistance and the fuel electrode polarization resistance, to improve both the cell performance and long-term durability.

Supplementary information

- SEM, EIS spectra

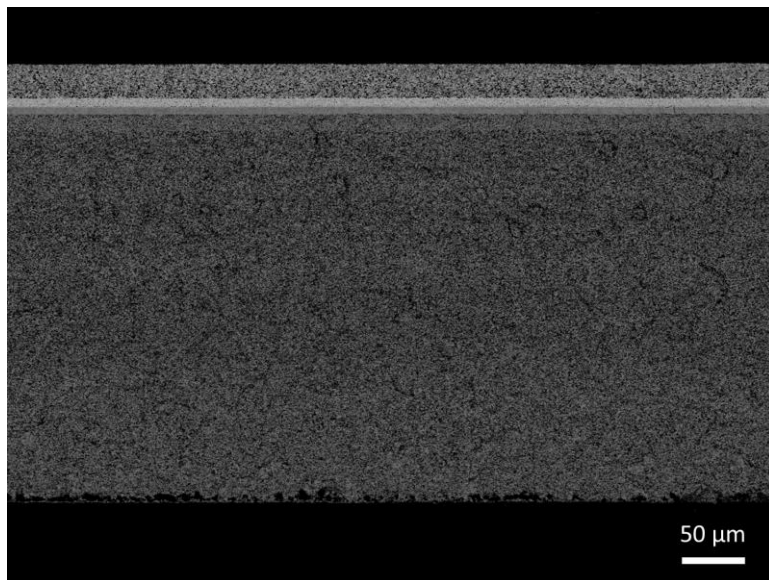


Figure 2.S1: Cross-sectional SEM image of fuel electrode-supported cell prior to the infiltration of LSC.

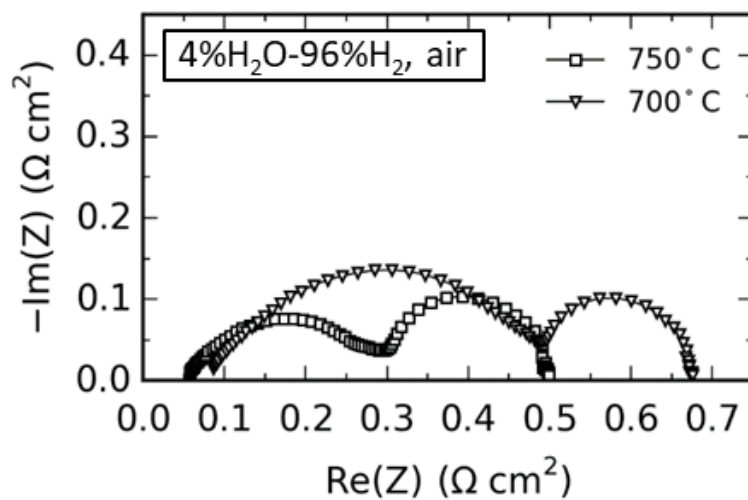


Figure 2.S2: Nyquist plot measured on a Ni/YSZ fuel-electrode supported cell with a thin YSZ electrolyte, a CGO barrier layer applied by pulsed vapor deposition (PVD), and a screen printed LSC/CGO oxygen electrode, at 750 and 700 °C with 4% H_2O -96% H_2 fed to the fuel electrode and dry air to the oxygen electrode. The cell was prepared as in our previously reported work [47].

CHAPTER 3

Nanoengineered solid oxide electrolysis cells for efficient and durable hydrogen production

This chapter is a published article (Paper II. Tong, X., Ovtar, S., Brodersen, K., Hendriksen, P.V. and Chen, M., ACS Appl. Mater. Interfaces, 2019,11, 29, 25996-26004)

Abstract

Despite various advantages of high-temperature solid oxide electrolysis cells (SOECs) over their low-temperature competitors, the insufficient long-term durability has prevented the commercialization of SOECs. Here, we address this challenge by employing two nano-engineered electrodes. The oxygen electrode consists of a $\text{La}_{0.6}\text{Sr}_{0.4}\text{CoO}_{3-\delta}$ (LSC) and Gd,Pr-co-doped CeO_2 (CGPO) nanocomposite coating deposited on a Gd-doped CeO_2 (CGO) scaffold, and the fuel electrode comprises a Ni/yttria stabilized zirconia (YSZ) electrode modified with a nano-granular CGO coating. The resulting cell with an active area of $4 \times 4 \text{ cm}^2$ exhibits a current density exceeding 1.2 A cm^{-2} at 1.3 V and $750 \text{ }^\circ\text{C}$ for steam electrolysis, while also offering excellent long-term durability at 1 A cm^{-2} with a high steam-to-hydrogen conversion of $\sim 56\%$. We further unravel the degradation mechanism of the most commonly used Ni/YSZ electrode at these conditions and describe the mitigation of the discussed mechanism on our nano-engineered electrode. Our findings demonstrate the potential of designing robust SOECs by nano-engineering electrodes through infiltration.

3.1 Introduction

Electrochemical water splitting using surplus electricity from renewable sources (the so-called “power-to-gas” (P2G) technology) has the potential to address energy storage

challenge and to offer a green solution for hydrogen (H_2) production. [131] While the low-temperature (typically $50\text{--}100\text{ }^\circ\text{C}$) alkaline electrolysis cells (AECs) and polymer electrolyte membrane electrolysis cells (PEMECs) are already commercially available, reversing the operation of high-temperature (typically $650\text{--}950\text{ }^\circ\text{C}$) solid oxide fuel cells (SOFCs) as solid oxide electrolysis cells (SOECs, **Figure 3.1**) has received increasing attention in recent years due to their unique advantages. Unlike low-temperature cells, high-temperature SOEC operation enables high efficiency at high production rate. Current densities exceeding 1 A cm^{-2} are regularly reported at close to 100% efficiency (at a thermal-neutral voltage of 1.29 V). [96, 111, 123, 132] Besides, high operating temperature avoids using noble metal based catalysts (as for PEMECs) and enables utilizing a variety of waste heat sources.

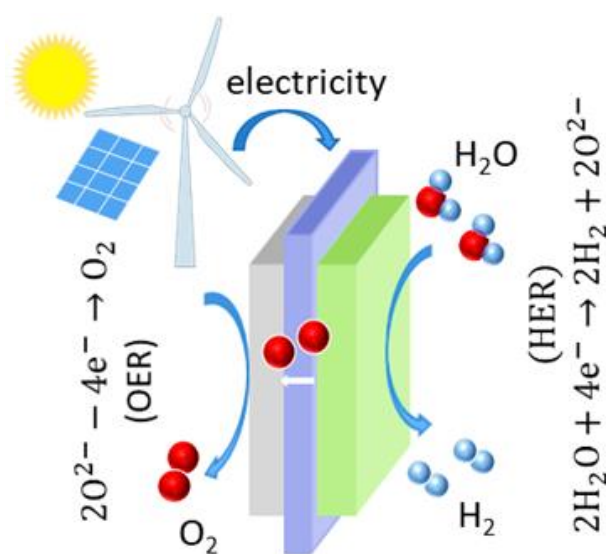


Figure 3.1: Schematic of water splitting using SOECs. When renewable electricity is applied, water/steam is split, releasing H_2 at the fuel electrode (hydrogen evolution reaction, HER). The oxygen ion is driven across the electrolyte, releasing O_2 at the oxygen electrode (oxygen evolution reaction, OER).

Despite these advantages, the insufficient long-term durability has prevented the commercialization of SOECs. Conventional SOECs consists of a thin yttria-stabilized zirconia (YSZ) electrolyte, a strontium-doped lanthanum manganite (LSM)/YSZ composite oxygen electrode and a Ni/YSZ fuel electrode. The reported durability on such SOECs has been disappointing, particularly when operated at above 0.5 A cm^{-2} . For example, Graves et al. [7] reported a degradation rate of 0.952 V kh^{-1} for a 420 h testing period at 1 A cm^{-2} (the

cell voltage increased from 1.33 V to 1.73 V, corresponding to an efficiency decrease from 96% to 75%). Even at 0.7 A cm^{-2} , Hartvigsen et al. [14] reported an increase in the cell resistance from 0.50 to $0.62 \text{ } \Omega \text{ cm}^2$ for 300 h operation, corresponding to a cell voltage increase of approximately 0.28 V kh^{-1} . In most studies, a key degradation mechanism has been reported as microstructural damage near the LSM/YSZ electrode – YSZ electrolyte interface. [7, 15-22] Graves et al. [7] found that this microstructural damage can be eliminated by using a reversible cycle with periods of 1 h in electrolysis mode and 5 h in fuel-cell mode, but such a cycle does not fit the flexibility requirement for practical applications. Benefiting from the development in SOFCs, mixed ionic-electronic conducting (MIEC) oxides have emerged as alternative oxygen electrode materials in SOECs, and infiltration (also known as impregnation) has been used as a route to prepare such MIEC type oxygen electrodes. [61-63] Nevertheless, most studies on infiltrated cells focused on mainly improving initial performance and were carried out at button cell level with an active area less than 2 cm^2 , only few concentrated on issues related to durability and scale-up.

More importantly, the Ni/YSZ fuel electrodes, which display excellent activity for the HER, have also been reported to show severe microstructural degradations at high current densities, likely associated with Ni coarsening and migration and even the reduction of YSZ leading to formation of ZrO_2 nano-particles on the Ni surface. [41-49, 133] Though alternative perovskite oxides have been explored as fuel electrodes, the activity for the HER and performance of these oxides have not reached the levels observed for that of the Ni/YSZ electrodes. Our recent work has demonstrated mitigation of the Ni migration in Ni/YSZ electrode by microstructure optimization, reducing degradation rate from $\sim 0.250 \text{ V kh}^{-1}$ to $\sim 0.060 \text{ V kh}^{-1}$ when operating at 1 A cm^{-2} and $800 \text{ }^\circ\text{C}$. [44] More recently, we have found that surface modification by coating nano-sized electrocatalysts as another effective way for durability enhancement, reducing degradation rate from 0.699 V kh^{-1} to 0.114 V kh^{-1} at 1.25 A cm^{-2} and $800 \text{ }^\circ\text{C}$. [50] However, further improvement in durability is required.

In this work, we report on a cell architecture demonstrated at $4 \times 4 \text{ cm}^2$ level (active area) with two nano-engineered electrodes, prepared via conventional techniques of ceramic processing and infiltration. The oxygen electrode consists of a $\text{La}_{0.6}\text{Sr}_{0.4}\text{CoO}_{3-\delta}$ (LSC) and Gd,Pr-codoped CeO_2 (CGPO) nanocomposite coating deposited on a Gd-doped CeO_2 (CGO) scaffold (herefrom referred to as LSC-CGPO-CGO). LSC was selected as the catalyst for OER due to its excellent mixed ionic and electronic conductivity and fast oxygen

exchange kinetics. [67] The fuel electrode comprises a Ni/YSZ electrode surface modified with a nanogranular CGO coating (herefrom referred to as CGO-Ni/YSZ). This is motivated by the more active oxygen exchange kinetics and redox capacity of CeO₂ and its derivatives (including CGO) in comparison to YSZ. [134-136] The cell exhibits a current density exceeding 1.2 A cm⁻² at 1.3 V and 750 °C for steam electrolysis, while also offering excellent long-term durability at 1 A cm⁻² with a steam-to-hydrogen conversion of ~56%.

3.2 Results and discussion

3.2.1 Full cell design

First, fuel electrode-supported cells with a configuration NiO/YSZ support | NiO/YSZ fuel electrode | YSZ electrolyte | CGO barrier | porous CGO layer, were fabricated by laminating and co-firing tape-casted green sheets at 1315 °C. The original size of the cells after sintering was 12×12 cm². From this smaller pieces (5.3×5.3 cm²) for testing were cut by laser cutting (**Figure 3.2a**). **Figures 3.2b,c** show typical cross-sectional scanning electron microscope (SEM) image of these cells. Note that the NiO/YSZ side of the cells has been reduced to Ni/YSZ prior to the imaging. On the basis of these cells, one cell with two nano-engineered electrodes (named as Cell A, **Figure 3.S1**) was prepared by infiltrating LSC-CGPO nanocomposites into the CGO scaffold and infiltrating CGO into the pre-reduced Ni/YSZ (further detail about infiltration is available in the supporting information). **Figures 3.2d,f** show that the LSC-CGPO covered the internal surfaces of the CGO scaffold well and also seems well interconnected.

Figures 3.2e,g illustrate the microstructure of the Ni/YSZ prior to and after coating with CGO. The CGO nanoparticles were well deposited on the surface of both Ni and YSZ, and in great concentration at the three-phase boundaries (TPBs) where Ni, YSZ, and gas are in contact. This was further evidenced by the corresponding energy-dispersive X-ray spectroscopy (EDX) where strongest Ce signals are found at Ni/YSZ/pore lines (**Figure 3.S2**). These TPBs are the key interfaces that largely govern the performance of Ni/YSZ fuel electrode and are also where the degradation phenomena are primarily observed. For comparison, one cell with the same LSC-CGO-CGO oxygen electrode but without CGO infiltration on Ni/YSZ (named as Cell B) was also prepared

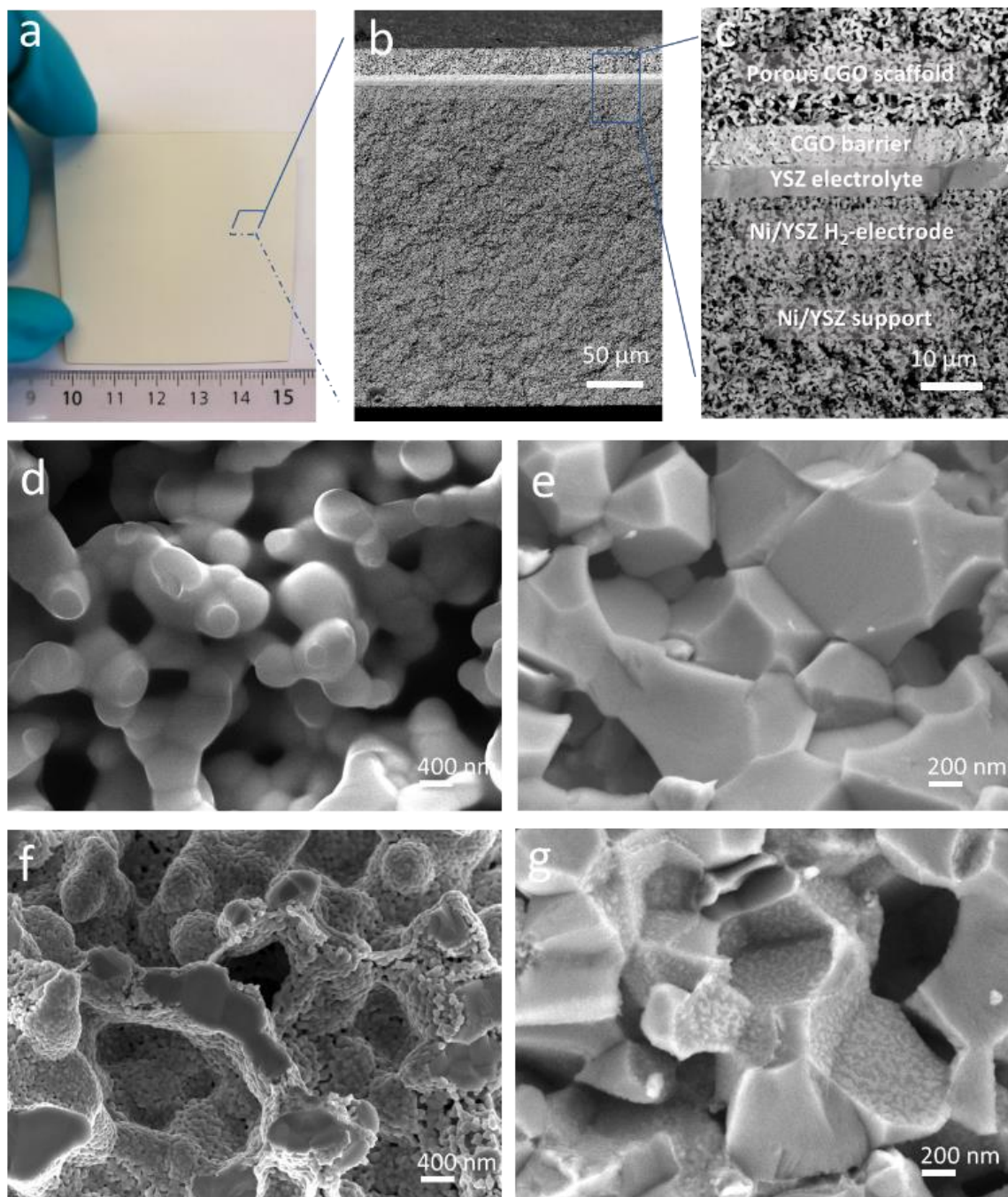


Figure 3.2: (a) A photo and (b,c) SEM images of the fuel electrode-supported cells. Cross-sectional SEM images of (d) porous CGO scaffold, (e) Ni/YSZ fuel electrode, (f) CGO scaffold deposited with LSC and CGPO nanocomposite (LSC-CGPO-CGO oxygen electrode) and (g) Ni/YSZ fuel electrode after CGO infiltration (CGO-Ni/YSZ fuel electrode).

3.2.2 Performance evaluation

The prepared cells were tested using in-house built testing rigs. The active area of the cells was $4 \times 4 \text{ cm}^2$. The edges were used for sealing (experimental details on the testing are provided in the supporting information). **Figure 3.3a** shows the current-voltage (I - V) curves of the electrolysis cells measured at 800–700 °C with 50% H_2O -50% H_2 fed to the fuel electrode and dry air to the oxygen electrode. The open-circuit voltages (OCVs) of the cells are all within 10 mV off the calculated Nernst potentials, implying that the cells were sealed well. Increasing the applied electrolysis current density leads to an increase in the voltage. At 800 and 750°C, the nonlinear increase in the voltage at high current densities indicates potential steam starvation.[137] At a cell voltage of 1.3 V, the current densities of Cell A are 1.37, 1.21, and 0.88 A cm^{-2} at 800, 750, and 700 °C, respectively. At 750 °C, the observed current density at 1.3 V on Cell B is almost identical to that of Cell A.

Figure 3.3b shows the Nyquist plots of the Electrochemical Impedance Spectroscopy (EIS) data recorded at open circuit condition. The total electrode polarization resistances (R_p), taken as the overall width of the depressed arcs, are determined to be 0.078, 0.089, and 0.121 $\Omega \text{ cm}^2$ for Cell A at 800, 750, and 700 °C, respectively, and 0.092 $\Omega \text{ cm}^2$ for Cell B at 750 °C. These R_p values are lower than those reported for most cells with Ni/YSZ fuel electrodes and using different oxygen electrodes, including the commonly used LSCF/CGO composite electrodes, [23, 29, 93] as well as the infiltrated electrodes such as LSCF-YSZ, [111] $\text{Sm}_{0.5}\text{Sr}_{0.5}\text{CoO}_{3-\delta}$ (SSC)-YSZ, [121] $\text{Nd}_2\text{NiO}_{4+\delta}\text{-Zr}_{0.88}\text{Sc}_{0.22}\text{Ce}_{0.01}\text{O}_{2.11}$ (NNO-SSZ), [123] $\text{La}_{0.8}\text{Sr}_{0.2}\text{Co}_{0.8}\text{Ni}_{0.2}\text{O}_{3-\delta}$ -CGO (LSCN-CGO). [138]

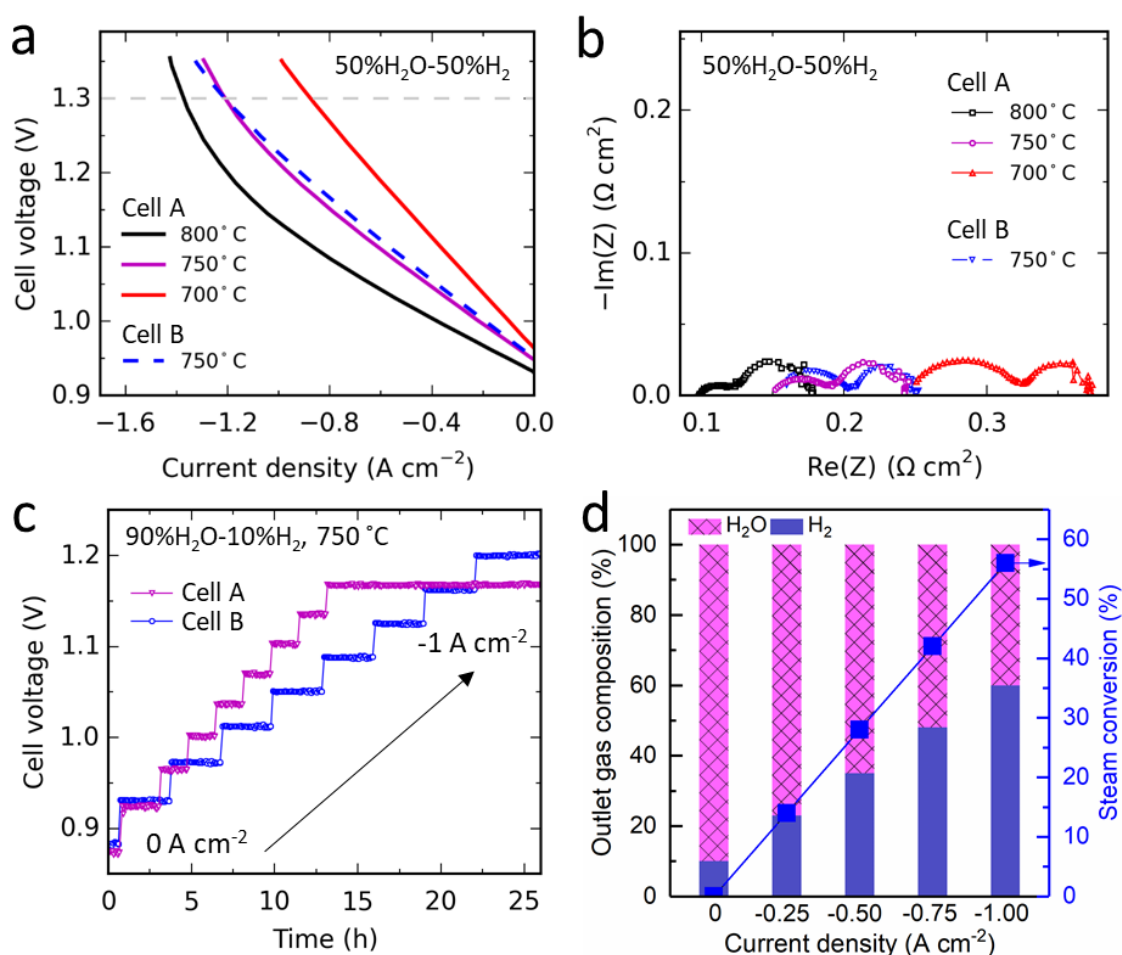


Figure 3.3: Performance of Cell A and Cell B for steam electrolysis. (a) *I-V* curves and (b) Nyquist plots of EIS data of the electrolysis cells measured at 800–700 °C with 50% H_2O -50% H_2 fed to the fuel electrode and dry air to the oxygen electrode. (c) Dependence of cell voltage on applied current density for cells at 750 °C with 90% H_2O -10% H_2 fed to the fuel electrode and pure O_2 to the oxygen electrode. (d) Corresponding gas composition at the outlet and overall steam conversion under the applied current densities.

The performance of the cells was further investigated by galvanostatic tests at 750 °C with 90% H_2O -10% H_2 fed to the fuel electrode and pure O_2 to the oxygen electrode. In **Figure 3.3c**, the evolution of the cell voltage when stepping up the current density from 0 up to 1.00 A cm^{-2} is shown. Note that the production rate of H_2 is proportional to the applied current density assuming a Faraday efficiency of 100%. At 1.00 A cm^{-2} , the H_2 production rate reaches $0.448 \text{ mol cm}^{-2}$ per day, corresponding to a steam-to-hydrogen conversion of $\sim 56\%$ and a hydrogen content of $\sim 60\%$ in the outlet gas (**Figure 3.3d**). The superiority of

Cell A (with CGO-Ni/YSZ fuel electrode) becomes more evident with increasing current density.

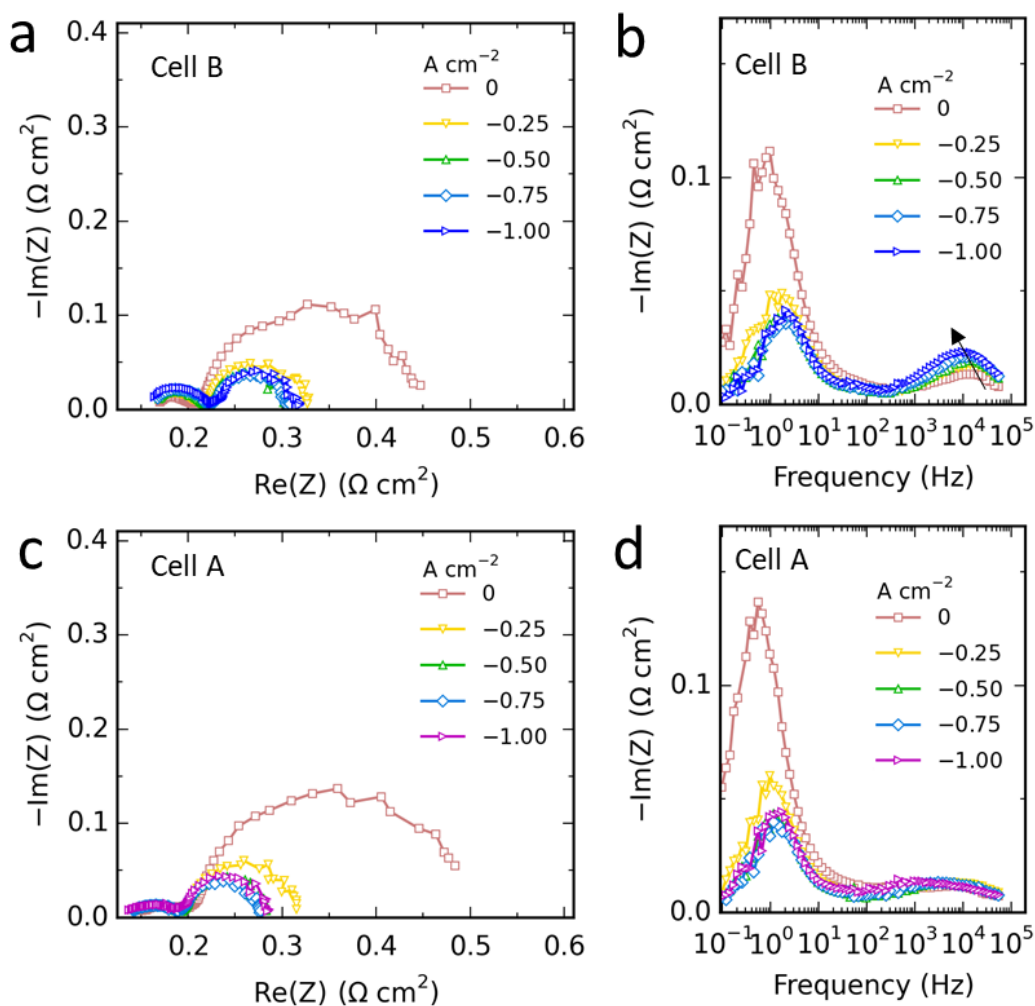


Figure 3.4: (a, b) Nyquist plots and (c, d) Bode plots of cells recorded at different current densities with 90% H₂O-10% H₂ fed to the fuel electrode and pure O₂ to the oxygen electrode.

Figure 3.4 compares Nyquist and Bode plots of EIS data obtained for Cell A and Cell B recorded at different current densities. The EIS response below $\sim 10^2$ Hz corresponds to the chemical processes including gas diffusion and conversion, and the EIS response in the frequency range ($\sim 10^2$ – 10^5 Hz) relates to the electrochemical processes in electrodes, [124, 139] supported by detailed EIS analysis in **Figure 3.S3**. For Cell B, increasing the current density resulted in a considerably increase of the imaginary part in the frequency range $\sim 10^2$ – 10^5 Hz and the peak frequency shifted from $\sim 2 \times 10^4$ Hz to $\sim 9 \times 10^3$ Hz. Cell A was in the corresponding frequency range $\sim 10^2$ – 10^5 Hz much less sensitive to the increased current

density. As these two cells differ only in the fuel electrode intentionally, different behavior with respect to current dependence can be ascribed to the effect of infiltrating nanostructured CGO into the Ni/YSZ electrode. Cell A and Cell B showed a similar behavior below $\sim 10^2$ Hz with increasing current density. The changes in this frequency range can be ascribed to changes of H₂O:H₂ ratio in the fuel electrode that affects both conversion and diffusion resistances. [140]

3.2.3 Durability assessment

Durability tests were performed at 750 °C with a constant current density of 1.00 A cm⁻², and 90% H₂O-10% H₂ fed to the fuel electrode and pure O₂ to the oxygen electrode. **Figure 3.5a** compares the evolution of cell voltage with time for the two cells. The voltage of Cell B increased from 1.200 V to 1.445 V during 537 h testing, corresponding to a degradation rate of 0.565 V kh⁻¹ (Note that the period from 194 h - 297 h where the cell was at open circuit condition has been excluded in the calculation of degradation rate). For Cell A, the cell voltage increased from 1.167 V to 1.189 V over 900 h, corresponding to a degradation rate of 0.024 V kh⁻¹, more than 20 times lower than that for Cell B.

The durability of Cell A is actually superior to most previously studied SOECs despite being tested at harsher conditions. As mentioned in the introduction, a degradation rate of 0.952 V kh⁻¹ was reported on a conventional SOEC (Ni/YSZ support | Ni/YSZ fuel electrode | YSZ electrolyte | LSM/YSZ oxygen electrode) under identical current but 50 °C higher testing temperature (800 °C). [7] Besides, a degradation rate of 0.125 V kh⁻¹ (i.e., 5 times that of Cell A) was reported for a Ni/YSZ fuel electrode supported SOEC with a thin YSZ electrolyte, and a LaNi_{0.5}Co_{0.5}O_{3-δ} infiltrated YSZ oxygen electrode under the same high current density of 1.00 A cm⁻² and steam conversion of 56% but at slightly higher temperature, ~ 800 °C. [70] A degradation rate of 0.040 V kh⁻¹ (~ 2 times that of Cell A) was reported under 1.00 A cm⁻² and a lower steam conversion of 36% and at higher temperature of ~ 775 °C on a Ni/YSZ fuel electrode supported SOEC with a thin YSZ electrolyte, a CGO barrier and a screen printed La_{0.58}Sr_{0.4}Co_{0.2}Fe_{0.8}O₃ oxygen electrode. [45] Note that the steam conversion has significant effect on cell durability, e.g. lowering the steam conversion from 70% to 42% resulted in a decrease of degradation rate from 0.114 V kh⁻¹ to 0.064 V kh⁻¹ as reported in a previous work. [50] There is one exception; Wood's et al. reported a cell named

“HiPoD” achieving a low degradation rate of 0.027 V kh^{-1} at extremely high current density of 3 A cm^{-2} at $750 \text{ }^\circ\text{C}$. [141] Unfortunately, only little detail on cell structure has been provided in ref [141]. The I - V curves collected before and after the durability tests are shown in **Figures 3.5b,c**. The change in current density at 1.3 V also verifies the good durability of Cell A. Cell A even showed a slight increase of current density after 900 h operation. By contrast, the current density in the I - V test degraded more than 40% after 537 h for Cell B.

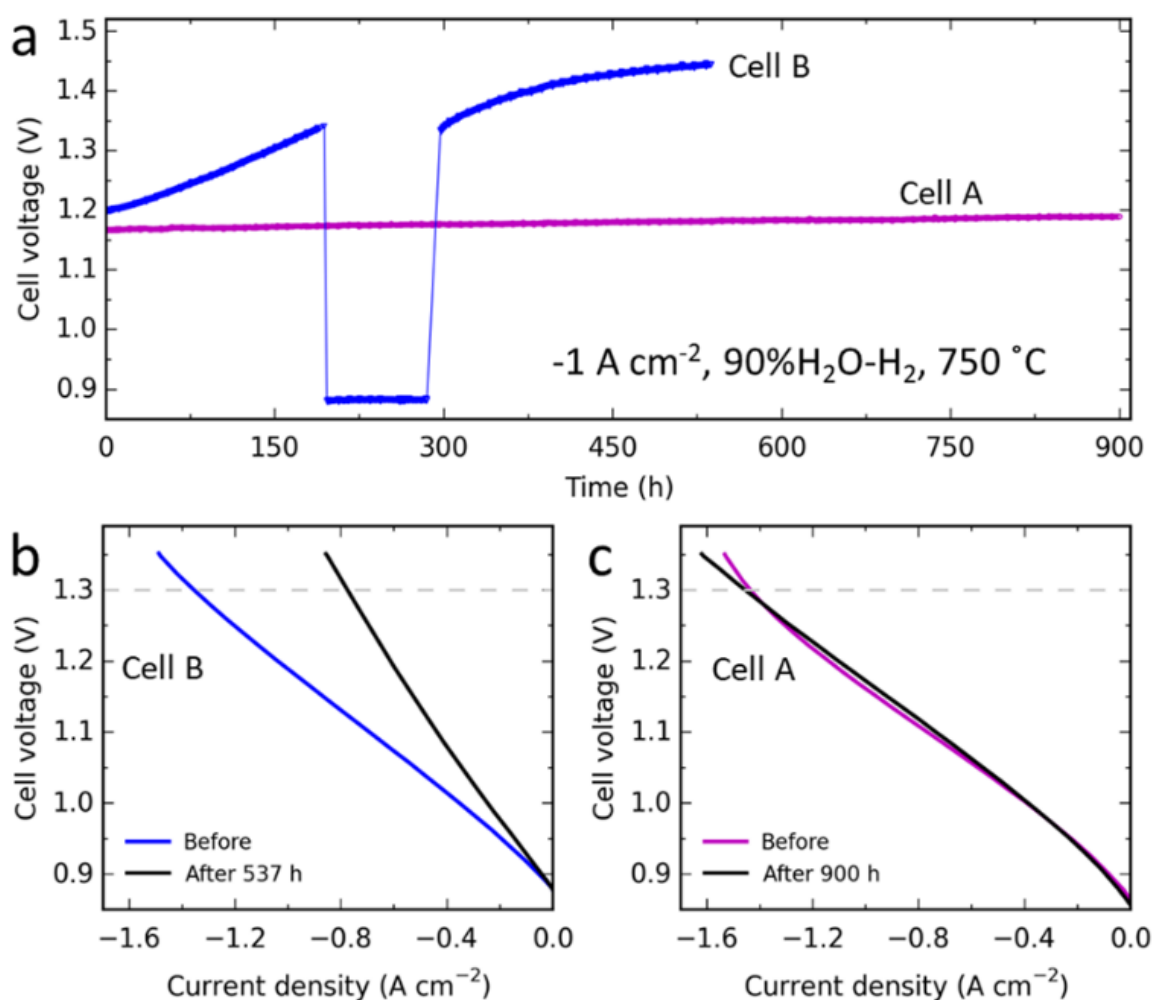


Figure 3.5: Comparison of the cell durability during steam electrolysis. (a) Evolution of cell voltage during long-term test under a constant current density of 1.00 A cm^{-2} at $750 \text{ }^\circ\text{C}$. (b, c) I - V curves collected before and after the durability tests. A $90\% \text{H}_2\text{O}-10\% \text{H}_2$ gas mixture was fed to the fuel electrode and pure O_2 was supplied to the oxygen electrode.

Figures 3.6a,b show the Nyquist plots of the EIS data obtained at the start and end of the durability test period. An increase in the R_p of $\sim 0.779 \text{ } \Omega \text{ cm}^2 \text{ kh}^{-1}$ is observed for Cell B,

indicating significant degradation, whereas the R_P of Cell A only had a slight increase of $\sim 0.020 \Omega \text{ cm}^2 \text{ kh}^{-1}$. These results correspond well with the voltage evolution results plotted in **Figure 3.5a**.

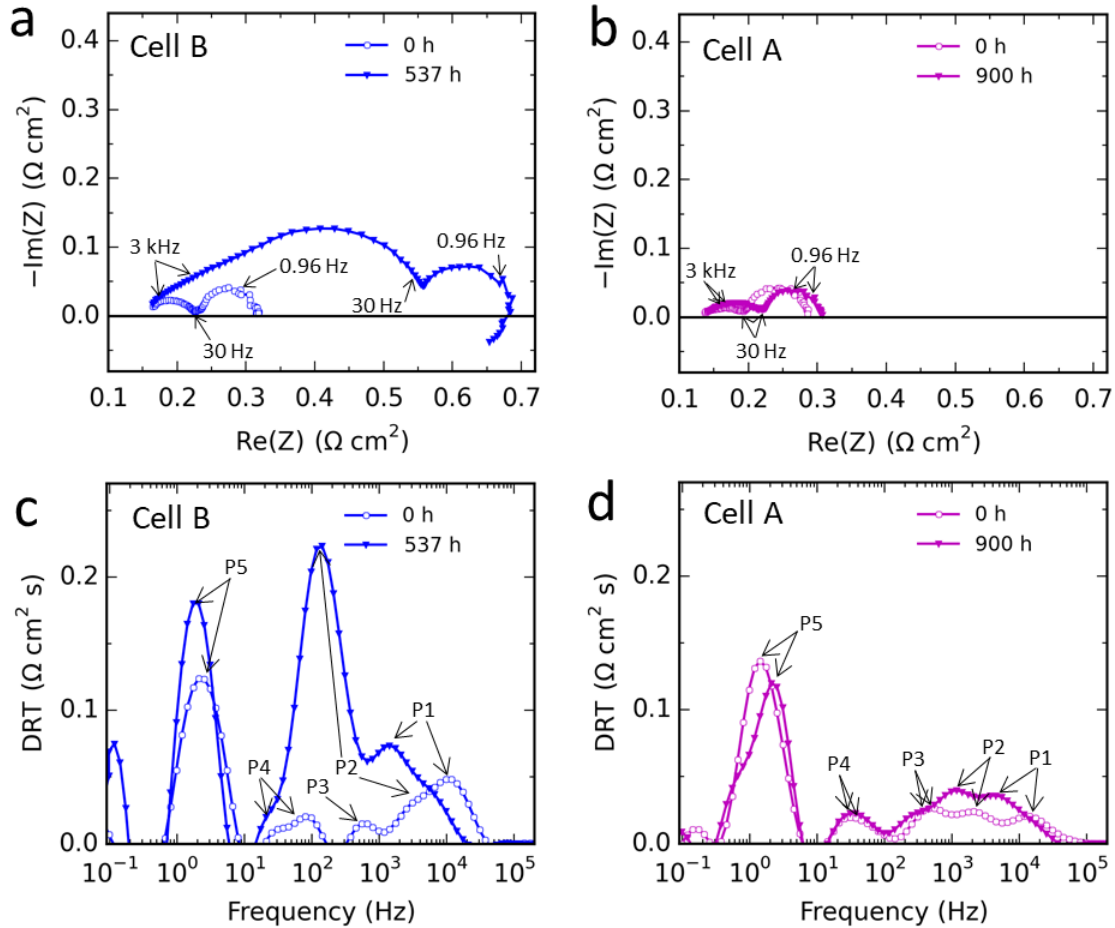


Figure 3.6: (a, b) Nyquist plots recorded at start and end of the durability test period. (c, d) Distribution of relaxation time for the impedance data shown in (a) and (b).

In order to further clarify the type of contributions to R_P and their evolution over time, the distribution of relaxation time (DRT) has been calculated for the EIS data. [142] The results are shown in **Figures 3.6c,d**. For both cells, five peaks (P1, P2, P3, P4 and P5) in the frequency range from 0.3–96850 Hz were identified on the initial spectra. Each peak represents an electrochemical or chemical process in the fuel or oxygen electrode, whereas the area under each peak corresponds to the magnitude of resistance for that electrode process. [143] On the basis of previously reported analyses: [44, 46, 140] P1 is tentatively ascribed to the transport of oxygen anions across electrolyte-electrode interfaces and through

the ionic conducting network in the electrodes. Since the applied cells have a highly ionic conducting CGO scaffold based oxygen electrode, the major contribution of P1 could well originate from the fuel electrode that has a YSZ network; P2 is associated with the HER process at the triple phase boundaries (TPBs) of the fuel electrode; P3 is likely associated with the OER, while P4 represents the gas diffusion and P5 the gas conversion in the fuel electrode. For Cell B, among the five peaks, P1 and P2 increased markedly and shifted to lower frequency, indicating that the major degradation is from the Ni/YSZ fuel electrode. Whereas, for Cell A the P1 and P2 only revealed a slight increase; well in line with the fact that the only intended difference between the cells is on the fuel electrode.

To enable a quantitative analysis of the various contributions to cell degradation, these spectra were further fitted with equivalent circuit models by the complex-non-linear-least-squares (CNLS) method. [44, 46, 144] The spectrum of Cell B at 0 h and spectra of Cell A were fitted with the circuit A, while the spectrum of Cell B at 537 h was fitted with the circuit B (**Figure 3.7a**). In circuit B the R_6L_6 was added to describe the inductance loop at low frequency. This process has been shown to originate from reduction of YSZ in Ni/YSZ electrode. [144] The detailed fitting results are shown in **Figures 3.S4,S5**. **Figures 3.7b,c** and **Table 3.S1** summarize the simulated values of R_{ohm} and resistances associated with each of the electrode processes. In contrast to many studies on SOECs with Ni/YSZ fuel electrodes, in which R_{ohm} is observed to increase considerably during continuous operation at high current densities, [21, 47, 94] we observed that the increase of R_{ohm} on Cell B was only $0.012 \Omega \text{ cm}^2$ after 537 h. This is ascribed to the optimized Ni/YSZ fuel electrode as previously discussed. [44] By introducing the nanostructured CGO coating into the Ni/YSZ fuel electrode, the increase of R_{ohm} on Cell A was further reduced to $0.003 \Omega \text{ cm}^2$ in 900 h.

The increase of resistance for transport of oxygen anions (R_{ion} , corresponding to P1) and the resistance for the HER at the TPBs in Ni/YSZ fuel electrode (R_{HER} , corresponding to process P2) on Cell B were $0.059 \Omega \text{ cm}^2$ and $0.251 \Omega \text{ cm}^2$, respectively, and contributed to ~90% of the total increase of R_P , showing that the Ni/YSZ fuel electrode dominates the cell degradation. Cell A with the CGO-Ni/YSZ fuel electrode had initially a lower initial R_{ion} of $0.013 \Omega \text{ cm}^2$, less than 31% of the one found for Cell B ($0.042 \Omega \text{ cm}^2$). More importantly, the increase of R_{ion} and R_{HER} on Cell A was much less; only $0.013 \Omega \text{ cm}^2$ and $0.012 \Omega \text{ cm}^2$ in 900 h, respectively. These results further demonstrate that the nano-CGO coating improves significantly the electrode durability at 1 A cm^{-2} , as also argued from the fact that

this electrode is the one that differs between the two cells. Note that the resistances for gas diffusion (R_{DIFF} , corresponding to P4) on Cell A were slightly higher than those on Cell B, which is attributed to the reduced porosity in the Ni/YSZ electrode after coating with CGO, also explaining the stronger tendency of steam starvation (the observed nonlinearity at high current density) in the I - V measurement of Cell A (**Figure 3.5b**).

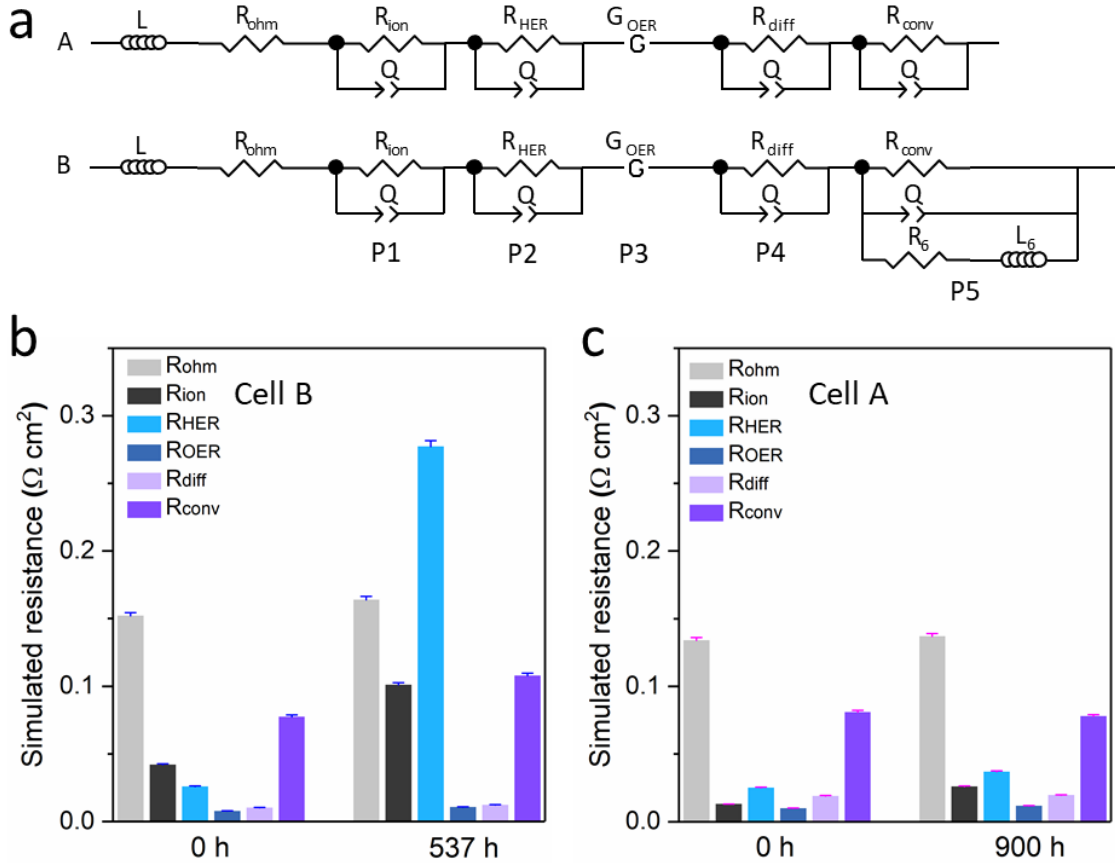


Figure 3.7: (a) Electrical equivalent circuits used in the fitting. (b, c) Results from equivalent circuit fit modeling of the impedance spectra.

As can also be seen in **Figures 3.7b,c**, the resistances for the OER at the LSC-CGPO-CGO oxygen electrode (R_{OER} , corresponding to P3) were around $0.010 \Omega \text{ cm}^2$ for both cells initially (0 h). These values are lower than those reported for a screen-printed LSC/CGO composite electrode tested under identical gas and current conditions but at $50 \text{ }^\circ\text{C}$ higher testing temperature ($800 \text{ }^\circ\text{C}$).[44] Furthermore, the increase of R_{OER} were as low as $0.003 \Omega \text{ cm}^2$ on Cell B, and $0.002 \Omega \text{ cm}^2$ on Cell A. These fitting results further confirm the good activity and stability of the LSC-CGPO-CGO oxygen electrode for the OER in SOECs

operated at 1 A cm^{-2} . The improved electrode stability was also supported by SEM images as shown in **Figure 3.S6**, where no obvious change in the microstructure of the LSC-CGPO-CGO electrodes was observed after the durability tests.

3.2.4 Microstructural evolution and discussion of degradation mechanisms

Figure 3.8 shows SEM images of the Ni/YSZ electrode in Cell B and the CGO-Ni/YSZ electrode in Cell A after the durability test. In the SEM images obtained by the low-voltage contrast technique, [145] a slight loss of Ni percolation is observed in Cell B after the durability test, particularly close to the electrode/electrolyte interface (**Figure 3.8a**), as compared with the initially pre-reduced electrode (**Figure 3.S7**). In contrast, the Ni percolation in Cell A in the CGO modified electrode is practically intact (**Figure 3.8b**). Furthermore, after the durability test, we observe clear disconnections (or gaps, or detachment) between Ni and YSZ in Cell B (**Figure 3.8c**) but none for the CGO modified electrode in Cell A (**Figure 3.8d**). High magnification images of the electrode combined with EDX characterization reveals the formation of ZrO_2 nanoparticles on the Ni grains at disconnected interfaces (**Figure 3.8e**, and **Figure 3.S8**). No evidence of formation of ZrO_2 nanoparticles in the CGO modified electrode is observed. The nano-CGO particles have clearly coarsened after the durability test, but they are still in the nanoscale with a size around 60 nm. They seem partly connected forming a surface network (**Figure 3.8f**).

Based on the microstructural observations, we suggest that: the degradation mechanism on Cell B leading to the fast increase of R_{ion} and R_{HER} is the disconnection between Ni and YSZ at the TPBs, which is caused by a combined effect of Ni migration, and YSZ reduction and formation of ZrO_2 nanoparticles on the Ni surface under the high cathodic overpotential estimated to be varying from 0.066 V to 0.378 V during the durability test (see **Figure 3.9a**). [41, 42, 144] This “disconnection” is effectively suppressed by modifying the Ni/YSZ with the nano-CGO coating. The slight increase in R_{ion} and R_{HER} of Cell A is likely due to the coarsening of the nano-CGO. The above results further confirm that the present nano-CGO-Ni/YSZ architecture is highly active for the HER and demonstrates great promise as an efficient and robust fuel electrode for steam electrolysis in SOECs.

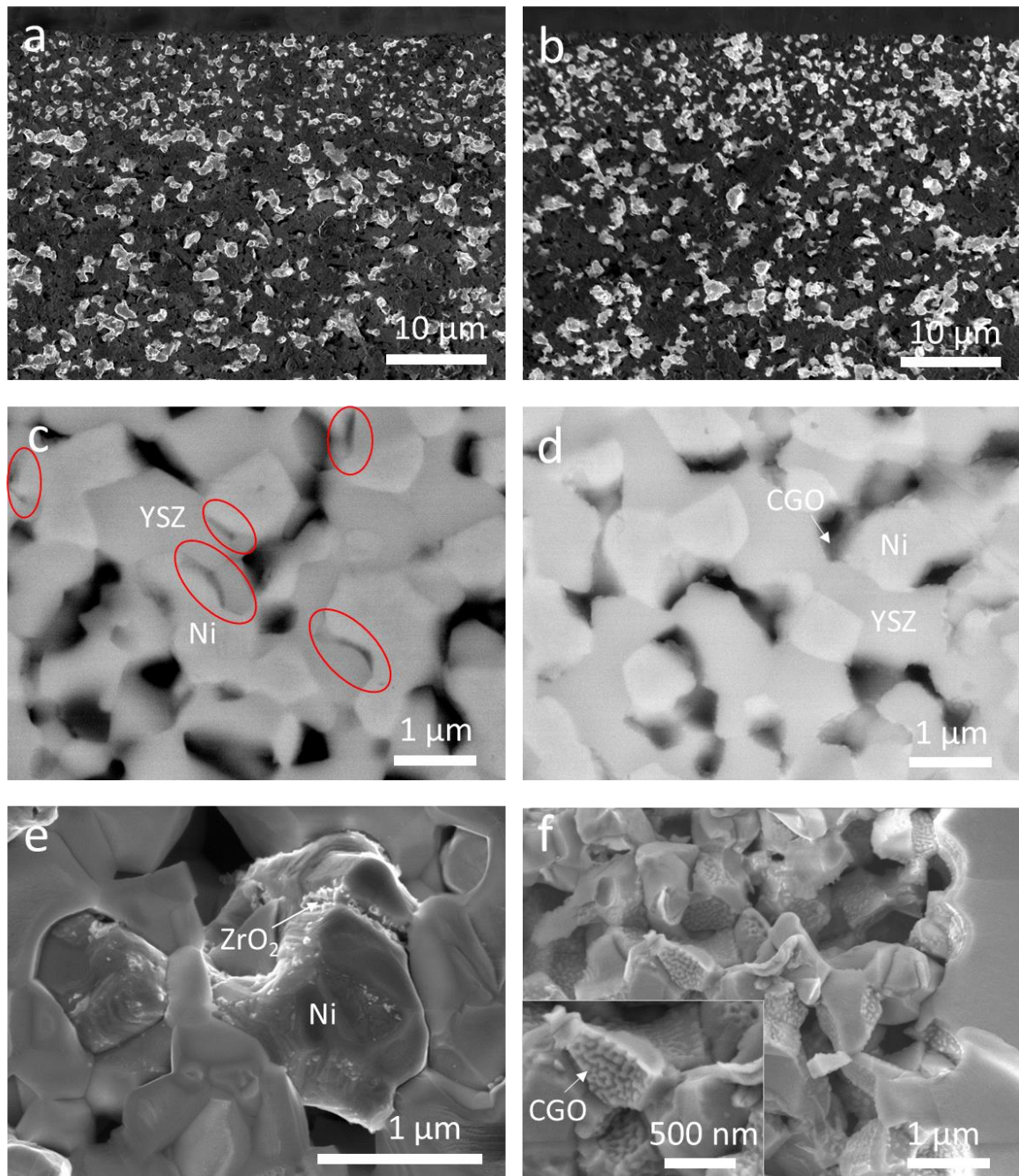


Figure 3.8: SEM characterization of the fuel electrode in Cell B and Cell A after the durability test. SEM images showing Ni percolation in (a) the Ni/YSZ fuel electrode and (b) the CGO-Ni/YSZ fuel electrode. SEM images of polished cross-sections showing the Ni-YSZ interface in (c) the Ni/YSZ fuel electrode and (d) the CGO modified electrode. SEM images showing fracture surface of (e) the Ni/YSZ fuel electrode and (f) the CGO modified one. The inset is an image with high resolution.

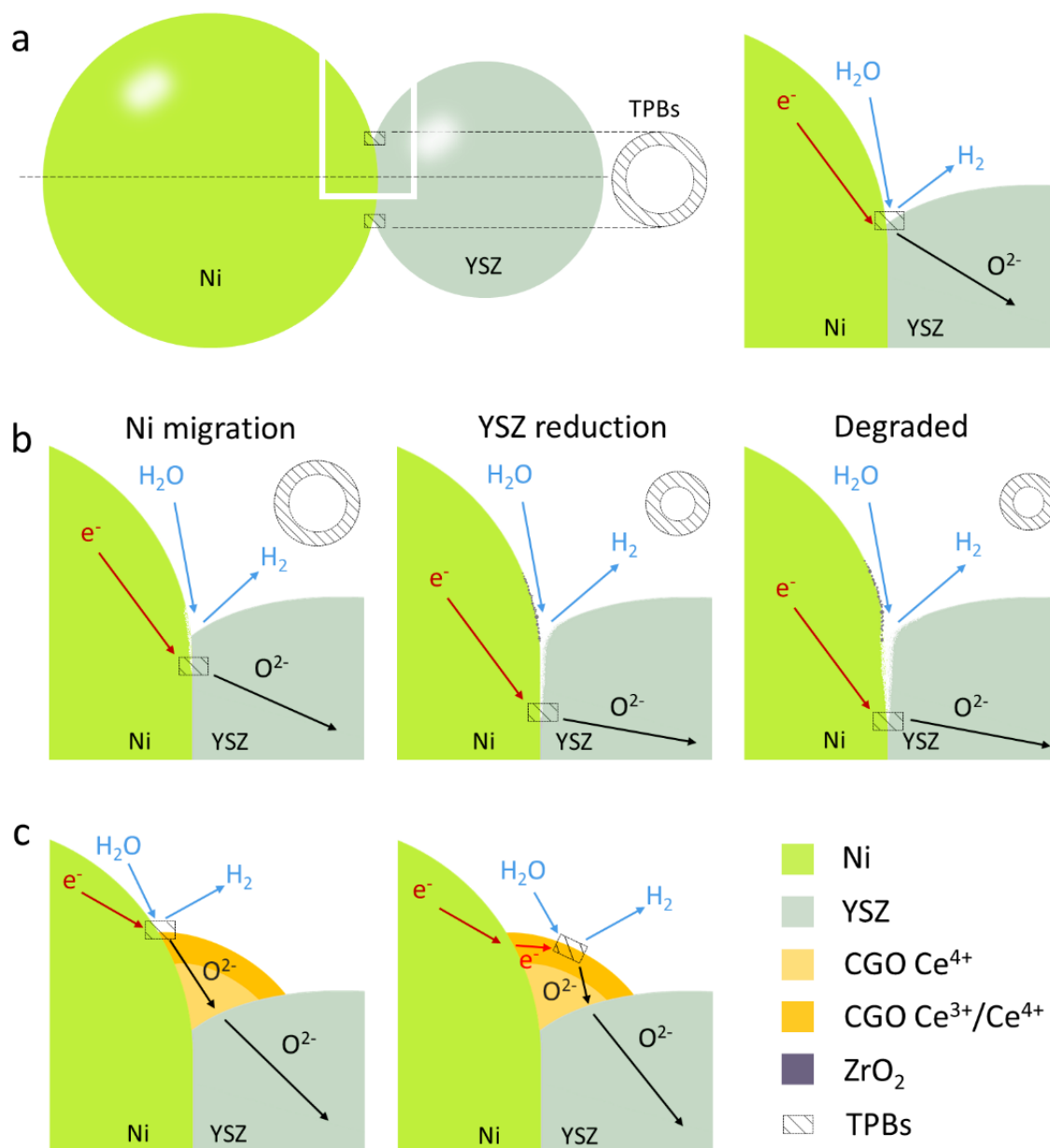
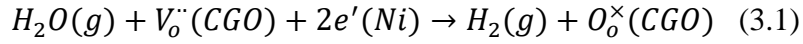


Figure 3.9: (a) Schematic illustration of the HER reaction at the three-phase boundary (TPB) in the Ni/YSZ electrode and (b) the suggested mechanism of microstructural deterioration of the electrode during high-current-density electrolysis operation. (c) Mitigation of the discussed mechanism by CGO modification.

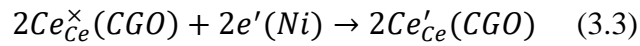
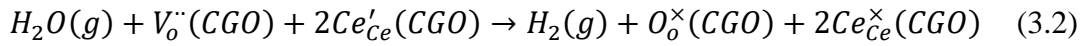
It has been demonstrated that the CGO can act as catalyst for dissociation of H_2O . [146, 147] Furthermore, the CGO will under the applied electrolysis conditions show mixed electronic and oxygen ion conductivity. [148] Therefore, introducing such a CGO coating into the Ni/YSZ electrode presumably provides additional active sites for the HER (**Figure**

3.9b), [149] e.g., TPBs at the nano-CGO, Ni and gas interface (Ni-CGO-gas); and at the two-phase boundary (2PB) at the surface of the CGO located on Ni grains (CGO-gas), thereby enhancing activity and structural stability. The reaction at these sites with nano-CGO may proceed in multiple consecutive or parallel steps as follows:

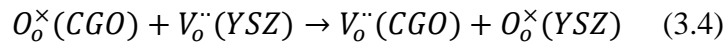
Dissociation of H₂O molecules at Ni-CGO-gas interface



or at the CGO-gas interface



and finally transport of oxygen vacancies within CGO coatings and transfer to YSZ



Where $V_o^{\bullet\bullet}(YSZ \text{ or } CGO)$ and $O_o^{\times}(YSZ \text{ or } CGO)$ represent oxygen ions and oxygen vacancies in the YSZ or CGO lattice, respectively. Compared to the YSZ in Ni/YSZ that has been sintered at 1315 °C, the more active surface oxygen exchange kinetics and excellent surface oxygen redox capacity of the nano-CGO is likely to facilitate the dissociation of H₂O molecules and the charge transfer process, thus significantly enhancing the durability of the Ni/YSZ fuel electrode under high current loading. Future work on electrocatalytic activity of water splitting on CGO using density-functional theory (DFT) calculation may help to prove this.

3.3 Conclusion

In summary, we demonstrated that planar SOECs incorporating two nano-engineered electrodes (a LSC-CGPO-CGO oxygen electrode and a CGO modified Ni/YSZ fuel electrode) prepared via conventional techniques of ceramic processing and chemical infiltration, exhibit both excellent initial performance at 750 °C and decent long-term durability at high current density of 1 A cm⁻², when tested at a technologically relevant level of 4×4 cm² (active area). The low R_{OER} resistance of 0.012 Ω cm² after 900 h operation and no obvious change in the microstructure suggest that the nanostructured LSC-CGPO-CGO is highly active and durable for the OER, which demonstrates the potential of designing robust oxygen electrode via infiltration for large-scale manufacture of SOECs. The introduced CGO coating effectively mitigates the microstructural deterioration (typically disconnection between Ni and YSZ at the TPBs) seen on non-modified Ni/YSZ electrodes under these conditions, thus significantly enhancing cell durability. These findings represent an important advance towards development of long-term stable SOECs.

3.4 Experimental

3.4.1 Preparation of the LSC-CGPO-CGO oxygen electrode

The inner surface of the porous CGO scaffold was first infiltrated with 0.7 M Gd,Pr co-doped CeO₂ (CGPO) nitrate solution containing stoichiometric amounts of Ce(NO₃)₃, Gd(NO₃)₃, and Pr(NO₃)₃ (16:4:5 molar ratio to metal ions), followed by calcination at 350°C in air for 15 min. The Triton X-100 surfactant (0.7 wt.%) was added into the CGPO solution to improve wetting/penetration of the structure. The infiltration was performed by dripping the CGPO solution onto the surface of the CGO scaffold. The solution will cover and wet all the surface due to the capillary force, and then the solution will be sucked into the scaffold. After 30 seconds, the residual solution was wiped off from the surface. The loading of CGPO was ~111 mg per 1 cm³ CGO scaffold. Hereafter, the scaffold was further infiltrated with a 0.5 M LSC nitrate solution containing stoichiometric amounts of La(NO₃)₃, Sr(NO₃)₂, and Co(NO₃)₃ (3:2:5 molar ratio of La³⁺:Sr²⁺:Co³⁺), followed by calcination. The Pluronic P-123

surfactant (1.7 wt.%) was added into the LSC solution. [113] The infiltration of LSC and the following calcination processes were repeated 9 times to get a loading of ~ 1185 mg per 1 cm^3 CGO scaffold. Finally, a LSC current-collector layer was applied on the top of the oxygen electrode by screen-printing

3.4.2 Preparation of the CGO-Ni/YSZ fuel electrode

The NiO/YSZ electrode was reduced by a “one sided” reduction in a specific in-house rig at $850 \text{ }^\circ\text{C}$, with 24 l/h $\text{H}_2\text{O}/\text{H}_2$ (4/96) fed to the Ni/YSZ fuel electrode and 50 l/h dry air to the oxygen electrode. Afterwards, the pre-reduced Ni/YSZ was infiltrated with a 0.3 M CGO nitrate solution containing stoichiometric amounts of $\text{Ce}(\text{NO}_3)_3$ and $\text{Gd}(\text{NO}_3)_3$ (4:2 molar ratio to metal ions), followed by calcination at 300°C in air for 15 min. The PE-L62 surfactant (1.4 wt.%) was added into the CGO solution. [50] The infiltration processes were repeated 7 times to get a loading of 120 mg CGO per 1 cm^3 Ni/YSZ structure (Ni/YSZ fuel electrode + Ni/YSZ support).

3.4.3 Electrochemical performance and durability testing of the cells

The electrochemical performance and durability of the cells were tested via in-house testing rigs, as described in previous work. [114, 140] For all the tests, the cells were mounted and sealed to an alumina housing. Corrugated nickel mesh and nickel plate were used as the contact components on the fuel electrode side. Corrugated gold mesh and gold plate were used on the oxygen electrode side. A gold frame was used for sealing on fuel electrode side. To ensure a good seal and a good electrical contact, four kilograms of weight was applied on top of the cell house during start up. The cells were heated ($1 \text{ }^\circ\text{C min}^{-1}$) to $800 \text{ }^\circ\text{C}$ for sealing with 9 % H_2 in Ar to fuel electrodes and air to oxygen electrodes for 2 h, followed by another 2 h with humidified H_2 (4 % H_2O) to fuel electrodes. Meanwhile, this reduction process will enable the infiltrated materials to form desired crystalline phases. The electrochemical performance of the cells was characterized at $800\text{--}700 \text{ }^\circ\text{C}$. A Solartron 1255 frequency response analyzer in combination with a measurement resistor was used for recording EIS, at frequencies from 96850 to 0.0968 Hz with an amplitude of 3.75 mA cm^{-2} . The galvanostatic durability tests were conducted at $750 \text{ }^\circ\text{C}$, with 50 l/h pure oxygen supplied to the oxygen electrode and 13.4 l/h 90% H_2O -10% H_2 to the fuel electrode under a

constant current density of 1 A cm^{-2} . The EIS spectra were also measured during the durability testing period. The in-house developed Python-based software Ravdav was used for plotting and analysis of the EIS data. [115]

3.4.4 Microstructure characterization

The cross-section of cells were examined using a Zeiss Merlin scanning electron microscope (SEM). For the fractured samples an accelerating voltage of 5 kV was used. To examine the percolation of Ni in Ni/YSZ electrodes, a low-voltage of 1 kV and an Inlens secondary electron detector in the SEM were used. [145] For the polished samples, they were first coated with carbon, and analyzed at an accelerating voltage of 15 kV. For energy-dispersive X-ray spectroscopy (EDX) analysis, an accelerating voltage of 10 kV was used for the data presented in **Figure 3.S2** and a voltage of 5 kV was used for those in **Figure 3.S8**.

Supplementary information

- Photo of the as-prepared Cell A, SEM, EDX elemental mappings, EIS spectra, CNLS fits of spectra, Table summarizing the fitting results

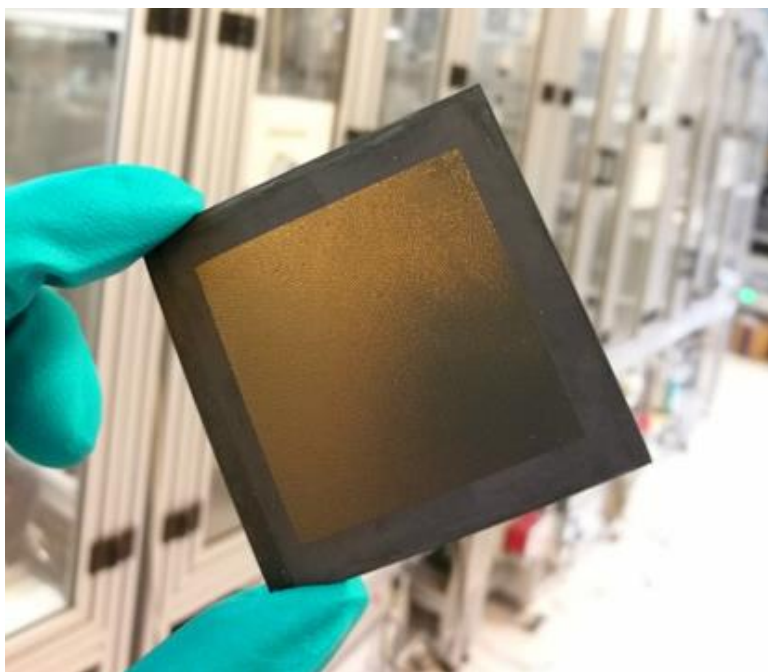


Figure 3.S1: A photo of the as-prepared Cell A (with the LSC-CGPO-CGO oxygen electrode and the CGO-Ni/YSZ fuel electrode)

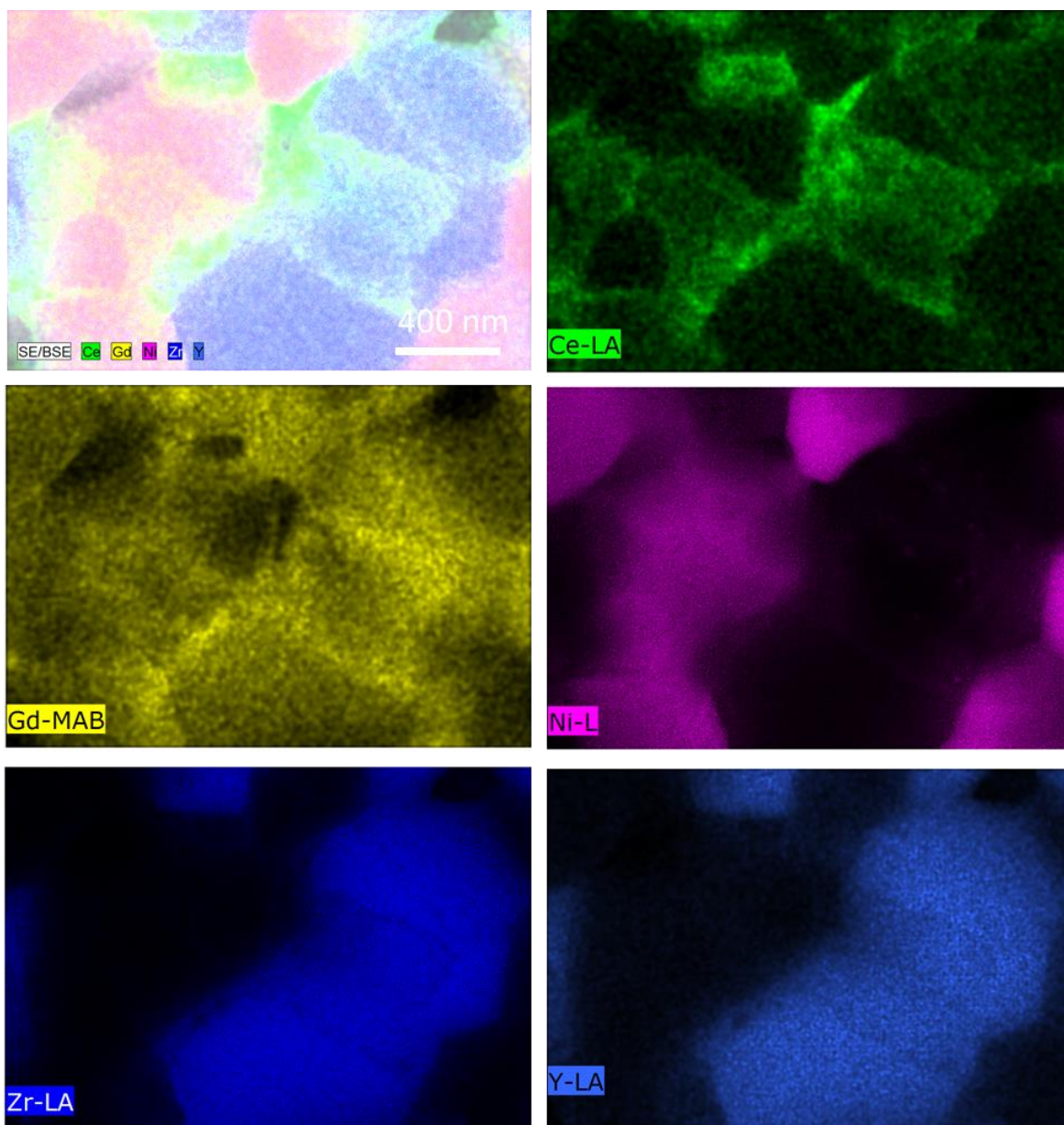


Figure 3.S2: Corresponding EDX elemental mappings of Ni/YSZ fuel electrode deposited with CGO coating (CGO-Ni/YSZ)

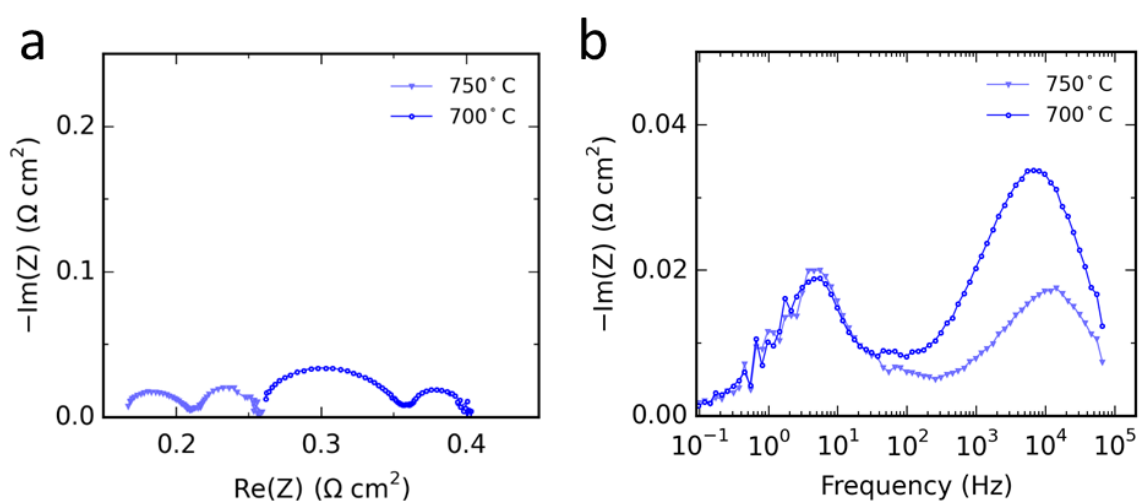


Figure 3.S3: (a) Nyquist plots and (b) Bode plots of impedance spectra measured on Cell B at 750°C and 700°C. The EIS response in the frequency range ($\sim 10^2$ – 10^5 Hz) increased pronouncedly with decreasing temperature while the response below $\sim 10^2$ Hz remained almost unaltered. The former can be ascribed to electrochemical processes in electrodes. The later can be ascribed to the gas diffusion and conversion processes, which are not thermally activated processes.

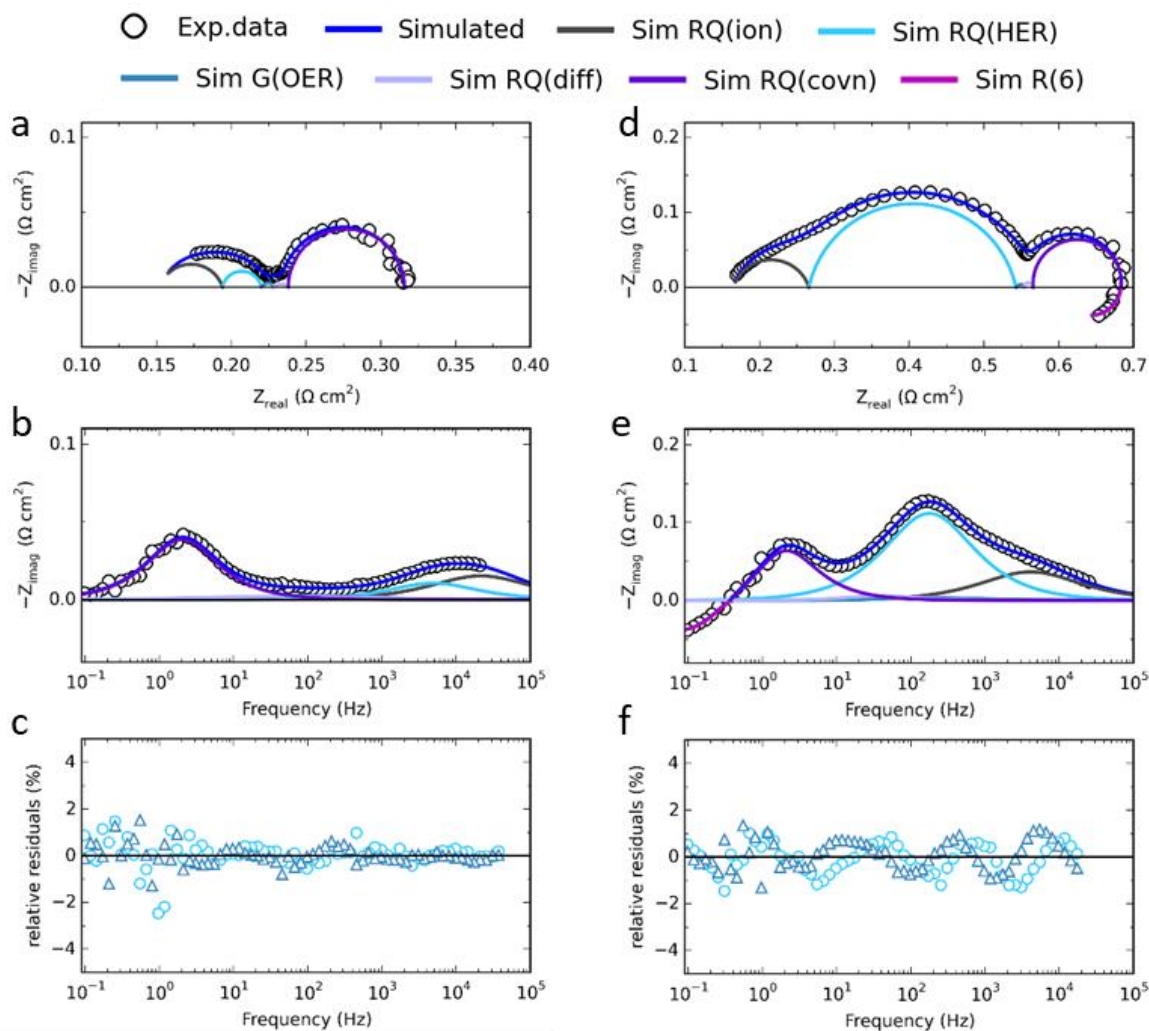


Figure 3.S4: CNLS fits of inductance corrected impedance spectra of Cell B at (a) 0 h and (d) 537 h of durability test under a constant current density of 1.00 A cm^{-2} at $750 \text{ }^\circ\text{C}$. The corresponding Bode plots (b, e) and relative residual plots (c, f).

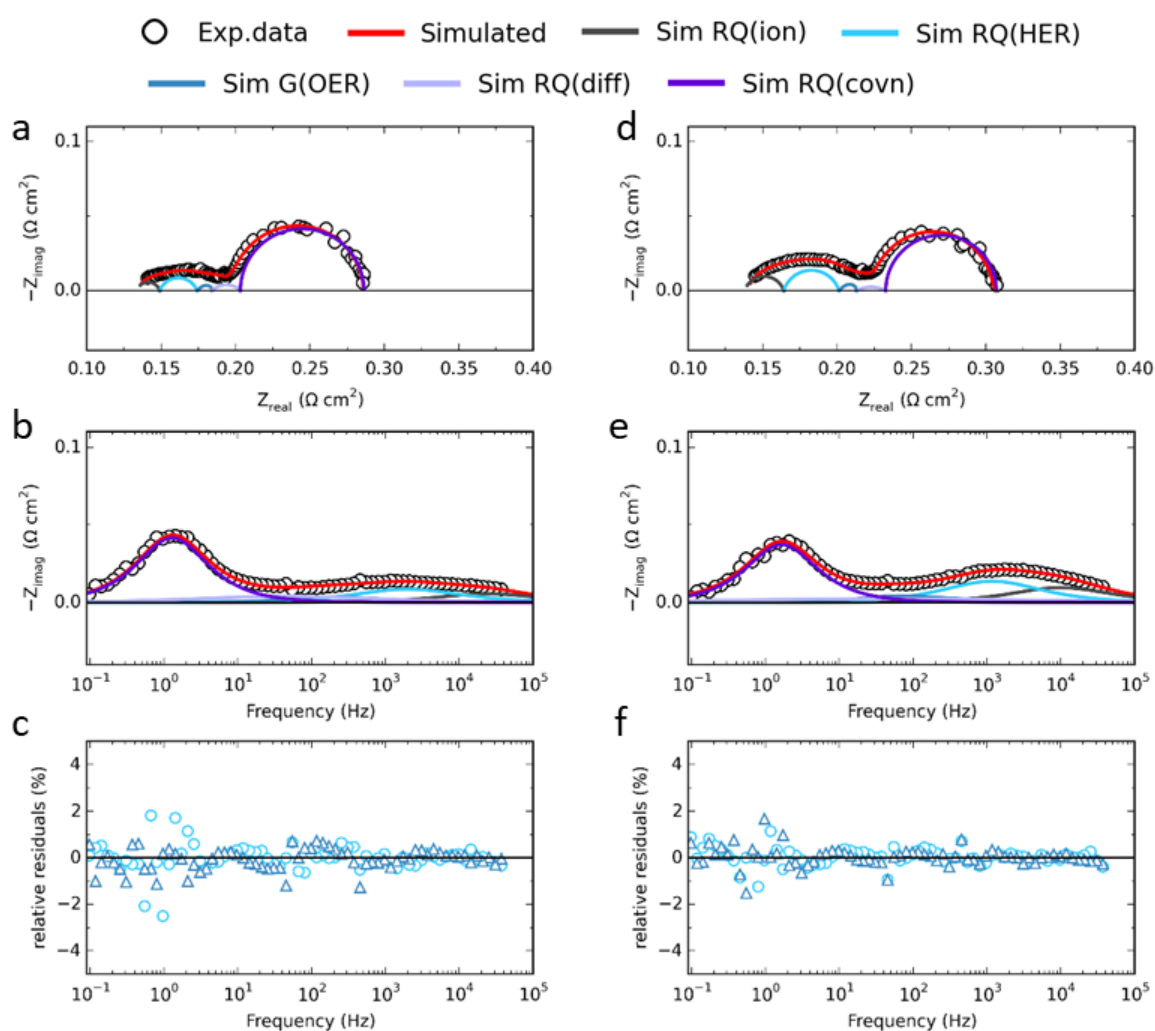


Figure 3.S5: CNLS fits of inductance corrected impedance spectra of Cell A at (a) 0 h and (d) 900 h of durability test under a constant current density of 1.00 A cm^{-2} at $750 \text{ }^\circ\text{C}$. The corresponding Bode plots (b, e) and relative residual plots (c, f).

Table 3.S1: Results from equivalent circuit modeling of impedance spectra shown in **Figure 3.7**.

Simulated resistance ($\Omega \text{ cm}^2$)	Cell B			Cell A		
	0 h	537 h	Increase	0 h	900 h	Increase
R_{ohm}	0.152	0.164	0.012	0.134	0.137	0.003
R_{ion}	0.042	0.101	0.059	0.013	0.026	0.013
R_{HER}	0.026	0.277	0.251	0.025	0.037	0.012
R_{OER}	0.008	0.011	0.003	0.010	0.012	0.002
R_{diff}	0.010	0.012	0.002	0.019	0.020	0.001
R_{conv}	0.079	0.107	0.028	0.081	0.078	-0.003
$R_{\text{P,Sim}}$	0.165	0.508	0.343	0.148	0.173	0.025

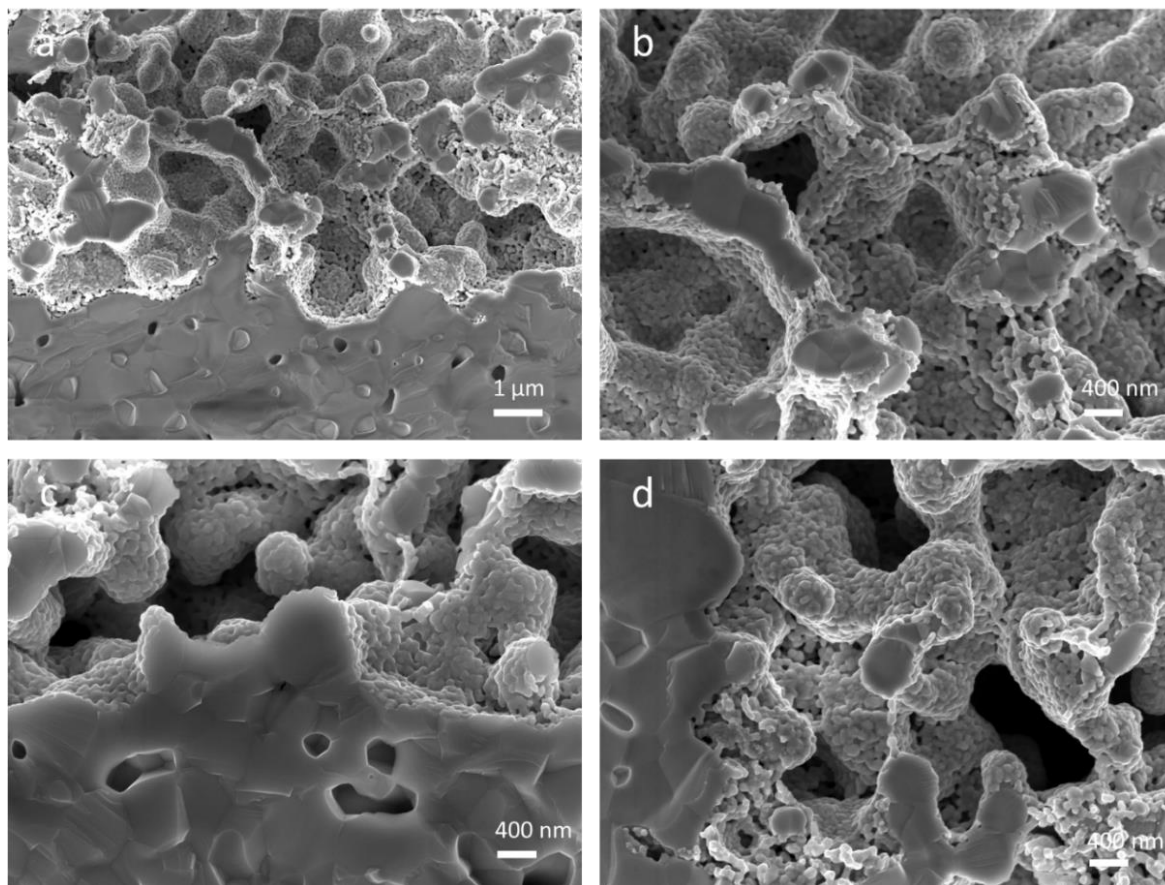


Figure 3.S6: Cross-sectional SEM images of LSC-CGPO-CGO oxygen electrodes for (a,b) initial, (c) Cell B after 537, and (d) Cell A after 900 h.

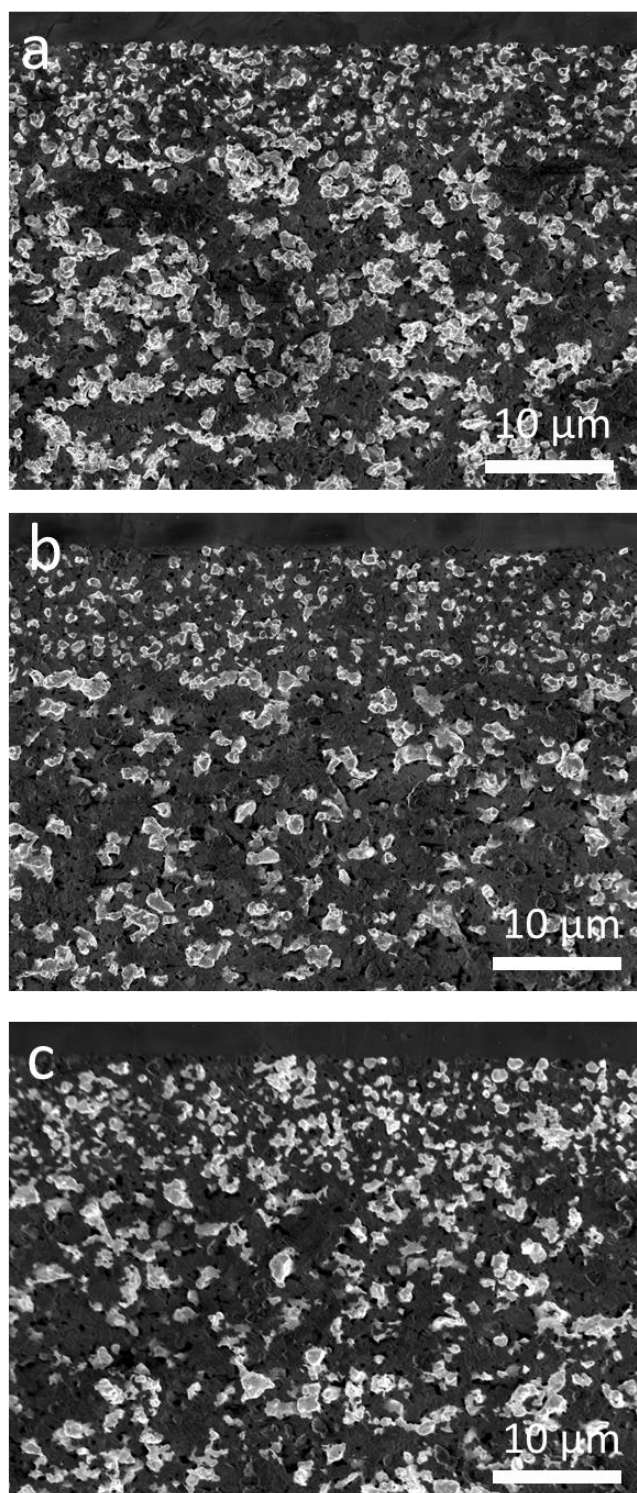


Figure 3.S7: SEM image showing Ni percolation in (a) the pre-reduced Ni/YSZ fuel electrode, (b) the Ni/YSZ fuel electrode of Cell B shown in **Figure 3.8a**, (c) the CGO-Ni/YSZ fuel electrode of Cell A shown in **Figure 3.8b**.

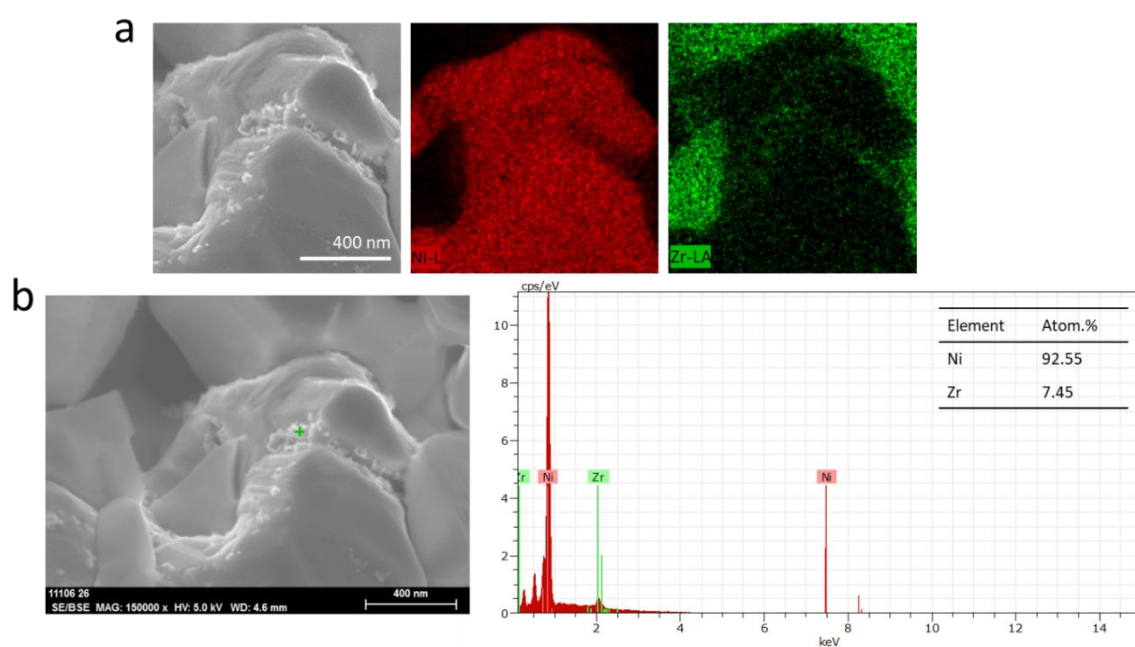


Figure 3.S8: Corresponding EDX of the Ni/YSZ fuel electrode from Cell B after the durability test. (a) elemental mappings, (b) point analysis on Ni grain.

CHAPTER 4

An up-scalable, infiltration-based approach for improving the durability of Ni/YSZ electrodes for solid oxide cells

A published article is included in this chapter (Paper [III](#). Tong, X., Hendriksen, P.V., Hauch, A. and Chen, M., ECS Transactions 91.1, 2019: 2433-2442)

Abstract

An important challenge for solid oxide electrolysis cells (SOECs) is the considerable degradation that the most commonly used fuel electrode, namely Ni/yttria-stabilized zirconia (YSZ), suffers during long-term operation, particularly at high current densities. In this work, we report on a method alleviating the problem based on infiltrating nano-sized electrocatalysts into the Ni/YSZ electrode of a full cell after it has been reduced in a “one-atmosphere-reduction” process. The performance and durability of infiltrated and non-infiltrated cells are evaluated at full test-cell size of 4 x 4 cm² level. The infiltrated cell exhibits significantly enhanced long-term durability at high current densities, with cell voltage degradation rates of 0.028 V kh⁻¹ (2.04 % kh⁻¹) at -1.25 A cm⁻² and 0.010 V kh⁻¹ (0.78 % kh⁻¹) at -1.00 A cm⁻² for steam electrolysis at 750 °C. These degradation rates are ~14 times and ~25 times smaller than those of the non-infiltrated cell, respectively. The infiltrated cell also shows superior durability to the non-infiltrated cell during reversible operation. These results demonstrate the great potential of boosting the durability of state-of-the-art Ni/YSZ fuel electrodes for electrolysis operation via this infiltration-based approach.

4.1 Introduction

The most commonly used fuel electrode in Solid oxide cells (SOCs) is based on Ni/yttria-stabilized zirconia (YSZ) composites, which displays excellent activity both for the hydrogen oxidation reaction (HOR) in fuel cell mode and the hydrogen evolution reaction (HER) in electrolysis mode. However, the Ni/YSZ electrode experiences considerable degradation in electrochemical performance during long-term electrolysis operation, particularly at strong polarization (high current densities). Several different microstructural deteriorations have been reported as contributing to the electrochemical performance degradation, including surface poisoning by impurities, Ni coarsening and migration, destruction of the Ni–YSZ interface, and even formation of ZrO₂ nanoparticles on the Ni surface due to the reduction/re-oxidation of YSZ. [41-52] Though mixed ionic-electronic conducting (MIEC) oxides, such as La_xSr_{1-x}Cr_{0.5}Mn_{0.5}O_{3-δ}, [53-55] La_{0.2}Sr_{0.8}TiO_{3+δ}, [56] La_{0.4}Sr_{0.4}Ni_{0.06}Ti_{0.94}O_{3-δ}, [57] La_{0.43}Ca_{0.37}Ni_{0.06}Ti_{0.94}O_{3-δ}, [58] and Sr₂Fe_{1.5}Mo_{0.5}O_{6-δ}, [59, 60] have been explored as alternative fuel electrodes, the catalytic activity and electrical conductivity of these MIEC electrodes have not reached the levels observed for the Ni/YSZ electrodes.

Recently, infiltration has been extensively applied for the fabrication and modification of SOC electrodes, resulting in excellent electrochemical performance. [61, 63, 150] More recently, our laboratory has found that modification of the Ni/YSZ electrode by coating the surface with nano-sized electrocatalysts via infiltration is an effective method to enhance the cell performance as well as the cell durability. [50, 127] For example, an infiltration modification has been carried out on a state-of-the-art SOC; Ni/YSZ support | Ni/YSZ fuel electrode | YSZ electrolyte | gadolinium-doped ceria (CGO) barrier layer | strontium and iron co-doped lanthanum cobaltite (LSCF)/CGO oxygen electrode, which reduced the degradation rate during steam electrolysis at 800 °C from 0.699 V kh⁻¹ to 0.114 V kh⁻¹ at -1.25 A cm⁻². [50] To enable a sufficient porosity in the Ni/YSZ structure for infiltration and to avoid the chemical expansion of the CGO barrier layer and decomposition of the LSCF during reduction, the cell was pre-reduced in a “two-atmosphere-reduction”, i.e., the NiO/YSZ fuel electrode was exposed to reducing atmosphere while the LSCF/CGO oxygen electrode was exposed to air (**Figure 4.1**). This was achieved using an in-house built test rig which is well suited for the purpose if only a small number of cells is considered, but not

well suited for mass production. A viable route for realizing the infiltration is performing the treatment as a “two-atmosphere-reduction” on stack level after the Ni/YSZ electrode has been reduced during stack-initiation as was done in ref [151]. In this work, we simplify the aforementioned infiltration method to allow it to be done before stack assembly, but yet in a way that can be upscaled to mass production. Instead of doing the treatment in two-atmosphere requiring temporary sealings, the full cell was subjected to reducing conditions. Treatment as a “one-atmosphere-reduction” that can well be carried out during the cooling of the cell after the final sintering step (**Figure 4.1**).

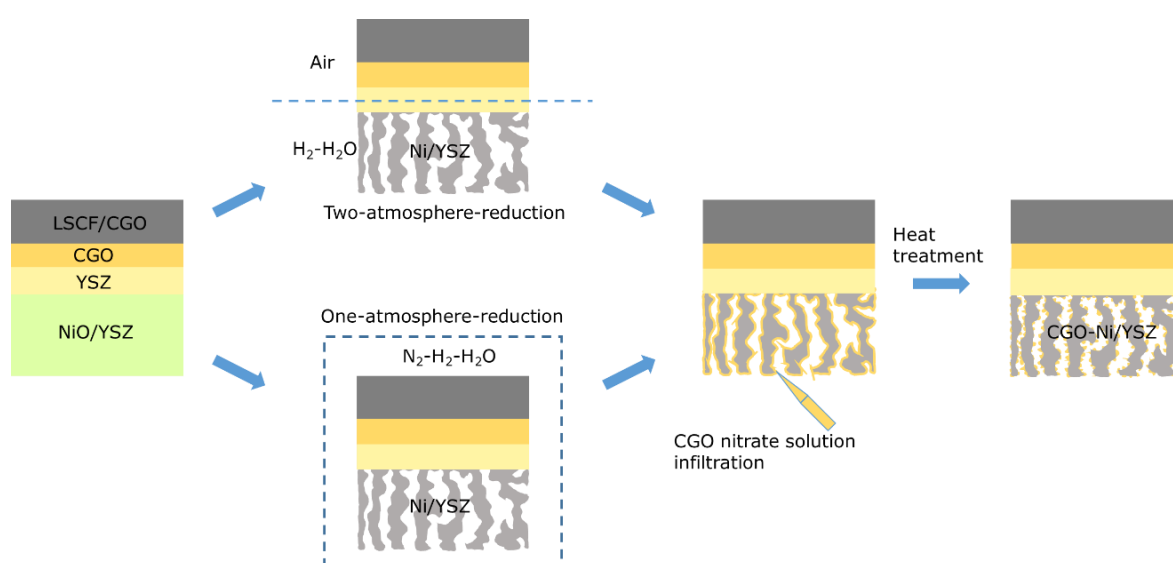


Figure 4.1: Schematic illustration of different cell preparation routes enabling the reduction of NiO to Ni prior to modifying the Ni/YSZ electrode with CGO electrocatalysts.

4.2 Experimental

4.2.1 Manufacturing of SOCs

The fuel-electrode-supported cells used in this work are in size of $5.3 \times 5.3 \text{ cm}^2$ and consist of a Ni/YSZ support, a Ni/YSZ fuel electrode, a dense YSZ electrolyte, a CGO barrier layer, and an LSCF/CGO (LSCF: $\text{La}_{0.6}\text{Sr}_{0.4}\text{Co}_{0.2}\text{Fe}_{0.8}\text{O}_{3-\delta}$) composite oxygen electrode. A detailed description of the fuel electrode-supported cell fabrication can be found elsewhere. [152] A $4 \times 4 \text{ cm}^2$ strontium-doped lanthanum manganite (LSM) current-collector layer was applied on top of the LSCF/CGO electrode by screen-printing.

4.2.2 Infiltration of SOCs

The infiltrated cells with CGO modified Ni/YSZ fuel electrodes were prepared after the full cell was reduced. For the applied “one-atmosphere-reduction”, conditions including temperature and gas feeds need to be carefully chosen and controlled. In this work, the treatment was carried out at $750 \text{ }^\circ\text{C}$ in $3.9\%\text{H}_2\text{-}93.2\%\text{N}_2\text{-}2.9\%\text{H}_2\text{O}$ gas mixture for 10 h. Afterwards, the reduced Ni/YSZ electrode was infiltrated with a nitrate solution containing stoichiometric amounts of $\text{Ce}(\text{NO}_3)_3$ and $\text{Gd}(\text{NO}_3)_3$ (4:1 molar ratio of Ce^{3+} : Gd^{3+}), followed by calcination at $300 \text{ }^\circ\text{C}$ in air for 15 min. Note that surfactant PE-L62 (Sigma-Aldrich Corporation) with 1.4 wt.% per weight of solution was added to improve wetting/penetration of the structure.[50] The infiltration and calcination processes were repeated 9 times to get a loading of $\sim 145 \text{ mg}$ CGO per 1 cm^3 Ni-YSZ backbone (Ni/YSZ electrode + Ni/YSZ support).

4.2.3 SEM and XRD analysis

The cell structures were examined using scanning electron microscopy (SEM) in a Zeiss Merlin microscope. The crystal structure of fuel electrodes was characterized by X-ray diffraction (XRD) on Bruker D8 Rigaku diffractometer using $\text{Cu K}\alpha$ radiation as the source. The scanning range is $20\text{--}80^\circ$.

4.2.4 Electrochemical characterization

Electrochemical tests were conducted on the infiltrated and non-infiltrated cells using in-house constructed test rigs, as described in previous work.[114, 140] The active area of the cells is $4 \times 4 \text{ cm}^2$, the edges were used for sealing. At start-up, the cells were heated ($1 \text{ }^\circ\text{C min}^{-1}$) to $750 \text{ }^\circ\text{C}$ with $5\% \text{H}_2$ - $95\% \text{Ar}$ fed to the fuel electrodes and air to the oxygen electrodes with a dwelling time of 2 h, followed by another 2 h with $96\% \text{H}_2$ - $4\% \text{H}_2\text{O}$ to the fuel electrodes. To evaluate the performance of the infiltrated and non-infiltrated cells, electrochemical impedance spectroscopy (EIS) measurements were performed at different temperatures, gas compositions and current loads. A Solartron 1255 frequency response analyzer in combination with a measurement resistor was used for recording the EIS, at frequencies from 0.0968 to 96850 Hz with a perturbation amplitude of 3.75 mA cm^{-2} . The durability of cells was evaluated at $750 \text{ }^\circ\text{C}$ both for steam electrolysis and reversible fuel cell/electrolysis cell operation.

4.3 Results and discussion

4.3.1 Microstructure of the cells

Figures 4.2a and **2b,c** show photographs and cross-sectional SEM images of the cell after being treated in the H_2 - N_2 - H_2O gas mixture for 10 h at $750 \text{ }^\circ\text{C}$. The color of the fuel electrode has changed from green to gray, indicating the reduction of NiO to Ni. This reduction provides the interconnected pores needed for infiltration. Meanwhile, no obvious delamination, cracks, or other damages are observed in the LSCF/CGO oxygen electrode, the CGO barrier layer or the YSZ electrolyte. **Figure 4.2d** shows the microstructure of the pre-reduced Ni/YSZ fuel electrode, in which a porous structure composed of clear grains is observed. **Figures 4.2e,f** show that after infiltration the nanostructured CGO coatings are well deposited on the inner surfaces of the Ni/YSZ electrode. The reduction of NiO to Ni and deposition of CGO coatings are further confirmed by the XRD patterns shown in **Figure 4.3**.

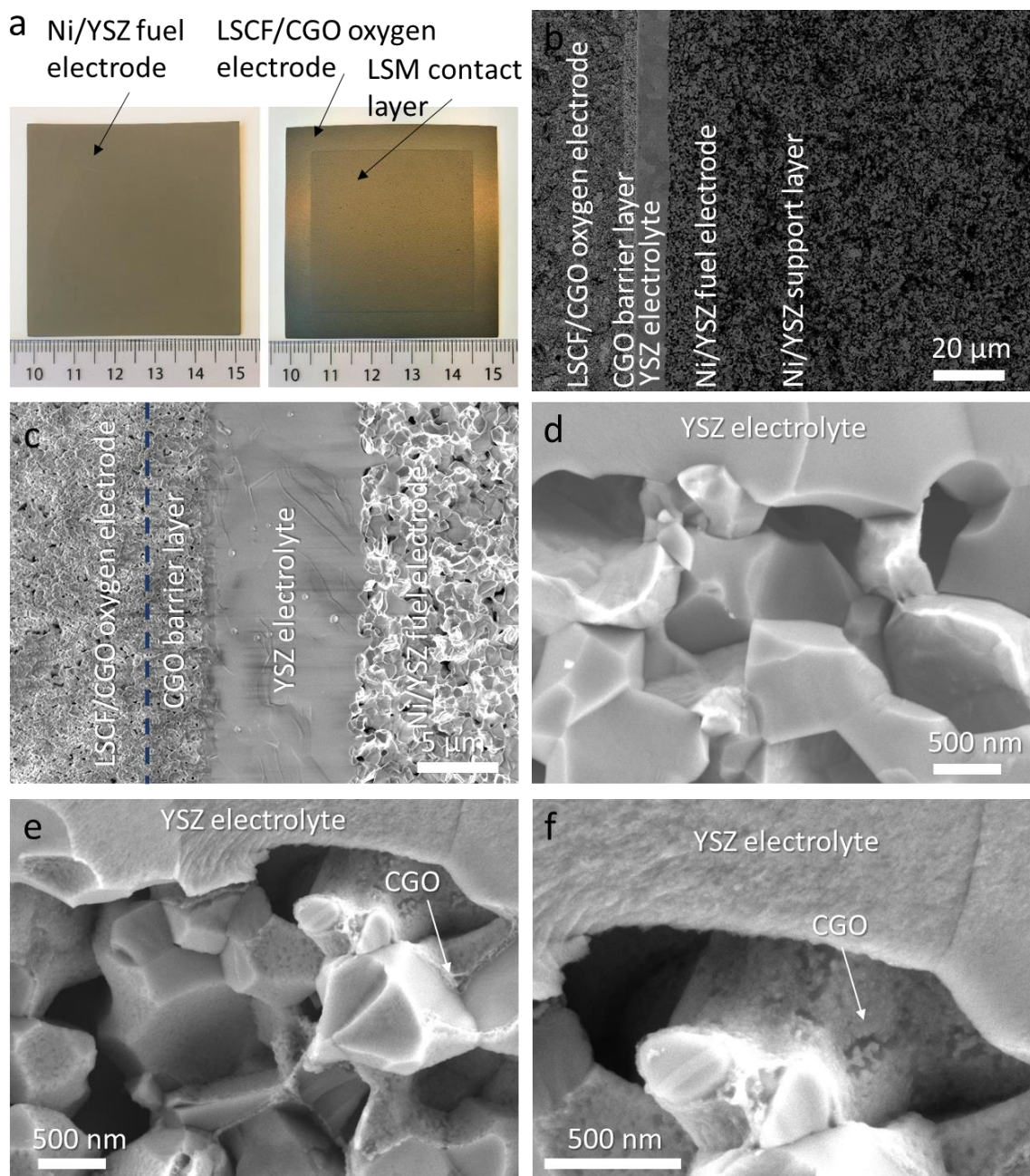


Figure 4.2: (a) Photographs and (b,c) cross-sectional SEM images of fuel-electrode-supported cell after “one-atmosphere-reduction”. Cross-sectional SEM images of (d) Ni/YSZ fuel electrode and (e,f) Ni/YSZ fuel electrode infiltrated with CGO electrocatalysts.

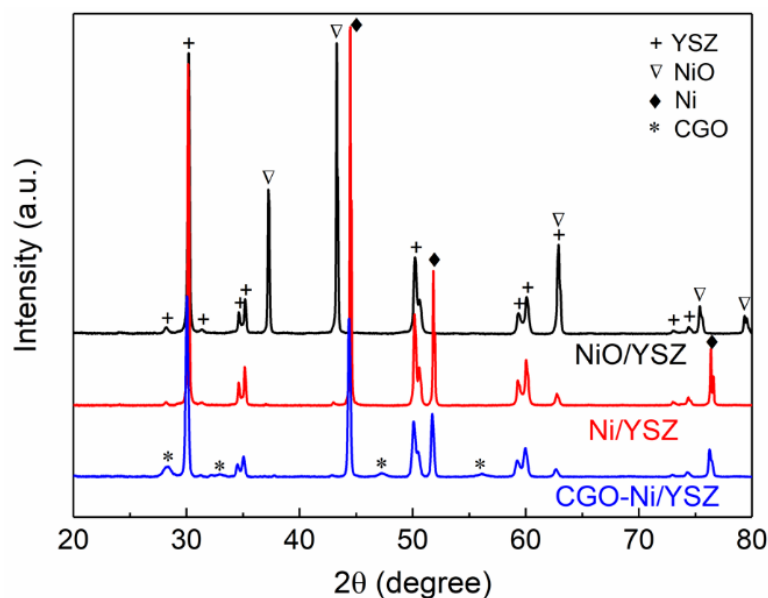


Figure 4.3: XRD patterns of NiO/YSZ electrode (black), Ni/YSZ electrode reduced in N_2 - H_2 - H_2O at 750 °C for 10 h (red), and Ni/YSZ electrode infiltrated with CGO electrocatalysts (blue).

4.3.2 Performance at open circuit voltage (OCV) conditions

To evaluate the effect of “one-atmosphere-reduction” and CGO infiltration on cell performance, EIS measurements were performed on the infiltrated cell and the “as-prepared” non-infiltrated sister-cell at 700 °C under OCV condition with different gas feeds. The intercept with the real axis at high frequency in the Nyquist plots (**Figures 4.4a,b**) represents the ohmic resistance (R_{ohm}), and the difference between the high and low frequency intercepts represents the total polarization resistance (R_p). The determined values of R_{ohm} and R_p are summarized in **Table 4.1**. To clearly compare the performance of the two cells, the EIS data recorded with 4% H_2O -96% H_2 fed to the fuel electrode and dry air to the oxygen electrode in **Figures 4.4a** and **4b** have been replotted in **Figure 4.4c**. The non-infiltrated and infiltrated cells show a similar and expected trend for R_{ohm} and R_p with the change of the gas feeds. R_{ohm} is almost unaltered. R_p decreases pronouncedly with increasing steam partial pressure from 4% H_2O to 50% H_2O at the fuel electrode, and they further decrease when the gas in the oxygen electrode compartment is changed from air to pure O_2 .

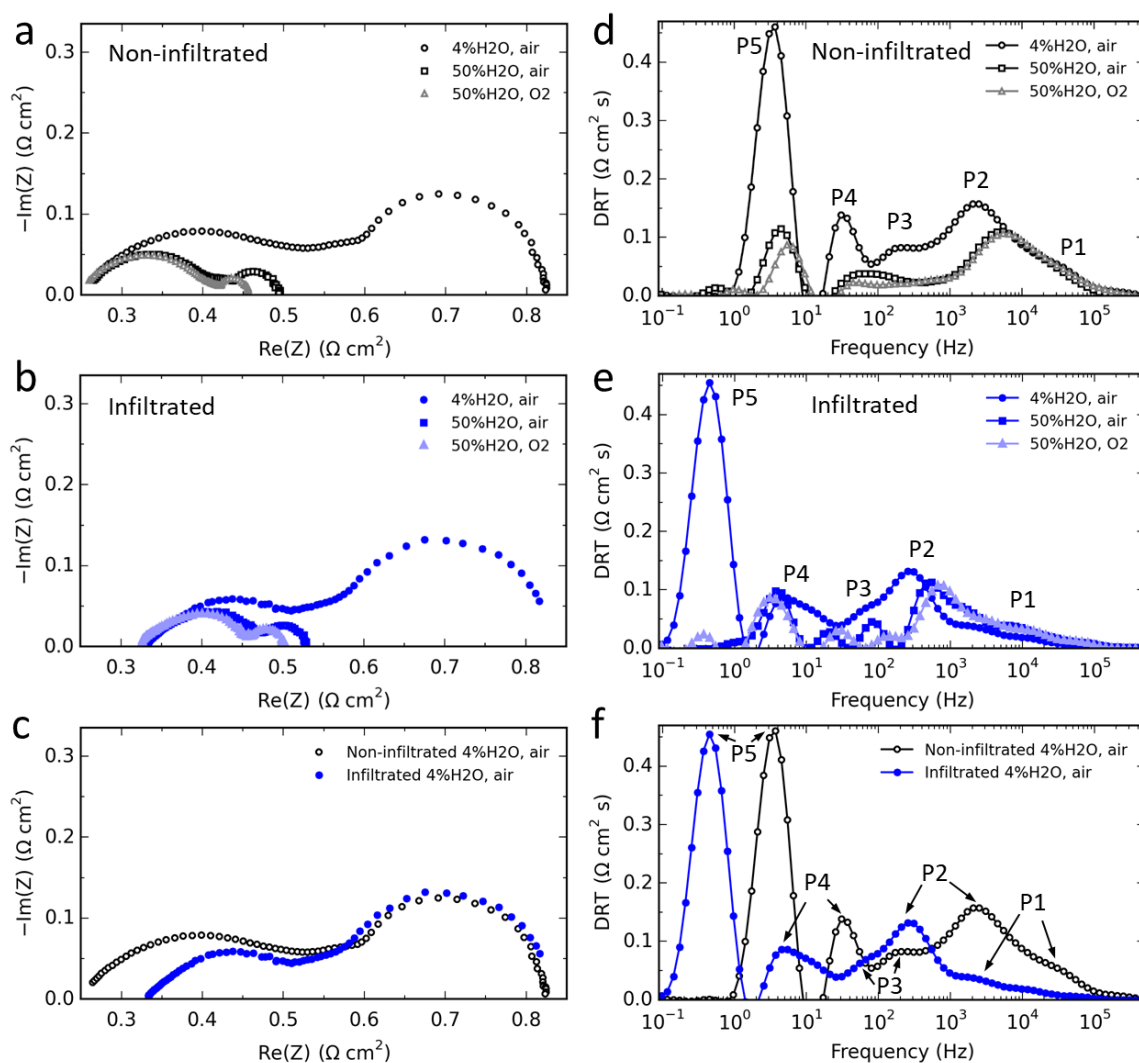


Figure 4.4: EIS data recorded at 700 °C and open circuit voltage with varying gas feeds to the electrodes. Nyquist plots and DRT plots (a, d) of the non-infiltrated cell, and (b, e) infiltrated cell. Comparison of the (c) Nyquist and (d) DRT plots of the non-infiltrated cell and the infiltrated cell.

The R_{ohm} values are determined to be 0.260–0.265 $\Omega \text{ cm}^2$ and 0.326–0.333 $\Omega \text{ cm}^2$ for the non-infiltrated and the infiltrated cell, respectively. For both cells, the R_{ohm} is much greater than the expected value of $\sim 0.06 \Omega \text{ cm}^2$, which is calculated from the thickness of the YSZ and CGO (8 μm YSZ and 5 μm thick CGO barrier) of the here investigated cells and the ionic conductivities of the two materials; 0.02 S cm^{-1} for YSZ and 0.03 S cm^{-1} for CGO at 700 °C. [117] This might in principle originate from poor contact in the cell-testing-setup or

between the oxygen electrode and the LSM current-collector layer, but is more likely an effect of an elemental interdiffusion between CGO and YSZ which is known to reduce conductivity in both these fluorites. [118-120] R_{ohm} of the infiltrated cell is higher than for the non-infiltrate one. Different batches of LSM inks were used for these two cells, this could be a reason for the discrepancy of R_{ohm} between two cells. This discrepancy could also be due to the treatment of “one-atmosphere-reduction” on the infiltrated cell. To make this clear, further work is needed. The R_p values are 0.560 and 0.483 $\Omega\text{ cm}^2$ in 4% H_2O -96% H_2 , air, 0.230 and 0.196 $\Omega\text{ cm}^2$ in 50% H_2O -50% H_2 , air, and 0.197 and 0.176 $\Omega\text{ cm}^2$ in 50% H_2O -50% H_2 , O_2 for the non-infiltrated and the infiltrated cell, respectively. Hence, R_p of the infiltrated cell is smaller than for the non-infiltrated one under all gas conditions.

Table 4.1: R_{ohm} and R_p of the non-infiltrated and infiltrated cells under different gas conditions at 700 °C. The resistances were determined from Nyquist plots in **Figure 4.4**, and the units for these values are $\Omega\text{ cm}^2$.

Gas conditions	Non-infiltrated		Infiltrated	
	R_{ohm}	R_p	R_{ohm}	R_p
4% H_2O -96% H_2 , air	0.262	0.560	0.331	0.483
50% H_2O -50% H_2 , air	0.265	0.230	0.333	0.196
50% H_2O -50% H_2 , O_2	0.260	0.197	0.326	0.176

In order to distinguish the different contributions to the overall R_p , the EIS data were analyzed by the distribution of relaxation time (DRT). [142, 153] The results are shown in **Figures 4.4d-f**. For both cells, five peaks (P_1 , P_2 , P_3 , P_4 , and P_5) in the frequency range of 0.1–100 kHz are identified. Each peak corresponds to an electrode process. The area enclosed by a specific peak represents the magnitude of resistance for that specific electrode process. [143] As shown in **Figures 4.4d,e**, P_1 is almost independent of the gas conditions. Whereas, increasing the steam partial pressure at the fuel electrode results in a significant decrease in the peak area of P_2 , P_4 , and P_5 . Moreover, the peak position shifts to a higher frequency. The change of gas in the oxygen electrode from air to O_2 leads to a change in P_3 , P_4 , and P_5 , while P_2 remains almost unaltered. On the basis of these results and previously reported analyses: [43, 44, 84, 140] P_1 is likely related to the transport of oxygen anions

through the ionic conducting networks in the electrodes. The major contribution of P_1 is then expected from the fuel electrode which has a thicker and poorer conducting electrolyte network than does the oxygen electrode; P_2 is associated with the steam splitting/hydrogen oxidation process at the triple phase boundaries (TPBs) of the fuel electrode; P_3 is associated with the oxygen incorporation/evolution process at the active sites of the oxygen electrode; P_4 and P_5 represent the gas diffusion and the gas conversion, respectively. **Figure 4.4f** compares the DRT plots of the two cells, showing a marked reduction in the area of P_2 ascribable to the CGO fuel electrode infiltration. The smaller area of P_3 for the redox cycled infiltrated cell indicates that the reduction and reoxidation at the start of testing do not harm the LSCF/CGO oxygen electrode, but it actually improves slightly. The areas of P_4 and P_5 are comparable for the two cells.

4.3.3 Performance under current

Figure 4.5 compares the EIS data on non-infiltrated and infiltrated cells recorded under varying current densities from 0 (OCV) to -1.25 A cm^{-2} with a step size of -0.125 A cm^{-2} . The gas conversion is proportional to the applied current density assuming a Faraday efficiency of 100%. R_{ohm} follows a similar trend for the two cells; it decreases slightly with increasing current density (**Figures 4.5a** and **5b**), attributed to a continuous increase in cell temperature due to producing more joule heat at higher current density. For both cells the R_p values first increase and then decrease with increasing current density, but the difference between the two cells is getting larger. At -1.25 A cm^{-2} , the R_p of the non-infiltrated cell reaches $0.294 \text{ } \Omega \text{ cm}^2$, $\sim 41 \%$ larger than that of the infiltrated cell ($0.209 \text{ } \Omega \text{ cm}^2$).

The DRT results in **Figures 5c** and **5d** show that this increased difference in R_p is mainly due to the different behaviors of the two cells on P_1 (the transport of oxygen anions through the ionic conducting networks in the electrodes) and P_2 (the steam splitting process at the TPBs in the Ni/YSZ fuel electrode). For the non-infiltrated cell, increasing the current density results in a continuous and considerable increase in P_1 and P_2 . Whereas the infiltrated cell shows a much smaller increase in P_2 , and even a slight decrease in P_1 .

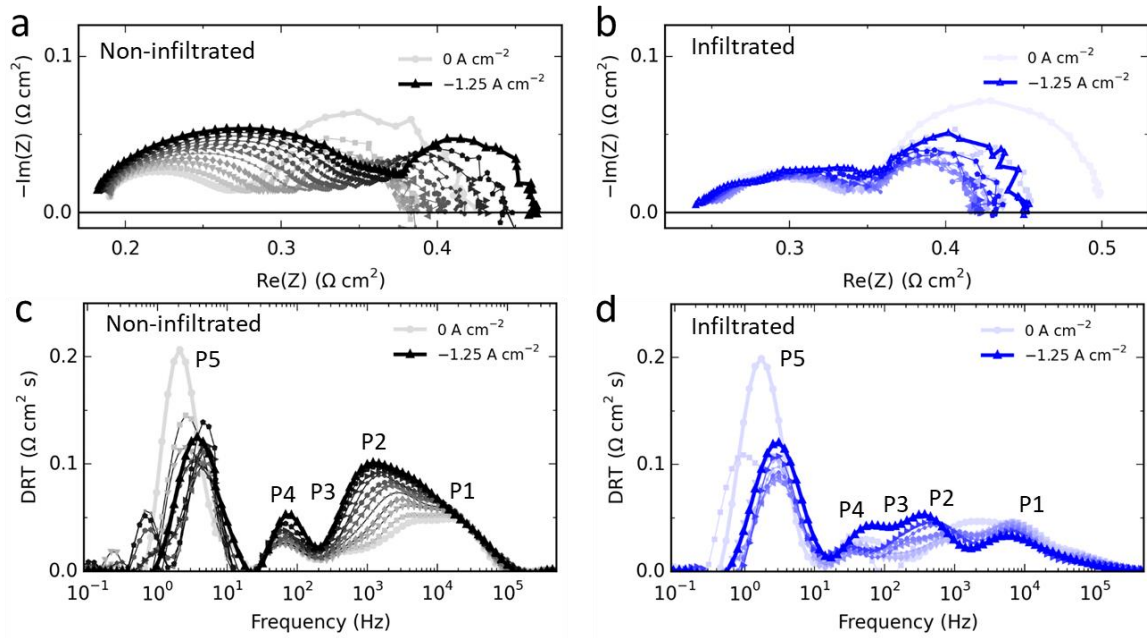


Figure 4.5: Nyquist plots and DRT plots of the EIS data recorded on (a,c) non-infiltrated cell and (d,e) infiltrated cell under varying applied current densities at 750 °C with 22.2 l h⁻¹ of 90% H₂O-10% H₂ fed to the fuel electrode and 50 l h⁻¹ pure O₂ to the oxygen electrode.

These EIS data were further fitted with the equivalent circuit model shown in **Figure 4.6a** by the complex-non-linear-least-squares (CNLS) method.[46, 50] Four constant phase elements (RQ) and a modified Gerischer element (G) in the model correspond to the five different processes seen in the DRT. **Figure 4.6b** shows the fitted spectra of EIS data measured at -1.25 A cm^{-2} . **Figure 4.6c** compares the evolution of the fitted resistances for each process of two cells with increasing current density. The two cells show significantly different behaviors on R_1 (the resistance for the transport of oxygen anions, corresponding to P₁) and R_2 (the dominant resistance term in the steam splitting process at the TPBs in the Ni/YSZ fuel electrode, corresponding to P₂). Notably, the R_2 of the non-infiltrated cell increases by a factor of ~ 2 when the current density is increased from 0 to -1.25 A cm^{-2} , while the R_2 of the infiltrated cell only increases by 25%. At -1.25 A cm^{-2} , the R_2 of $0.040 \text{ } \Omega \text{ cm}^2$ for the infiltrated cell is $\sim 35\%$ that of the non-infiltrated cell ($0.114 \text{ } \Omega \text{ cm}^2$). These results suggest that the electro-catalytic activity is greatly improved on the CGO modified Ni/YSZ electrode, particularly at high current densities.

Furthermore, the R_3 (the dominant resistance for the oxygen evolution reaction at the active sites in the LSCF/CGO oxygen electrode, corresponding to P_3) of the infiltrated cell seems lower than those of the as-prepared cell, but the difference is very small and it is within the uncertainty of the fitting. Future work based on symmetrical cells will be performed to study the effect of reduction and oxidation treatments on the performance of the LSCF/CGO oxygen electrode. The two cells show a similar behavior on the total concentration resistance (i.e., the sum of R_4 (gas diffusion, corresponding to P_4) and R_5 (gas conversion, corresponding to P_5)), which first decreased with increasing current density from 0 to -0.75 A cm^{-2} (corresponding to a decrease in steam content of gas mixture from 90% to 67%) and then increased. Base on the plug-flow model described in ref. [154], starting from a 90% H_2O -10% H_2 mixture the concentration resistance will decrease with increasing current density as the composition approaches the 50% H_2O -50% H_2 mixture where the concentration resistance is minimal whereafter it increases again. The change of concentration resistance with current density in **Figure 4.6c** is faster than theoretically calculated, and similar behavior has also been observed by Mogensen et al. [154]

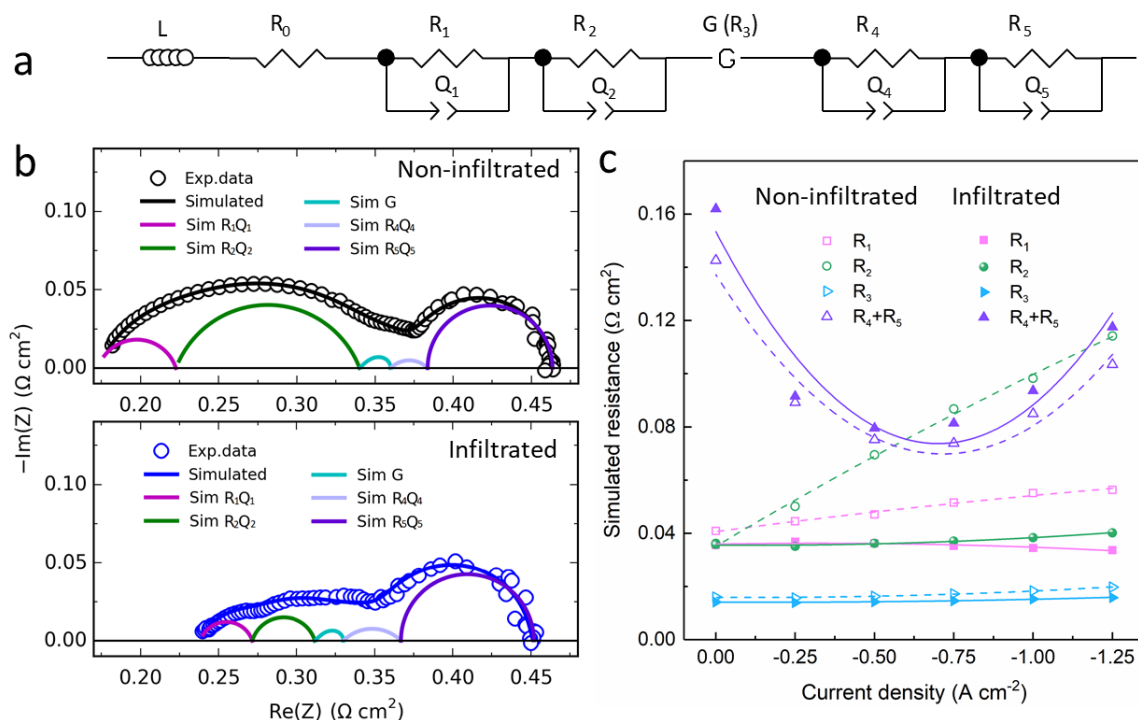


Figure 4.6: (a) Electrical equivalent circuit model for CNLS fits. (b) CNLS fits of EIS data recorded under -1.25 A cm^{-2} for the non-infiltrated and the infiltrated cells. (c) Resistances from the fitting results.

4.3.4 Durability for steam electrolysis and reversible operation

Figure 4.7 compares the durability of non-infiltrated and infiltrated cells for steam electrolysis, tested at 750 °C with current density maintained first at -1.25 and then -1.00 A cm^{-2} . Assuming a Faraday efficiency of 100%, the H_2 production rates for the two cells reach 8.70 and 6.96 $\text{ml min}^{-1} \text{cm}^{-2}$ at -1.25 and -1.00 A cm^{-2} , respectively, corresponding to steam utilization of 42 and 33 %. **Figure 4.7a** shows the evolution of cell voltage with time. When operated at -1.25 A cm^{-2} , the initial voltage of the non-infiltrated cell is 1.385 V, and it decreases to 1.377 V over the first 15 h, then increases rapidly to 1.503 V in the following 285 h, corresponding to a degradation rate of 0.442 V kh^{-1} (32.1 % kh^{-1}). In contrast, the initial voltage of the infiltrated cell is 1.408 V, and it decreases continuously to 1.350 V over the first 300 h, then increases to 1.372 V over the following 800 h, corresponding to a degradation rate of 0.028 V kh^{-1} (2.0 % kh^{-1}), ~ 14 times smaller than the degradation rate for the non-infiltrated cell when assessed over these selected periods.

Subsequently, the durability of the cells was tested at -1.00 A cm^{-2} . For the non-infiltrated cell, the voltage increases from 1.385 V to 1.464 V in 300 h (from 315 to 615 h), corresponding to a degradation rate of 0.263 V kh^{-1} (19.0 % kh^{-1}). Whereas the infiltrated cell has a much lower voltage of 1.280 V initially, and the voltage increases only 0.003 V over the next 300 h (from 1130 to 1430 h), corresponding to a degradation rate of 0.010 V kh^{-1} (0.8 % kh^{-1}), a factor of 25 smaller than that of the non-infiltrated cell. This cell can effectively be operated with very small degradation (0.8 % kh^{-1}) at thermo-neutral voltage yielding a current density of -1.00 A cm^{-2} at 750 °C. Clearly, the durability of the infiltrated cell is far superior to the non-infiltrated cell, demonstrating the feasibility of enhancing cell durability via the applied approach; where the full cell is placed in reducing environment and after the treatment the Ni/YSZ electrode is infiltrated. The reduction step could conveniently be carried out as the last step in the cell manufacturing process; during cooling after firing the oxygen electrode, the atmosphere is changed to the specified mixture of H_2 - N_2 - H_2O .

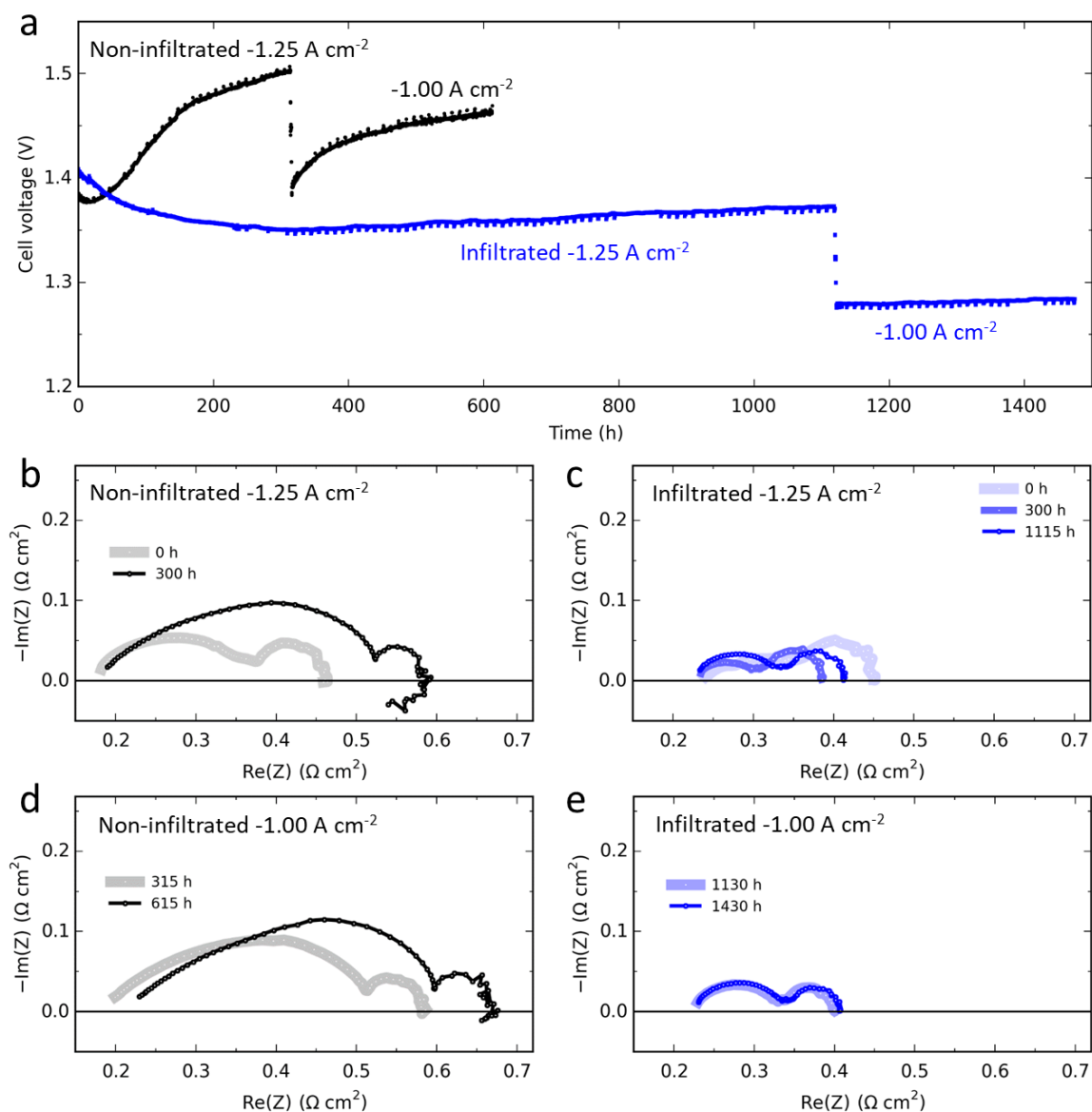


Figure 4.7: Comparison of the cell durability during steam electrolysis at 750 °C with 22.2 l h⁻¹ of 90%H₂O-10%H₂ to the fuel electrode and 50 l h⁻¹ pure O₂ to the oxygen electrode. (a) Evolution of cell voltage as a function of time. Nyquist plots of EIS data recorded under current during the durability test period. (b) -1.25 A cm⁻² on the non-infiltrated cell, (c) -1.25 A cm⁻² on the infiltrated cell, (d) -1.00 A cm⁻² on the non-infiltrated cell, and (e) -1.00 A cm⁻² on the infiltrated cell.

Figures 4.7b-e show the Nyquist plots of the EIS data recorded under current during the durability tests. After 300 h at -1.25 A cm⁻², R_{ohm} and R_p of the non-infiltrated cell increase 0.007 Ω cm² and 0.079 Ω cm², respectively (**Figure 4.7b**). The increase in R_p contributes

~92% of the total resistance increase, showing that the cell degradation processes occur mainly on the electrodes. The significant increase in P_2 in the corresponding DRT plots for the non-infiltrated cell reveals that the major degradation is from the Ni/YSZ fuel electrode (**Figure 4.8a**). Supporting this is also the observation of an additional “negative loop” appearing in the low-frequency range in the Nyquist plot after 300 h operation (**Figure 4.7b**), which has been shown to originate from the reduction of YSZ in the Ni/YSZ electrode.[42, 144]

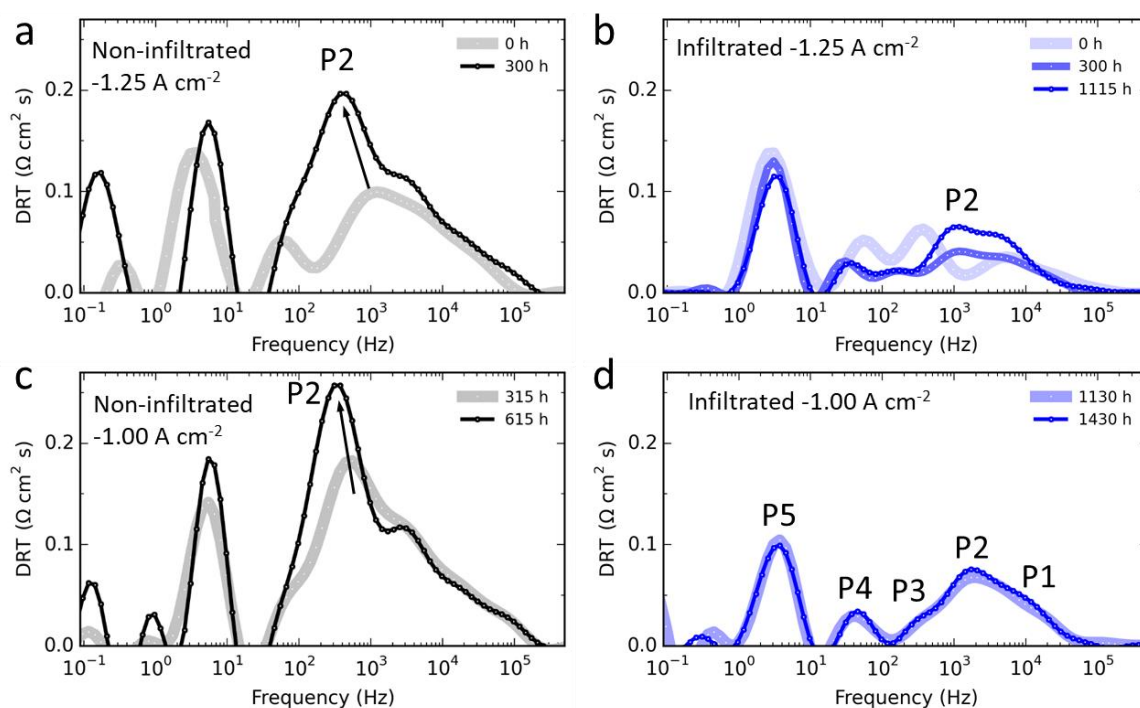


Figure 4.8: DRT plots of EIS data recorded under current during the durability test period. (a) -1.25 A cm^{-2} on the non-infiltrated cell, (b) -1.25 A cm^{-2} on the infiltrated cell, (c) -1.00 A cm^{-2} on the non-infiltrated cell, and (d) -1.00 A cm^{-2} on the infiltrated cell.

For the infiltrated cell, both R_{ohm} and R_p decreased in the first 300 h (**Figure 4.7c**). Furthermore, a decrease in P_2 is observed in the corresponding DRT plots (**Figure 4.8b**), which is attributed to an activation of the CGO modified Ni/YSZ fuel electrode. In the next 800 h, R_{ohm} is almost stable and the R_p only increases $0.027 \text{ } \Omega \text{ cm}^2$. The corresponding increase in P_2 (**Figure 4.8b**) is much smaller than that for the non-infiltrated cell (**Figure 4.8a**). For the subsequent 300 h operation at -1.00 A cm^{-2} , the increase of R_{ohm} and R_p on the non-infiltrated cell are $0.030 \text{ } \Omega \text{ cm}^2$ and $0.044 \text{ } \Omega \text{ cm}^2$, respectively (**Figure 4.7d**).

Whereas, the increase of R_{ohm} and R_p on the infiltrated cell are only $0.001 \Omega \text{ cm}^2$ and $0.005 \Omega \text{ cm}^2$, respectively (**Figure 4.7e**). Similar to the observation at -1.25 A cm^{-2} , the increase in P_2 is also significantly reduced for the infiltrated cell when operated at -1.00 A cm^{-2} (**Figures 4.8c** and **8d**). These EIS results are consistent with the cell voltage evolution results plotted in **Figure 4.7a**, and they demonstrate that the CGO modification improves significantly the durability of Ni/YSZ fuel electrode when operated at or above -1 A cm^{-2} .

After steam electrolysis, the infiltrated cell was further investigated for reversible operation under a current density of first ± 0.50 and then $\pm 1.00 \text{ A cm}^{-2}$ at $750 \text{ }^\circ\text{C}$ (**Figure 4.9a**). Under each current, the cell was operated for 120 h in fuel cell mode and 120 h in electrolysis mode before shifted to cyclic operation with time periods of 3 h in fuel cell mode and 20 h in electrolysis mode. The H_2 and steam utilization were adjusted to be 52 % during reversible operation. When operated at $\pm 0.50 \text{ A cm}^{-2}$, no obvious signs of degradation could be observed on the infiltrated cell. For comparison, a new “as prepared” non-infiltrated cell was tested under the same cycling conditions. The new non-infiltrated cell was used because the previous one has degraded a lot after the steam electrolysis test and its performance is too poor for further investigation. **Figure 4.9b** illustrates the behavior; 0.016 V increase in cell voltage after 120 h at -0.50 A cm^{-2} , corresponding to a degradation rate of $\sim 0.133 \text{ V kh}^{-1}$; 0.148 V increase in cell voltage after 26 cycles at $\pm 0.50 \text{ A cm}^{-2}$, corresponding to a degradation rate of $\sim 0.006 \text{ V per cycle}$).

For reversible operation under $\pm 1.00 \text{ A cm}^{-2}$, the infiltrated cell shows 0.009 V increase in cell voltage after 120 h at -1.00 A cm^{-2} , corresponding to a degradation rate of $\sim 0.075 \text{ V kh}^{-1}$; 0.029 V increase in cell voltage after 11 cycles at $\pm 1.00 \text{ A cm}^{-2}$, corresponding to a degradation rate of $\sim 0.003 \text{ V per cycle}$. These degradation rates measured at $\pm 1.00 \text{ A cm}^{-2}$ are $\sim 50\%$ less than those of the non-infiltrated cell at lower current of $\pm 0.50 \text{ A cm}^{-2}$. Accordingly, the infiltrated cell showed significantly improved durability compared with the non-infiltrated cell during reversible operation.

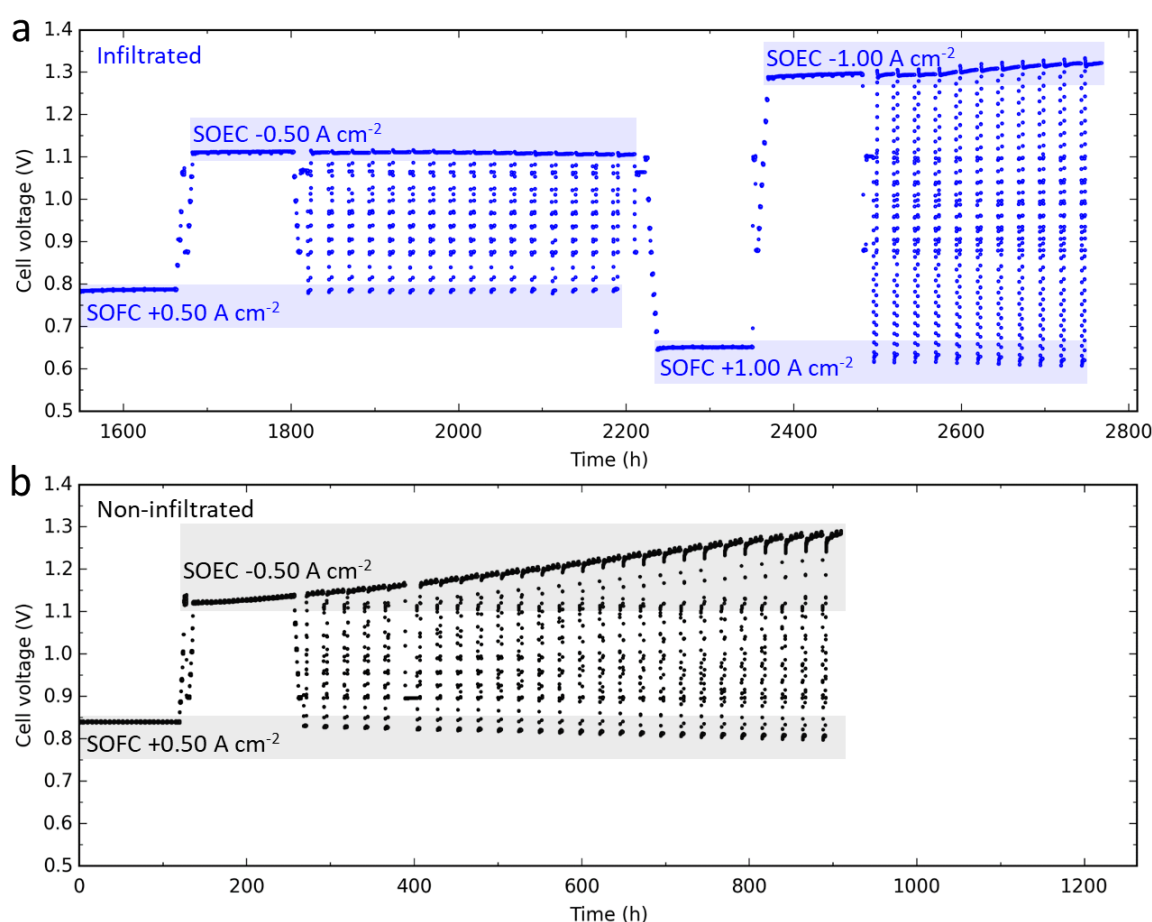


Figure 4.9: Comparison of the cell durability during reversible operation at 750 °C. Evolution of cell voltage as a function of time on (a) infiltrated cell and (b) non-infiltrated cell. When operated at $+0.50 \text{ A cm}^{-2}$ (fuel cell mode), the fuel and oxygen electrodes were fed with 12.8 l h^{-1} of $50\% \text{H}_2\text{-}50\% \text{N}_2$ and 60 l h^{-1} of dry air, respectively. When operated at -0.50 A cm^{-2} (electrolysis mode), the fuel and oxygen electrodes were fed with 8.0 l h^{-1} of $80\% \text{H}_2\text{O-}20\% \text{H}_2$ and 12 l h^{-1} of dry air, respectively. For $\pm 1.00 \text{ A cm}^{-2}$, the composition of gas feeds was the same as that of $\pm 0.50 \text{ A cm}^{-2}$ but with a doubled flow rate.

Figure 4.10 shows SEM images of the CGO-Ni/YSZ electrode of the infiltrated cell after the durability tests of steam electrolysis and cyclic operation (in total $\sim 2800 \text{ h}$). The examined location is at the gas inlet, where the microstructural changes of the Ni/YSZ electrode are usually more pronounced than at the center or the gas outlet due to the decrease of overpotential along the fuel flow.[42, 128] Only a slight loss of Ni percolation is observed at close to the electrode/electrolyte interface (**Figure 4.10a**), indicating alleviated Ni migration on the infiltrated cell with the CGO-Ni/YSZ electrode when compared with

previously reported cells with bare Ni/YSZ electrodes tested under similar conditions. [42, 44] Note that a cell with CGO-Ni/YSZ electrode but achieved by treating the cell with a “two-atmosphere-reduction” followed by CGO infiltration, has also been reported with the slight Ni loss after tested for steam electrolysis at -1.25 A cm^{-2} and $800 \text{ }^\circ\text{C}$ for 1000 h. [50] The microstructure of CGO coating changed significantly after the durability tests (**Figure 4.2e** and **Figure 4.10b**). The nano-CGO particles clearly coarsened to the size of 70-130 nm (**Figure 4.10b**). The coarsening of nano-CGO may be the major contributor to the degradation of the infiltrated cell, and it is expected to be mitigated by operating the cell at lower temperatures.

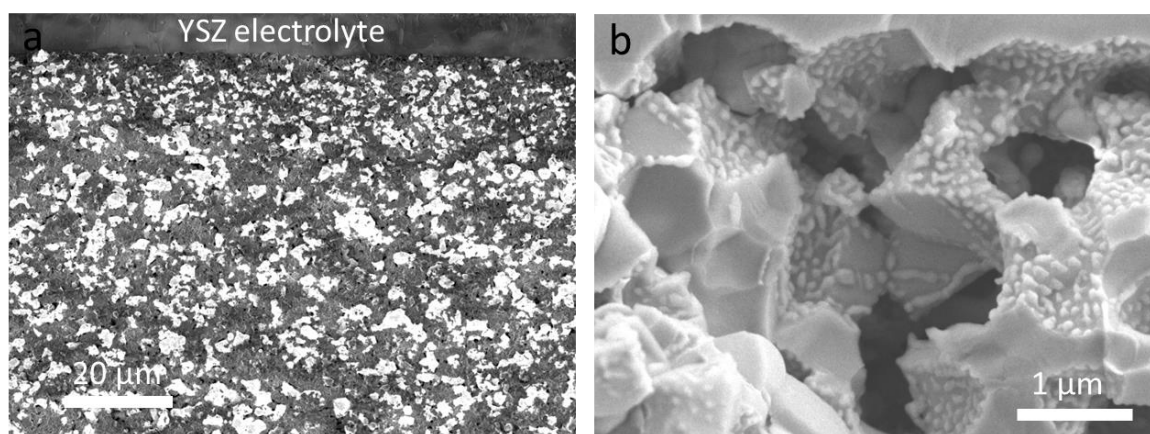


Figure 4.10: SEM characterization of the CGO-Ni/YSZ fuel electrode of the infiltrated cell after the durability test. (a) Showing Ni percolation, and (b) showing fracture surface.

It has here been demonstrated that tailoring of the Ni/YSZ electrode by infiltration can be done at single cell level even after reducing the full cell. This is practical from a manufacturing point of view compared to previously applied “two-atmosphere” treatments and has some distinct advantages over a post-stack assembly infiltration [151] as was discussed in ref [155]. First, it allows more careful quality and process control at single cell level when all steps in the cell manufacturing have been completed. Also, the cells are in fact more robust for strain loading, [155] when in reduced state than when in oxidized state, which can be an advantage in handling and during stacking.

4.4 Conclusion

In summary, we demonstrated an up-scalable, effective route for infiltrating CGO electrocatalysts into the Ni/YSZ electrode after exposing the full cell to a “one-atmosphere-reduction”. When operated for steam electrolysis at 750 °C, the observed cell voltage degradation rates of the infiltrated cell are 0.028 V kh⁻¹ (2.0 % kh⁻¹) at -1.25 A cm⁻² and 0.010 V kh⁻¹ (0.8 % kh⁻¹) at -1.00 A cm⁻², ~14 times and ~25 times smaller than the degradation rates for the non-infiltrated cell, respectively. For reversible operation at +/-0.50 A cm⁻², no obvious signs of degradation could be observed on the infiltrated cell, showing significantly improved durability compared with the non-infiltrated cell. The results of EIS data recorded at OCV and under current load substantiate the finding that the CGO infiltration not only improves the initial electro-catalytic activity of the Ni/YSZ electrode but also strongly enhances the electrode durability. The EIS results also demonstrate a small improvement of the performance of the LSCF/CGO oxygen electrode after the redox cycle introduced via the “one-atmosphere-reduction” and the subsequent reoxidation at the start of testing.

CHAPTER 5

Promotion of oxygen reduction and evolution by applying a nanoengineered hybrid catalyst on cobalt free electrodes for solid oxide cells

Abstract

A key requirement for the widespread commercialization of solid oxide cell (SOC) technology is to develop cost-effective oxygen electrodes with sufficiently high electro-catalytic activity and durability at intermediate temperatures (600–750 °C). Here we report a remarkable enhancement of electro-catalytic activity of cobalt-free $\text{La}_{0.6}\text{Sr}_{0.4}\text{FeO}_{3-\delta}$ (LSF) electrode by applying a nanoengineered hybrid catalyst coating composed of nanoparticles of $\text{Ce}_{0.85}\text{Gd}_{0.15}\text{O}_{2-\delta}$ (CGO) and PrO_x via infiltration. Different from the conventional infiltration with a precursor of metal nitrate, here a mixture solution of colloidal CGO nanocrystals and $\text{Pr}(\text{NO}_3)_3$ is used for infiltration to enable the desired nanoengineered architecture. The hybrid-catalyst-coated LSF oxygen electrode displays a very low polarization resistance of $0.017 \Omega \text{ cm}^2$ at 750 °C, about one order of magnitude lower than that of the bare LSF ($0.197 \Omega \text{ cm}^2$). Furthermore, the hybrid-catalyst-coated LSF electrode shows excellent performance in both fuel cell and electrolysis modes, while it also offers good durability over more than 1000 h of operations. The superior performance and durability are attributed to the combined effects of accelerating oxygen surface exchange kinetics by PrO_x and enhancing the surface area for catalytic reaction by the nanoporous architecture of the catalyst coating. This work not only opens the opportunity for applying the cobalt-free oxygen electrode in SOCs but also proposes a smart co-infiltration strategy to develop highly active and robust catalyst coating by combinedly tuning the composition and morphology, which may also be applicable to other devices such as metal-air batteries and membrane reactors.

5.1 Introduction

Reducing the operating temperature to the intermediate temperature range (600–750 °C) will be highly beneficial to enable the widespread commercialization of the SOC technology. One of the technical challenges for operating SOCs in this temperature range is to ensure sufficiently high electro-catalytic activity toward the oxygen reduction reaction (ORR, when operated in fuel-cell mode) and the oxygen evolution reaction (OER, when operated in electrolysis mode) as well as good durability. During the past decades, substantial efforts have been made, leading to a shift in oxygen electrode materials from the conventional electronic conducting $\text{La}_{1-x}\text{Sr}_x\text{MnO}_3$ (LSM) compound to mixed ionic-electronic conductors (MIECs). In particular, many cobalt-containing perovskite-type oxides, such as $\text{La}_{0.6}\text{Sr}_{0.4}\text{Co}_{0.2}\text{Fe}_{0.8}\text{O}_{3-\delta}$ (LSCF) [23], $\text{La}_{0.6}\text{Sr}_{0.4}\text{CoO}_{3-\delta}$ (LSC) [25], $\text{Ba}_{0.5}\text{Sr}_{0.5}\text{Co}_{0.8}\text{Fe}_{0.2}\text{O}_{3-\delta}$ (BSCF) [27], $\text{Sm}_{0.5}\text{Sr}_{0.5}\text{CoO}_{3-\delta}$ (SSC) [26], and $\text{PrBa}_{0.8}\text{Ca}_{0.2}\text{Co}_2\text{O}_{5+\delta}$ (PBCC) [77], have been developed, and have shown to provide favorable catalytic activity at intermediate temperatures. Nevertheless, these cobalt-containing materials are not without problems. The materials show a large thermal expansion mismatch with commonly used electrolyte materials, i.e., yttria-stabilized zirconia (YSZ) and scandium-stabilized zirconia (SSZ); the chemical stability of them is not excellent; the volatilization and diffusion of cobalt during the high-temperature sintering process cause various cell fabrication issues [30-32]. Furthermore, cobalt is price volatile and it may become resource-limited due to the rocketing demand of cobalt oxide for lithium-ion batteries [31]. Finally, it is considered carcinogenic. All these factors push the development of cobalt-free electrodes for SOCs.

LaFeO_3 -based oxides are attractive alternatives because of their similar thermal expansion coefficients to that of the conventional electrolyte materials and improved chemical stability as well as the high abundance and low cost of iron. [156, 157] However, LaFeO_3 -based materials exhibit relatively low catalytic activity for ORR and OER in comparison with cobalt-containing materials. For example, $\text{La}_{0.5}\text{Sr}_{0.5}\text{FeO}_{3-\delta}$ electrode was reported to show a polarization resistance (R_p) of $0.79 \Omega \text{ cm}^2$ at 700 °C [158], more than 2 times that of the most commonly used LSCF electrode ($0.34 \Omega \text{ cm}^2$) under the same conditions [159]. The R_p of $\text{La}_{0.5}\text{Sr}_{0.5}\text{FeO}_{3-\delta}$ electrode can be reduced to a value comparable to that of LSCF by substitution with other elements than Co on the Fe site. A value of $0.35 \Omega \text{ cm}^2$ has been reported for $\text{La}_{0.5}\text{Sr}_{0.5}\text{Fe}_{0.8}\text{Cu}_{0.15}\text{Nb}_{0.05}\text{O}_{3-\delta}$ at 700 °C [92]. This value though

matching that of LSCF is still ~ 4 times higher than that of more cobalt-rich composite like PBCC electrodes ($0.071 \Omega \text{ cm}^2$) under the same conditions [77], and ~ 50 % higher than that of BSCF electrode ($0.22 \Omega \text{ cm}^2$) at a temperature of $650 \text{ }^\circ\text{C}$. [160]

Recently, surface modification via infiltration of oxygen electrodes with catalytically-active nanoparticles/coating has emerged as an effective approach to enhance the activity. [77, 78, 80, 81, 161] Several kinds of catalyst coatings have been deposited onto LSCF electrode surfaces via infiltration. In such catalyst-coated LSCF electrodes, the porous LSCF backbones provide a highly continuous pathway for the transport of both oxygen ions and electrons while the catalyst coatings offer enhanced surface oxygen exchange kinetics and tolerance to contaminant poisoning and in some cases improved durability. [78, 161] For instance, a coating of $\text{PrSrCoMnO}_{6-\delta}$ (PSCM) on LSCF reduced the R_p from 0.126 to $0.093 \Omega \text{ cm}^2$ at $750 \text{ }^\circ\text{C}$. [162] A multi-phase catalyst coating has also been reported to not only dramatically reduce the R_p from $2.57 \Omega \text{ cm}^2$ (for bare LSCF) to $0.312 \Omega \text{ cm}^2$ at $600 \text{ }^\circ\text{C}$ but also to enhance the durability. [79] In the above examples, the coatings were introduced by infiltration of nitrate solutions that were subsequently decomposed via heat treatment. By this approach the overall composition of the coating is well controlled but the phase and the morphology of coating, which is also important for performance, is not well controlled. It will among other things depend on the temperature of the firing step.

Here, we report on $\text{La}_{0.6}\text{Sr}_{0.4}\text{FeO}_{3-\delta}$ (LSF)-based electrodes that can be strongly improved to a level allowing operation between 650 and $750 \text{ }^\circ\text{C}$ by applying a nanoengineered hybrid catalyst coating realized through a nonconventional infiltration route. The hybrid coating is composed of nanoporous layer of nanoparticles of $\text{Ce}_{0.85}\text{Gd}_{0.15}\text{O}_{2-\delta}$ (CGO) and PrO_x . The coating is achieved by infiltrating the porous LSF with a solution of colloidal CGO nanocrystals and $\text{Pr}(\text{NO}_3)_3$. PrO_x was included because of its good catalytic activity towards the ORR. [110, 163] The resulting hybrid-catalyst coated LSF electrode displayed a very low R_p of $0.017 \Omega \text{ cm}^2$ at $750 \text{ }^\circ\text{C}$. This performance is comparable to those of the high-performance cobalt-containing electrodes mentioned previously. The effect of coating on oxygen surface exchange kinetics was investigated by electrical conductivity relaxation (ECR) measurements. Moreover, the electrode demonstrated excellent durability in full cells for both practical fuel-cell and electrolysis operations.

5.2 Results and discussion

5.2.1 Microstructure of LSF electrodes

CGO nanocrystals were synthesized through continuous hydrothermal flow synthesis (CHFS), as reported previously. [164] The shapes and exposed facets of the CGO nanocrystals were examined using transmission electron microscopy (TEM). A typical TEM image of CGO nanocrystals in **Figure 5.1a** shows crystallites of well-defined octahedral shapes with sizes of 25-45 nm. **Figure 5.1b** shows a high-resolution transmission electron microscopy (HRTEM) image of a typical octahedron, indicating that the octahedron was dominated by {111} facets with the lattice fringes at 0.31 nm. [164, 165]

Shown in **Figure 5.1c** is a typical SEM image of the bare LSF electrode backbone after firing at 1100°C for 5 h, showing smooth surfaces and clear grains. In **Figures 5.1b-d**, images of CGO, PrO_x, and the hybrid-catalyst (CGO+PrO_x)-coated LSF electrodes are displayed. The electrodes were prepared by infiltrating a colloidal CGO nanocrystal solution, Pr(NO₃)₃ solution, and mixture of the two into the porous LSF backbones and calcinating at 750 °C for 4 h. The loading of coating was 9 wt.% relative to the porous LSF backbones. **Figure 5.1d** shows that CGO nanocrystals are uniformly deposited on the LSF grains and that they have maintained their shapes. Once coated with the PrO_x catalyst, the continuous and dense film is observed on the surface of the LSF grains, making it appear rougher (**Figure 5.1e**). **Figure 5.1f** shows that the hybrid catalyst covers the LSF very well with particle size of 25–60 nm and forms a nanoporous coating. Compared to the dense PrO_x coating obtained after Pr(NO₃)₃ infiltration, this nanoporous hybrid catalyst coating achieved by co-infiltration of colloidal CGO nanocrystals and Pr(NO₃)₃ may largely enhance the surface area for the catalytic reaction. This was demonstrated by the Brunauer-Emmett-Teller (BET) results, in which the measured surface areas for the bare LSF, CGO-coated LSF, PrO_x-coated LSF, and hybrid-catalyst-coated LSF electrodes were 1.2, 2.9, 2.1 and 3.0 m² g⁻¹, respectively. In addition, introducing CGO nanocrystals decreases the use of praseodymium which is costly.

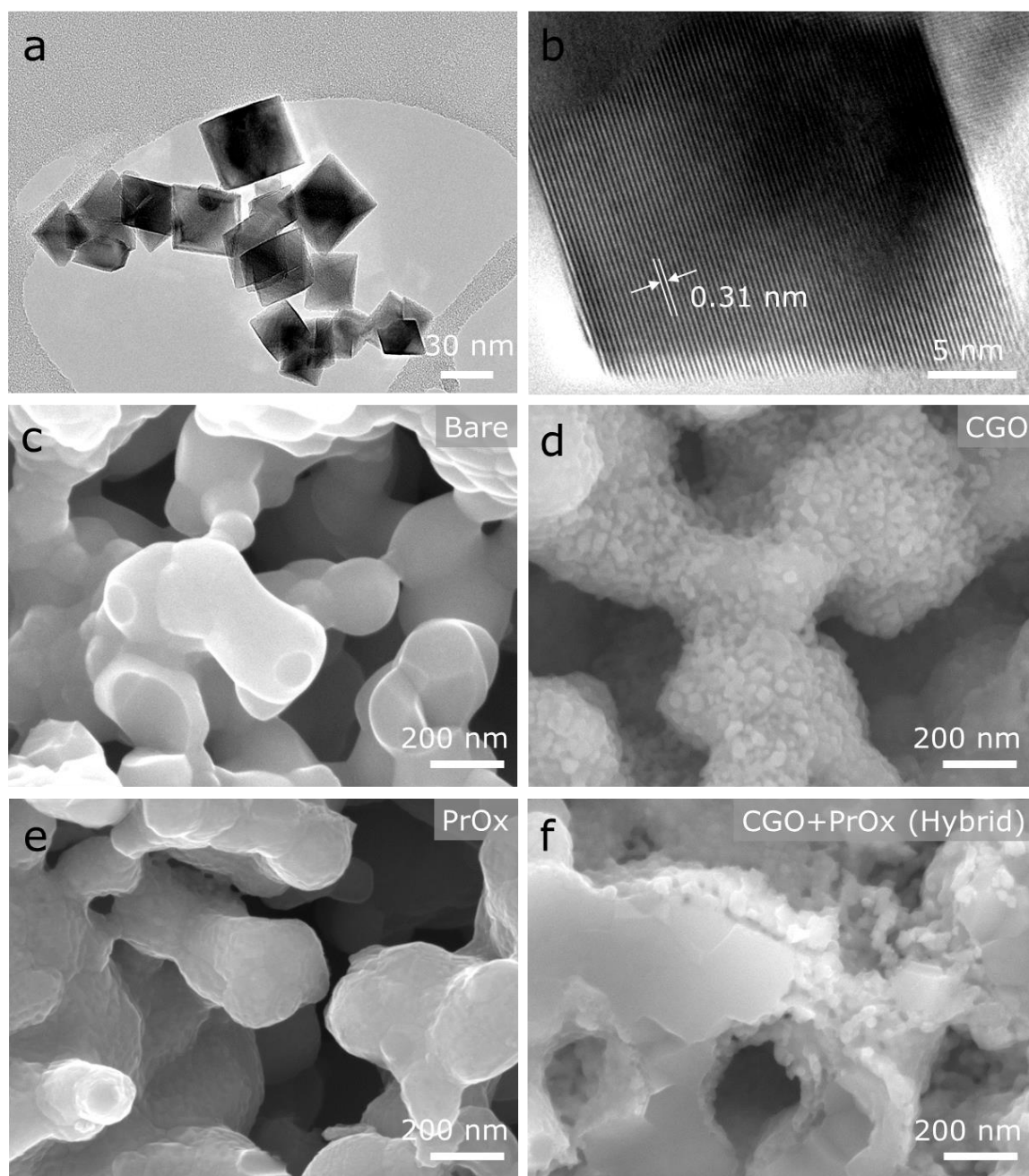


Figure 5.1: (a) TEM and (b) HRTEM images of CGO nanocrystals. Cross-sectional SEM images of four types of LSF electrodes. (c) Bare LSF, (d) CGO-coated LSF, (e) PrO_x-coated LSF, and (f) hybrid-catalyst-coated LSF.

5.2.2 Performance and durability of the LSF electrodes

The electrochemical performance of the bare LSF, CGO-coated LSF, PrO_x-coated LSF, and hybrid-catalyst (CGO and PrO_x)-coated LSF electrodes was evaluated by measuring the electrochemical impedance spectra (EIS) of symmetrical cells with a configuration of electrode/electrolyte/electrode. **Figures 5.2a** and **2b** compare Nyquist plots of EIS data for the four types of LSF electrodes obtained at 750 and 650 °C, respectively. Clearly, all of the coated LSF electrodes show significantly reduced polarization resistances (R_p) when compared to the bare LSF. The hybrid-catalyst-coated LSF electrode displays the lowest R_p among them. For instance, the R_p value of the hybrid-catalyst-coated LSF at 750 °C is $0.017 \Omega \text{ cm}^2$, about one order of magnitude lower than that of the bare LSF ($0.197 \Omega \text{ cm}^2$), $\sim 81\%$ lower than that of CGO-coated LSF ($0.089 \Omega \text{ cm}^2$), and $\sim 39\%$ lower than that of PrO_x-coated LSF ($0.028 \Omega \text{ cm}^2$) under the same conditions.

The performance of the hybrid-catalyst-coated LSF electrode reported here is comparable to those of the high-performance cobalt-containing electrodes reported recently, including LSCF or LSCF nanofiber [159], BSCF-Ce_{0.9}Gd_{0.1}O_{2- δ} (CGO10) mixture or nanofibers [160], SrTi_{0.3}Fe_{0.63}Co_{0.07}O_{3- δ} (STFC) [96] and PBCC [77] as well as several representative surface-coated-electrodes such as PSCM-coated LSCF [162], PrNi_{0.5}Mn_{0.5}O₃ (PNM) thin film and PrO_x nanoparticles -coated LSCF [78], multi-phase catalysts (composed of BaCoO_{3- x} (BCO) and PrCoO_{3- x} (PCO) nanoparticles and a conformal PBCC thin film)-coated LSCF [79], and SSC-coated LSCF/CGO10 [81] (**Figure 5.2c**). In one exception, Nicollet et al. reported even better performing cobalt-free electrodes, i.e., Pr₆O₁₁-coated CGO10 electrodes, which achieved polarization resistances as low as $0.028 \Omega \text{ cm}^2$ at 600 °C, prepared by infiltrating Pr(NO₃)₃ into the porous CGO10 backbone. [110] Compared to the hybrid-catalyst-coated LSF electrode developed in this work, the above Pr₆O₁₁-coated CGO10 electrodes are with a higher loading of Pr₆O₁₁ catalysts (30 wt.% relative to the CGO10 backbone) and calcinated at a lower temperature of 600 °C for 2 h before being tested. Note that the calcination temperature and catalyst loading can significantly influence the performance of infiltrated electrodes. [74, 166] The performance of the hybrid-catalyst-coated LSF electrode may be further improved by, for example, using CGO nanocrystals with smaller size or optimizing the component ratio or loading of the hybrid catalyst. Such studies will be part of our future work.

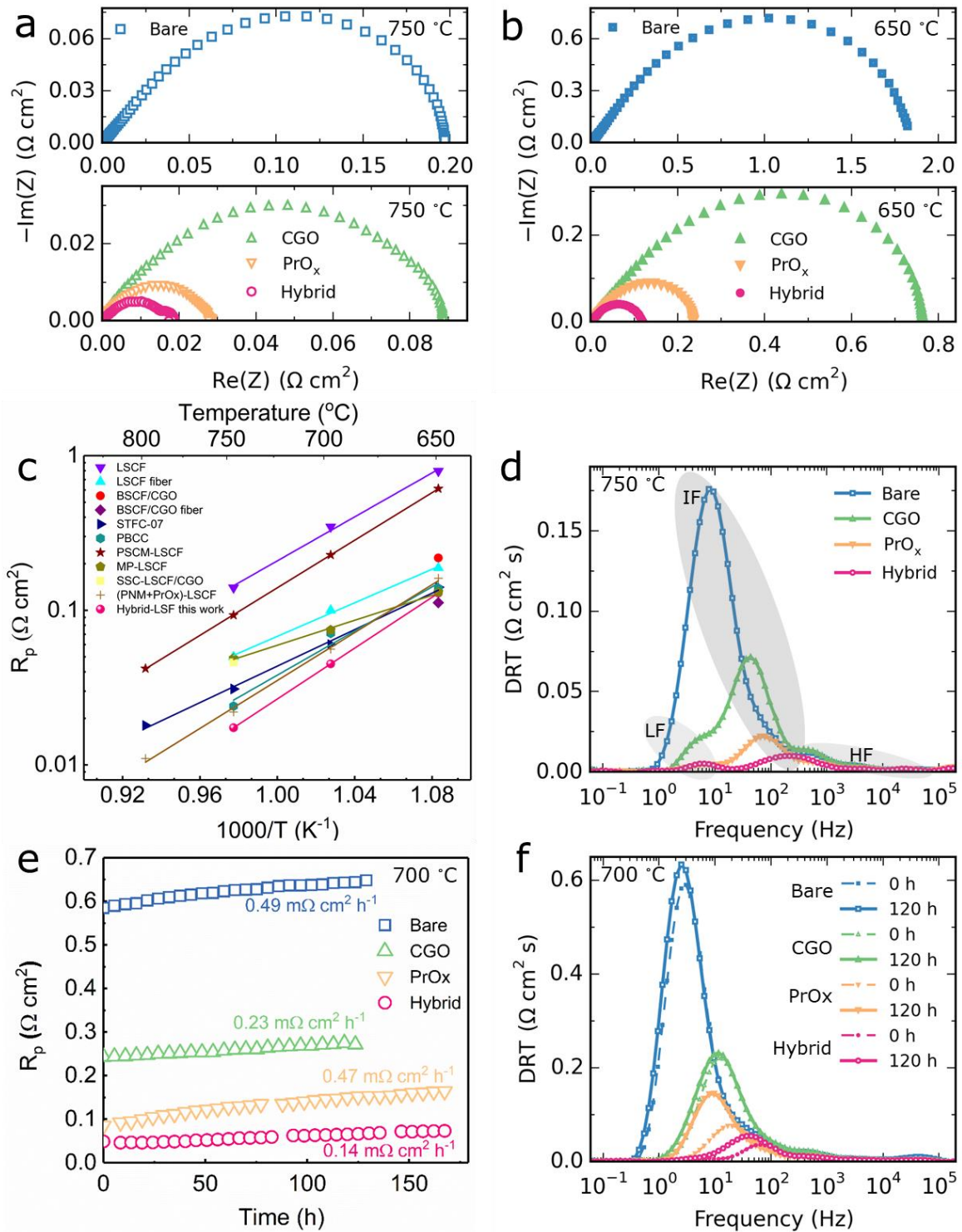


Figure 5.2: Electrochemical performance and durability of symmetrical cells with four types of LSF electrodes measured under OCV conditions. Nyquist plots of EIS data measured at (a) 750 °C and (b) 650 °C. (c) Comparison of R_p of hybrid-catalyst-coated LSF electrode with some high-performance cobalt-containing electrodes reported recently. (d) DRT plots of EIS data for four types of LSF electrodes measured at 750 °C. (e) Durability on

symmetrical cells with four types of LSF electrodes at 700 °C under OCV condition. (f) DRT plots at 0 h and 120 h.

The kinetics of the electrochemical processes on these LSF electrodes were investigated by examining the distribution of relaxation time (DRT) of the EIS data. DRT analysis is a useful tool for deconvoluting the complex EIS data to separate the contributions of some key steps from the total R_p of electrode reactions. In general, each peak in DRT plots represents an electrode process, and its integral area corresponds to the resistance contribution of that process. The higher the characteristic frequency of the peak, the faster the relaxation of the corresponding process. Shown in **Figure 5.2d** is the comparison of DRT plots for symmetrical cells with the four types of LSF electrodes. **Figure 5.S1** contains Nyquist and DRT plots of bare LSF electrode under different oxygen partial pressures (pO_2) and of the hybrid-catalyst-coated electrode at different temperatures. In these DRT plots three distinct peaks are identified in the frequency range of 0.3–100 kHz, they are denoted as low frequency (LF), intermediate frequency (IF), and high frequency (HF). The LF peak has little dependence on temperature while the other peaks are characterized by a pronounced thermal activation (**Figure 5.S1b**). This strongly indicates that the LF peak is related to gas diffusion within the pores of the electrodes since gas diffusion process is only mildly temperature dependent. [79] The IF peak has a strong dependence on temperature and pO_2 (**Figures 5.S1b** and **S1d**), indicating that the IF peak is associated with the oxygen surface exchange processes including oxygen adsorption/desorption, dissociation, and/or surface diffusion. [77, 79] The insensitivity of the HF peak to pO_2 (**Figure 5.S1d**) suggests that the HF peak is likely related to transport of O^{2-} within the LSF backbone and/or across the electrode/electrolyte interface, which are pO_2 less dependent processes. [77, 79] It is clearly seen in **Figure 5.2d** that at 750 °C the resistance of IF peak (surface exchange processes) dominates the total R_p of the bare LSF electrode, and that this peak decreases significantly by introducing coatings on the electrode. Also, its characteristic frequency shifts to higher values. The hybrid-catalyst-coated electrode has the highest characteristic frequency and the lowest resistance of the IF peak.

These results are consistent with results of characterizations of the surface exchange coefficient (k) from electrical conductivity relaxation (ECR) measurements. Results of ECR experiments on as prepared LSF bars and surface coated ones are reproduced in **Figure 5.S2**. The k value of a bar of LSF is significantly increased after coating with catalysts, and the

hybrid catalyst coated LSF possesses the highest k value. For example, the k values at 750 °C are 2.07×10^{-4} , 9.71×10^{-4} , $1.67 \times 10^{-3} \text{ cm s}^{-1}$ for the bare LSF, PrO_x -coated LSF, and the hybrid-catalyst-coated LSF, respectively. The activation energy (E_a) for oxygen surface exchange decreases from 2.49 eV on bare LSF to 0.68 eV on PrO_x -coated LSF, and 0.96 eV on hybrid-catalyst-coated LSF. The lowest E_a of the PrO_x -coated LSF electrode may suggest that PrO_x has the highest intrinsic activity for oxygen exchange, while the hybrid-catalyst-coated LSF electrode shows the highest k in ECR and lowest R_p in the symmetrical cell due most likely to its unique nanostructure, which combines the effects of high intrinsic activity of PrO_x and the large surface area enabled by the CGO nanocrystals.

The short-term durability of four types of LSF electrodes was investigated using symmetrical cells aged at 700 °C. The evolution in R_p with time is summarized in **Figure 5.2e**. The order in degradation rate is: bare LSF ($0.49 \text{ m}\Omega \text{ cm}^2 \text{ h}^{-1}$) > PrO_x -LSF ($0.47 \text{ m}\Omega \text{ cm}^2 \text{ h}^{-1}$) > CGO-LSF ($0.23 \text{ m}\Omega \text{ cm}^2 \text{ h}^{-1}$) > hybrid-LSF ($0.14 \text{ m}\Omega \text{ cm}^2 \text{ h}^{-1}$). **Figure 5.2f** shows a comparison of DRT plots at 0 h and 120 h for the four types of symmetrical cells. After 120 h of tests, all of the DRT plots display a shift in characteristic frequency to lower frequency on the IF peak and an accompanying increase of the corresponding integral resistance, reflecting a reduced rate of the surface exchange process on the electrodes. Remarkably, the CGO-coated LSF and hybrid-catalyst-coated LSF electrodes show a significantly smaller increase in the IF peak resistance in comparison with that of PrO_x -coated LSF, revealing a positive effect on electrode durability of introducing CGO nanocrystals into the coating.

5.2.3 Performance and durability of full cells incorporating the hybrid-catalyst-coated LSF oxygen electrodes

To evaluate the performance of the hybrid-catalyst-coated LSF oxygen electrode in an actual full cell, fuel-electrode-supported cells with a configuration of Ni/YSZ support | Ni/YSZ fuel electrode | YSZ electrolyte | CGO10 barrier | hybrid-catalyst-coated LSF oxygen electrode (hybrid-catalyst-coated LSF cell) were fabricated and tested under both fuel cell and electrolysis operating conditions. Cross-sectional views of the cell components are shown in **Figure 5.S3**. **Figure 5.3a** shows the typical I-V-P curves of the cell tested under

representative fuel cell conditions with 4% H₂O-96% H₂ fed to the fuel electrode and dry air to the oxygen electrode. For comparison, the performance of a cell with a bare LSF electrode (LSF cell) was also characterized under identical test conditions. The hybrid-catalyst-coated LSF cell delivers peak power densities (PPDs) of 1.57, 1.15, 0.67 W cm⁻² at 750, 700, and 650 °C, respectively, about 70, 130, and 170 % higher than those of the LSF cell (0.94, 0.50, 0.25 W cm⁻² at 750, 700, and 650 °C, respectively).

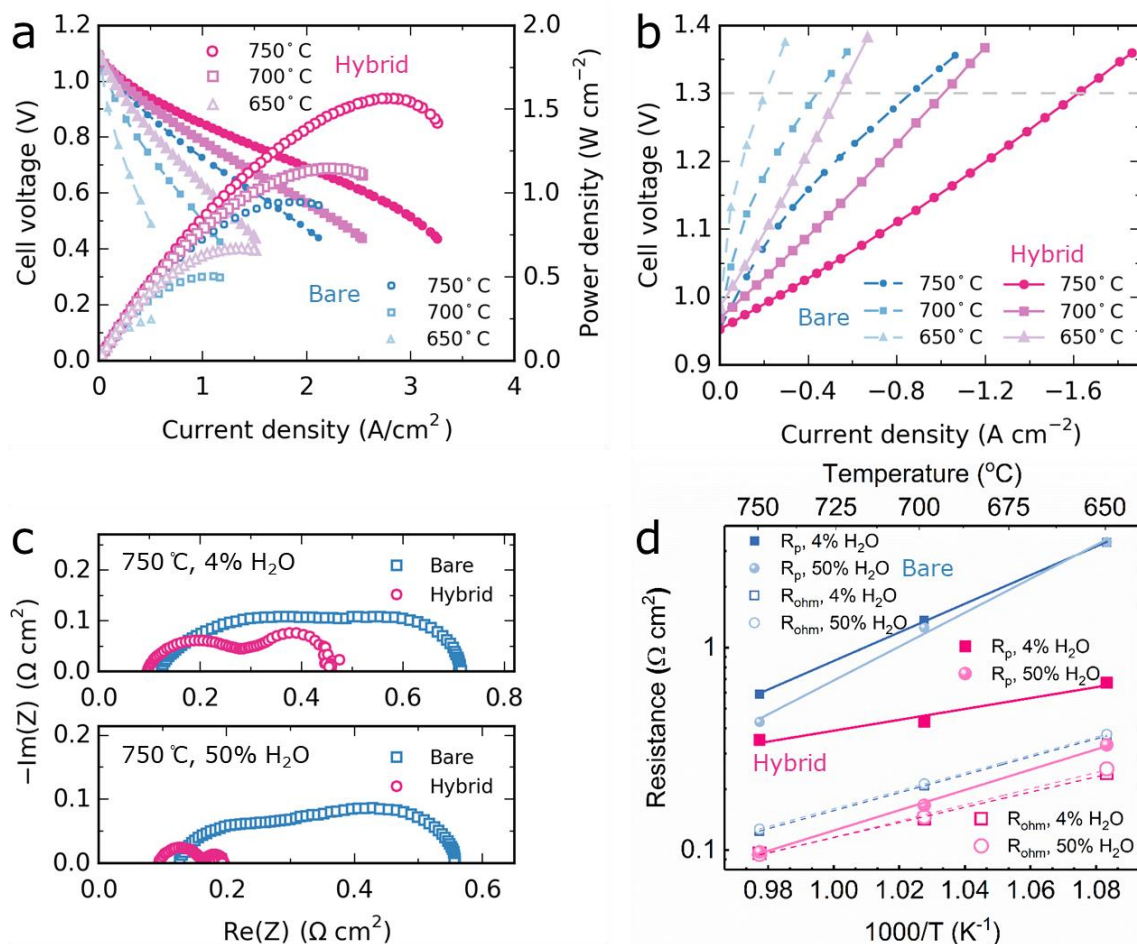


Figure 5.3: Electrochemical performance on Ni/YSZ fuel-electrode-supported cells with the bare LSF and hybrid modified LSF oxygen electrodes. (a) Voltage and power density versus current density (I-V-P) measured at 650–750 °C with 4% H₂O-96% H₂ fed to the fuel electrode and dry air to the oxygen electrode (fuel cell mode). (b) Voltage versus current density (I-V) measured at 650–750 °C with 50% H₂O-50% H₂ fed to the fuel electrode and dry air to the oxygen electrode (electrolysis mode). (c) Nyquist plots of EIS data recorded at 750 °C under OCV. (d) Comparison of R_{ohm} and R_p under OCV.

Figure 5.3b shows the I-V curves of the cells tested under electrolysis conditions with 50% H_2O -50% H_2 fed to the fuel electrode and dry air to the oxygen electrode. At the preferred electrolysis operation voltage of 1.3 V, the current densities of the hybrid-catalyst-coated LSF cell are 1.62, 1.01, 0.54 A cm^{-2} at 750, 700, and 650 $^\circ\text{C}$, respectively; these values are about 90, 130, and 170 % higher than those of the LSF cell (0.86, 0.44, 0.20 A cm^{-2} at 750, 700, and 650 $^\circ\text{C}$, respectively). In light of the results on symmetrical cells, this significantly improved performance observed on the hybrid-catalyst-coated LSF cell under realistic fuel cell and electrolysis operating conditions is as expected. The results demonstrate that surface modification by the suggested nano-engineered hybrid catalyst coating can be effectively transferred to real cell architecture resulting in very well performing cells. Encouragingly, the behavior of the hybrid-catalyst-coated LSF cell reported here competes well with those of high-performance SOCs based on cobalt-containing electrodes [77, 78, 81, 162, 167].

Figure 5.3c shows typical EIS data of the hybrid-catalyst-coated LSF cell and the LSF cell acquired at 750 $^\circ\text{C}$ under OCV conditions. The polarization resistance (R_p) is significantly reduced by introducing the hybrid-catalyst coating, meanwhile the ohmic resistance (R_{ohm}) also decreases slightly. For example, the R_p of the hybrid-catalyst-coated LSF cell is 0.098 $\Omega \text{ cm}^2$ under 50% H_2O -50% H_2 fed to the fuel electrode, as only 23 % of that of the LSF cell (0.429 $\Omega \text{ cm}^2$) under identical test conditions. Moreover, the hybrid-catalyst-coated LSF cell shows lower activation energy of R_p compared with the LSF cell (**Figure 5.3d**), consistent with the more significant improvement in performance at low temperature observed from the I-V curves in **Figures 5.3a** and **3b**.

Durability is one of the key factors determining the practical application of SOCs. The long-term durability of the hybrid-catalyst-coated LSF cell was evaluated at 650 $^\circ\text{C}$ in both fuel-cell and electrolysis modes, as shown in **Figure 5.4**. When operated in fuel-cell mode under a constant current density of 0.5 A cm^{-2} , the cell experiences an initial degradation followed by an activation during the first 300 h (**Figure 5.4a**). Subsequently, it displays excellent durability in the following 800 h. EIS data measured during the durability test shows that it is the R_p that dictates the evolution of total resistance (**Figure 5.4b**). R_p first increases and then decreases over the first 300 h, and gets stable afterwards. R_{ohm} is practically unaltered over the test period. This durability is superior to that reported for a metal-supported cell with PrO_x infiltrated YSZ oxygen electrode, showing a voltage

degradation of ~30% over 100 h of operation at 700 °C and 0.7 V.[163] The degradation of that cell was reported due mainly to the coarsening of PrO_x resulting in the transformation of the porous microstructure to a dense blanket. [163]

When operated for steam electrolysis under a constant current density of -0.5 A cm^{-2} , however, the hybrid-catalyst-coated LSF cell shows a considerable degradation. The cell voltage increases from 1.260 to 1.491 V in a test period of 500 h, with an accelerating degradation in the first 400 h (**Figure 5.4c**). The degradation rate reaches a peak value of 0.998 V kh^{-1} at 400 h. Similar to the observation during fuel-cell operation, the EIS data shows that the R_{ohm} is stable during the continuous electrolysis operation (**Figures 5.4d** and **4e**), whereas an increase in R_p from 0.387 to $0.741 \text{ } \Omega \text{ cm}^2$ is observed.

In order to clarify the contributions of each electrode to the increase in R_p , the EIS data shown in **Figure 5.4e** were analyzed using DRT. The results are shown in **Figure 5.4f**. **Figure 5.S4** presents the EIS data of the cell measured under different temperatures and gas conditions and corresponding DRT results. In all DRT plots four distinct peaks are identified, denoted P1 to P4 from high to low frequency, corresponding to at least four electrode processes. It is shown in **Figure 5.S4b** that the processes associated with P1, P2, and P3 are characterized by a pronounced thermal activation while P4 is not sensitive to temperature. **Figure 5.S4d** shows that P2 and P4 are very sensitive to the ratio of H_2O to H_2 in the fuel electrode while P1 and P3 are almost independent of that. On the basis of these results and previously reported analyses:[43, 44, 140] P1 is likely related to the transport of oxygen anions through the ionic conducting networks in the electrodes, and the major contribution of P1 might originate from the YSZ network of the fuel electrode; P₂ is associated with the hydrogen evolution reaction (HER) at the triple-phase boundaries (TPBs) of the fuel-electrode; P₃ is likely related to the OER at the TPBs of the oxygen electrode and P₄ represents the gas diffusion and conversion. **Figure 5.4f** shows that among four peaks the integral resistance of P2 dominates the total R_p at initial (0 h) and has the largest increase in 500 h operation, whereas the resistance of P3 is much smaller than that of P2 and remains relatively constant. These results suggest that the hybrid-catalyst-coated LSF oxygen electrode has good activity and durability for the OER when operated at this condition for steam electrolysis, and among the two electrodes of the present cell, the Ni/YSZ fuel electrode is the one limiting cell performance and durability.

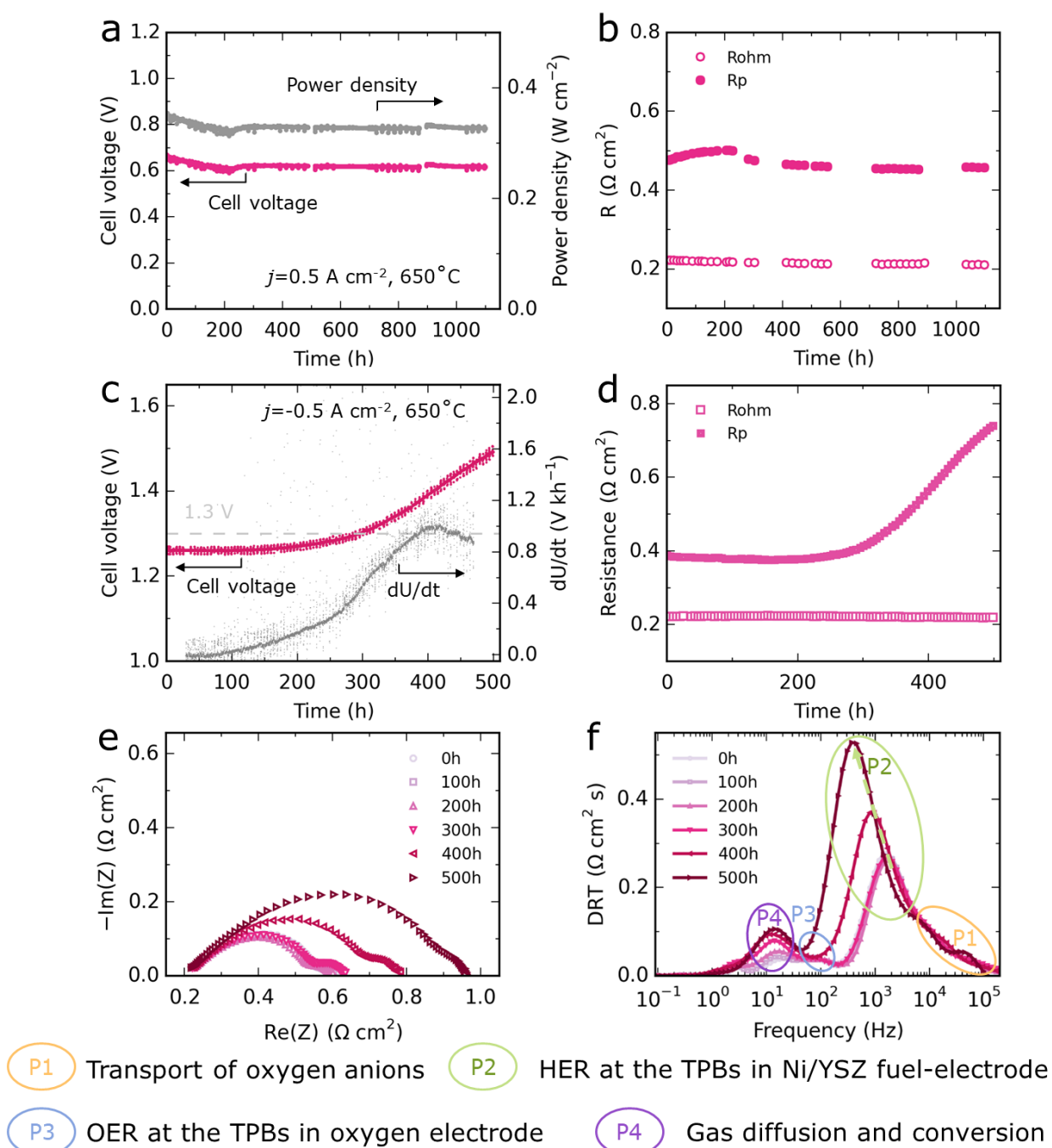


Figure 5.4: Durability on Ni/YSZ fuel-electrode-supported cells with the hybrid modified LSF oxygen electrode. Fuel cell operation under a constant current density of 0.5 A cm^{-2} at 650°C with $4\% \text{ H}_2\text{O}-96\% \text{ H}_2$ fed to the fuel electrode and dry air to the oxygen electrode: (a) Evolution of the cell voltage and power density, and (b) Evolution of R_{ohm} and R_p . Electrolysis operation under a constant current density of -0.5 A cm^{-2} at 650°C with $50\% \text{ H}_2\text{O}-50\% \text{ H}_2$ fed to the fuel electrode and dry air to the oxygen electrode: (c) Evolution

of the cell voltage, (d) Evolution of R_{ohm} and R_p , and (e) Nyquist plots and (f) DRT plots of EIS data recorded during electrolysis operation.

The observed degradation of the Ni/YSZ fuel electrode during electrolysis operation is not surprising and has been reported previously [42, 45, 47, 126]. Recently, some encouraging progress has been made into the degradation mechanism and strategies to reduce degradation. [44, 50, 127-130] We have found that surface modification of the Ni/YSZ electrode by coating nano-sized $Ce_{0.8}Gd_{0.2}O_{2-\delta}$ (CGO20) electrocatalysts is an effective approach to enhance the cell durability. [50, 127] Here, we applied this approach to the hybrid-catalyst-coated LSF cell such thus resulting in a double-side modified cell (with a CGO20-coated Ni/YSZ fuel electrode and the hybrid-catalyst-coated LSF oxygen electrode). At 1.3 V, the current densities of the such cell are 1.86, 1.41, 0.82 $A\ cm^{-2}$ at 750, 700, and 650 °C, respectively (**Figure 5.5a**). These values are higher than those of the hybrid-catalyst-coated LSF cell under identical conditions (**Figure 5.4b**), indicating an improvement in cell performance by introducing CGO20 coating into the Ni/YSZ electrode. **Figure 5.5b** summarizes the R_p and R_{ohm} values of the double-side modified cell at different temperatures. It is worth noting that at all three temperatures the R_{ohm} is higher than R_p and constitutes more than 50 % of the total resistance. Accordingly, future efforts in improving cell performance should be devoted to reducing the R_{ohm} by e.g., reducing the thickness of electrolyte and barrier layer, or introducing a better oxygen ionic conducting electrolyte materials like scandium-stabilized zirconia (SSZ).

More importantly, the double-side modified cell shows a significantly enhanced long-term durability under an electrolysis current density of 0.5 $A\ cm^{-2}$ at 650 °C (**Figures 5.5c and 5d**). After an accelerated degradation over the first 250 h, the degradation rate of the cell decreases continuously in the subsequent period. After 1400 h operation, the cell reached a voltage of 1.306 V (compared to 1.491V after 500 h for the hybrid-catalyst-coated LSF cell) and a degradation rate of $\sim 0.009\ V\ kh^{-1}$ ($\sim 0.69\ \%\ kh^{-1}$). The EIS results shown in **Figure 5.5d** confirms this durability behavior, where R_{ohm} is almost constant over the entire test period and the increase of R_p is slowing down gradually, showing an increase in R_p of less than $0.001\ \Omega\ cm^2$ for the last 500 h.

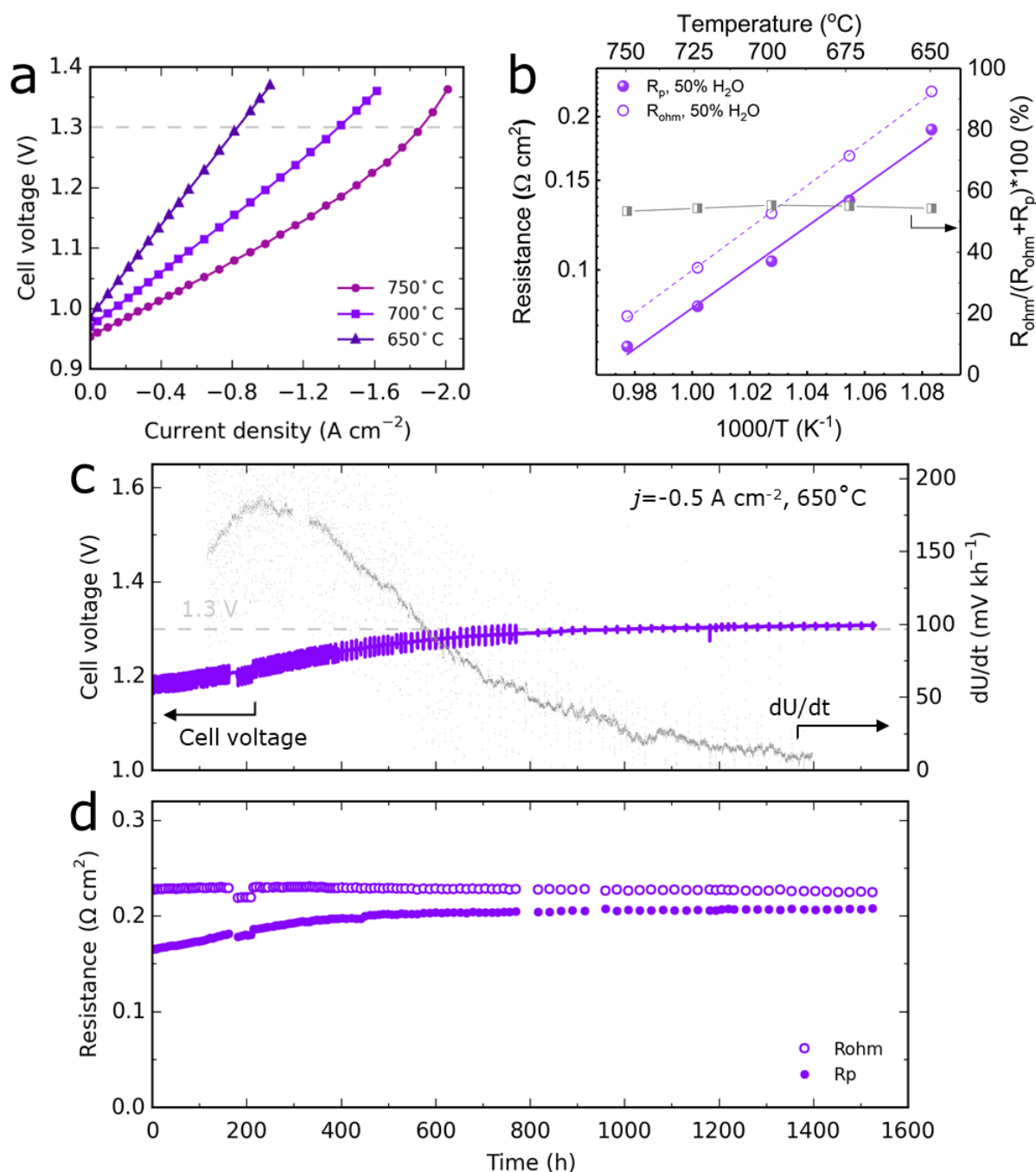


Figure 5.5: Electrochemical performance and durability for electrolysis operation on fuel-electrode-supported cell with the CGO20 modified Ni/YSZ fuel electrode and the hybrid modified LSF oxygen electrode, measured with 50% H_2O -50% H_2 fed to the fuel electrode and dry air to the oxygen electrode (a) Voltage versus current density measured at 650–750 °C. (b) R_p and R_{ohm} plotted as a function of inverse temperature (EIS data were recorded under OCV). Evolution of (c) cell voltage and (d) R_{ohm} and R_p under a constant current density of -0.5 A cm^{-2} at 650 °C.

5.3 Conclusion

In summary, the activity of LSF-based oxygen electrode for both the ORR and the OER has been strongly enhanced by applying a nanoporous hybrid catalyst coating composed of nanoparticles of CGO and PrO_x . The coating was realized using infiltration with a solution of colloidal CGO nanocrystals and $\text{Pr}(\text{NO}_3)_3$. The hybrid-catalyst-coated LSF electrode exhibited a very low polarization resistance of $0.017 \Omega \text{ cm}^2$ at $750 \text{ }^\circ\text{C}$ in symmetrical cell test, about one order of magnitude lower than that of bare LSF ($0.197 \Omega \text{ cm}^2$). Moreover, the durability of the hybrid-catalyst-coated LSF electrode for both the ORR and the OER was investigated in fuel-electrode-supported cells under practical operating conditions. Excellent performance and durability were observed. The analyses of SEM, BET, ECR as well as EIS indicated that the PrO_x greatly accelerates the oxygen surface exchange kinetics and the nanoporous architecture of the catalyst coating significantly increases the surface area for the oxygen incorporation reaction, thus enabling the superior activity and durability. This work shows that well performing cobalt-free oxygen electrode can be prepared and that when applied on a CGO modified Ni/YSZ electrode supported cell stable operation at $650 \text{ }^\circ\text{C}$ under -0.5 A cm^{-2} with cell voltage close to 1.3 V can be achieved.

5.4 Experimental

5.4.1 Synthesis and characterization of CGO nanocrystals

The CGO nanocrystals used in this work were synthesized by a continuous hydrothermal flow synthesis (CHFS) method. The process details can be found elsewhere. [164] Shortly, in an in-house developed CHFS flow-type reactor, a precursor stream of $\text{Ce}(\text{NO}_3)_3$ (0.04 mol L^{-1}) and $\text{Gd}(\text{NO}_3)_3$ (0.01 mol L^{-1}) was mixed with a stream of supercritical water (396 °C, 26 MPa). The nanocrystals nucleated and grew upon mixing. The nanocrystals were collected in the outflow that was cooled down and depressurized to atmospheric pressure. The nanocrystals were then separated from the suspension by using a centrifuge, washed in deionized water and ethanol, and dried for later processes. Bright field TEM (BF-TEM) and high-resolution TEM (HR-TEM) images were taken on a JEOL 3000F field emission transmission electron microscope that operates at 300 kV.

5.4.2 Fabrication of symmetrical cells

Symmetrical cells with the bare LSF electrodes were prepared by printing an in-house LSF ink onto both sides of commercially available CGO10 electrolyte (KERAFOL). The ink was obtained by mixing LSF powders (KUSAKA, 85 wt.%) and carbon powders (15 wt.%) in an organic vehicle composed of solvent, dispersant, and binder. After printing and drying, the cells were sintered at 1100 °C for 5 h to form porous LSF electrodes (with an active area of 0.28 cm^2). Three types of symmetrical cells with CGO, PrO_x , and the hybrid-catalyst (CGO+ PrO_x)-coated LSF electrodes, respectively, were prepared by infiltrating colloidal CGO solution, $\text{Pr}(\text{NO}_3)_3$ solution, and a mixture solution of colloidal CGO nanocrystals and $\text{Pr}(\text{NO}_3)_3$, into porous LSF backbones with subsequent calcination at 350 °C. Colloidal CGO was prepared by ultrasonically dispersing as-synthesized CGO nanocrystals in ethanol with polyethylene glycol (1 wt.%) as surfactant. [66] Pluronic P-123 surfactant (1.7 wt.%) was added into the $\text{Pr}(\text{NO}_3)_3$ solution. The mixture solution was obtained by mixing above colloidal CGO and $\text{Pr}(\text{NO}_3)_3$ solutions in molar ratio of 1:1.3. The loadings of these coatings were as adjusted to 9 wt.% relative to the porous LSF backbones after multiple infiltration cycles. The coatings were subsequently calcinated at 750 °C for 4 h during the cell start-up

stage to achieve the desired crystalline phases. The microstructure of four types of electrodes was examined using a Zeiss Merlin scanning electron microscope (SEM).

5.4.3 Fabrication of fuel-electrode-supported cells

The fuel-electrode-supported half cells with a configuration NiO/YSZ support | NiO/YSZ fuel electrode | YSZ electrolyte | CGO10 barrier were produced by laminating and co-sintering tape-cast green tapes, as previously reported. [152] The hybrid-catalyst-coated LSF oxygen electrode (with an area of 4 cm^2) was then applied to the CGO barrier using the same procedures as described previously for the preparation of symmetrical cells. The modification of Ni/YSZ fuel electrode with CGO electrocatalysts was performed by a pre-reduction procedure followed by the infiltration of CGO20 nitrate precursor solution containing stoichiometric amounts of $\text{Ce}(\text{NO}_3)_3$ and $\text{Gd}(\text{NO}_3)_3$ (4:1 molar ratio to metal ions), as previously reported. [127]

5.4.4 Electrochemical characterization

The electrochemical performance of these bare/coated LSF electrodes was assessed on symmetrical cells at 650–750 °C in air. The setup of symmetrical cell measurements can be found elsewhere. [74] The cells were heated to 750 °C with a heating rate of 1 °C min^{-1} and held for 4 h during the start-up. The electrochemical performance and durability of the fuel-electrode-supported cells were investigated both in fuel-cell and electrolysis modes using in-house constructed test rigs. [114] In fuel-cell mode, the cells were tested with 4% H_2O -96% H_2 fed to the fuel electrode and dry air to the oxygen electrode. In electrolysis mode, the cells were tested with 50% H_2O -50% H_2 fed to the fuel electrode and dry air to the oxygen electrode. EIS measurements were conducted using a Solartron 1255 frequency response analyzer in combination with a measurement resistor, at frequencies from 0.1 to 10 kHz with an amplitude of 3.75 mA cm^{-2} . All of EIS data analyses were carried out using the Python-based software Ravdav. [115]

5.4.5 Electrical conductivity relaxation (ECR) measurement

The surface exchange kinetics of bare and catalyst-coated LSF were evaluated by ECR measurement. Dense LSF bars were prepared by pressing, sintering, and polishing, as described in previous work. [168] Briefly, LSF powders were uniaxially pressed at 50 MPa followed by isostatically pressing at 300 MPa and sintering at 1200 °C for 4 h and further densification at 1150 °C for 16 h (the relative density > 98%). The sintered bars were ground by SiC sandpaper followed by gradual polishing with diamond paste (down to 1 μm diamond particle size) to the sample dimensions of approximately 1.5 × 1.5 × 19 mm³. Subsequently, the bars were ultrasonically cleaned in acetone, followed by ethanol and finally deionized water. The above infiltration solutions were coated on the entire polished surface in a similar manner as described above. The electrical conductivity was measured by the four-probe technique. The samples were heated to 750 °C with heating rate of 2 °C min⁻¹ and held for 4 h to calcine the coating. All the measurements were performed by changing pO₂ from 0.2 to 0.1 bar (reduction runs) and from 0.1 to 0.2 bar (oxidation runs). The gas pO₂ was varied by diluting the O₂ stream with N₂. A detailed description of ECR measurement and data fitting can be found in our previous work. [168]

Supplementary information

- SEM, EIS spectra, DRT results, ECR results

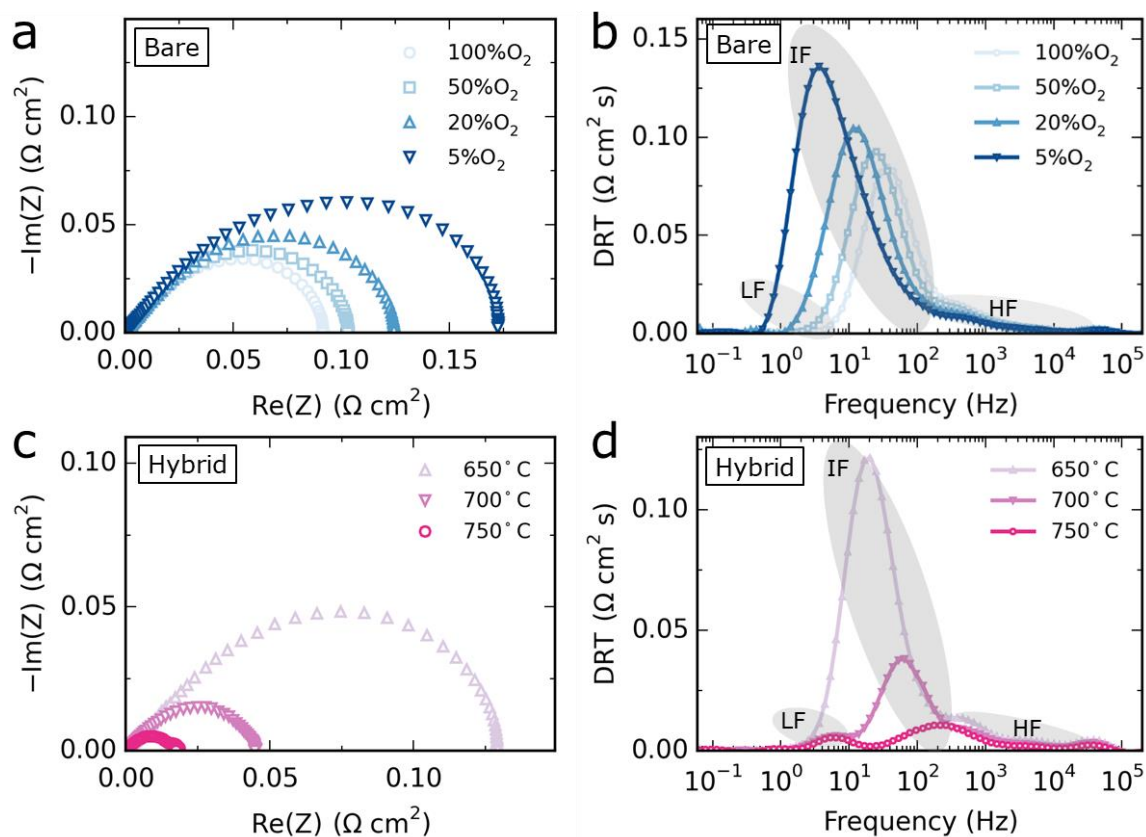


Figure 5.S1: Electrochemical performance on symmetrical cells. Effects of oxygen partial pressure ($p\text{O}_2$) on the EIS data of bare LSF electrodes at 750 °C: (a) Nyquist plots and (b) DRT plots. Effects of temperature on the EIS data of hybrid modified LSF electrodes in dry air: (c) Nyquist plots and (d) DRT plots.

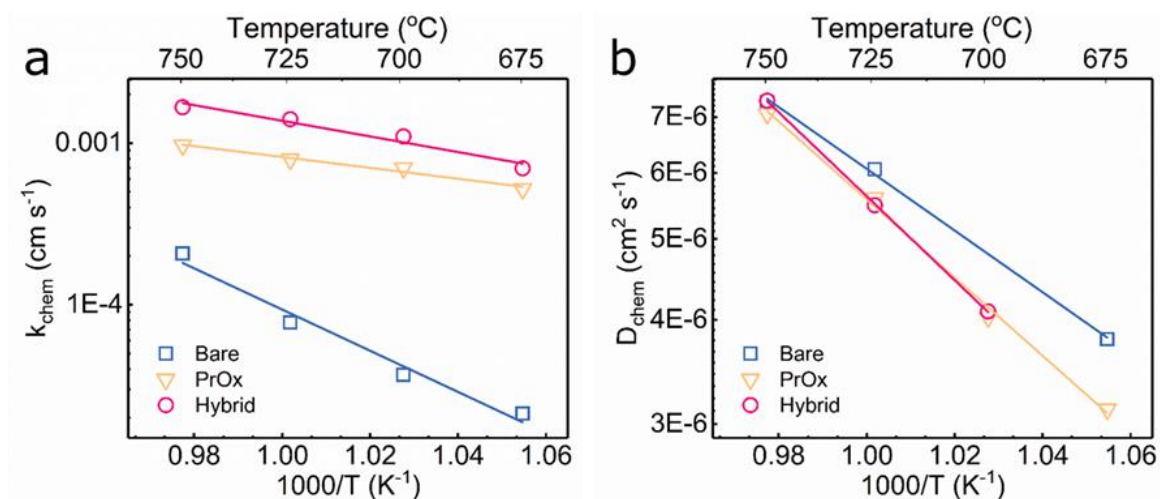


Figure 5.S2: (a) Surface exchange coefficient (k_{chem}) and (b) chemical diffusion coefficient (D_{chem}) of the bare LSF, PrOx-coated LSF, and hybrid-catalyst-coated LSF electrodes obtained from the ECR measurements.

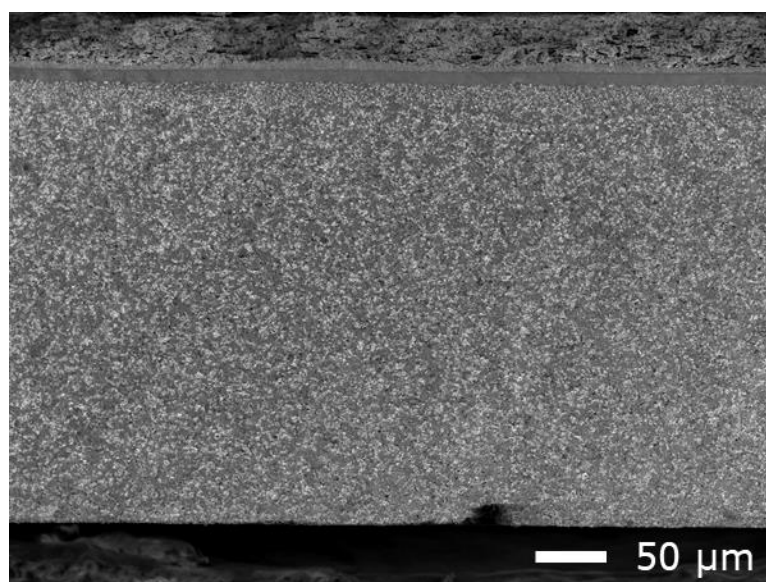


Figure 5.S3: Cross-sectional SEM images of fuel-electrode-supported cells with a configuration of Ni/YSZ support | Ni/YSZ fuel electrode | YSZ electrolyte | CGO barrier | hybrid-catalyst-coated LSF oxygen electrode (hybrid-catalyst-coated LSF cell).

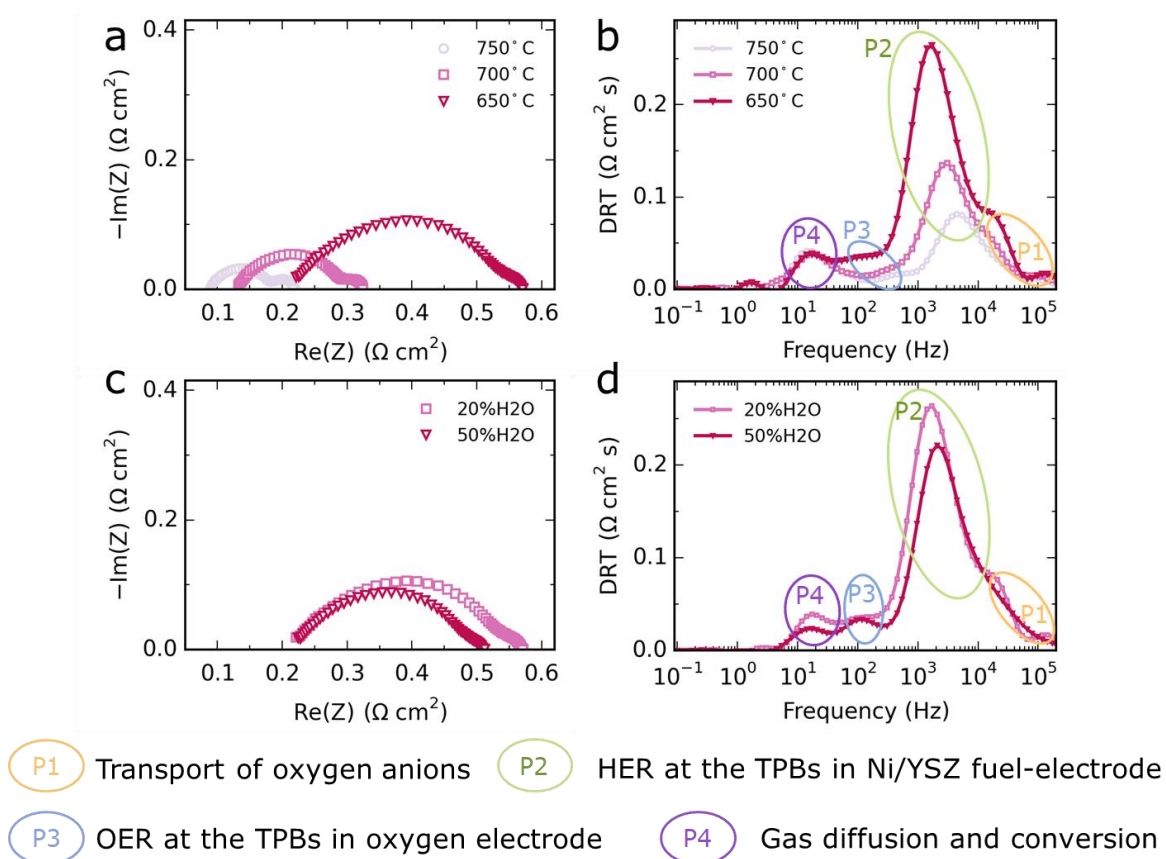


Figure 5.S4: EIS data on Ni/YSZ fuel-electrode-supported cells with the hybrid modified LSF oxygen electrode measured under OCV conditions. Effects of temperature on the EIS data: (a) Nyquist plots and (b) DRT plots. Effects of steam content in the fuel electrode on the EIS data: (c) Nyquist plots and (d) DRT plots.

CHAPTER 6

Conclusion and outlook

6.1 Conclusion

The SOC technology has shown potential in energy storage and conversion. One of the key components determining the performance and reliability of SOCs is the electrodes. The work presented in this thesis has centered around the development of advanced electrodes for intermediate-temperature SOCs. The performance, durability, cost, and scalability of the electrodes have been considered. The study is based on the use of infiltration to fabricate nanostructured electrodes. The experimental studies yielded the following notable results and discoveries.

- Large size ($12.5 \times 12.5 \text{ cm}^2$) fuel-electrode-supported SOCs with $\text{La}_{0.6}\text{Sr}_{0.4}\text{CoO}_{3-\delta}$ (LSC) infiltrated gadolinia-doped ceria (CGO) oxygen electrodes were prepared in **Chapter 2**. When examined at $4 \times 4 \text{ cm}^2$ level (active area), the resulting cell delivered favorable performance at $750 \text{ }^\circ\text{C}$ under high gas/steam utilization, e.g., a power density of 1.08 W cm^{-2} at 0.6 V in fuel cell mode and a current density of -1.07 A cm^{-2} at 1.3 V in electrolysis mode. The EIS results suggest that the LSC infiltrated CGO oxygen electrode has not only superior activity for both ORR and OER but also good durability when operated at -0.5 A cm^{-2} and $750 \text{ }^\circ\text{C}$ for steam electrolysis. Furthermore in **Chapter 3**, when tested at high current density of -1 A cm^{-2} at $750 \text{ }^\circ\text{C}$, the LSC infiltrated CGO oxygen electrode was also proved to be highly active and durable, showing the low R_{OER} resistance of $0.012 \text{ } \Omega \text{ cm}^2$ after 900 h operation and no obvious change in the microstructure. These results demonstrate the feasibility of using infiltration to produce nanostructured, well-performing oxygen electrodes for SOCs.

- Surface modification by coating nano-sized electrocatalysts via infiltration is an effective approach to enhance the durability of the most commonly used Ni/YSZ electrode during electrolysis operation (**Chapter 3**). For example, after modifying with CGO nano-catalysts, the degradation rate of the cell was reduced by a factor of ~ 22 , from 0.565 to 0.024 V kh^{-1} , when tested at -1.00 A cm^{-2} and 750 $^{\circ}\text{C}$ for steam electrolysis. Post-test microstructural analysis reveals that the introduced CGO coating effectively mitigates the microstructural deterioration (typically disconnection between Ni and YSZ at the TPBs) seen on non-modified Ni/YSZ electrodes under the same testing condition.
- By well controlling the conditions such as temperature and gas composition, one single atmosphere can be utilized to reduce the NiO in the fuel electrode of a full cell to Ni thus creating enough porosity for infiltration, at the same time making no harm to the oxygen electrode side as well as the barrier layer (**Chapter 4**). Benefit from this finding, the aforementioned infiltration approach was further simplified to fit the upscaling requirement, by replacing the complicated “two-atmosphere-reduction” procedure (i.e., the fuel electrode side is exposed to reducing atmosphere while the oxygen electrode is exposed to air) with a facile “one-atmosphere-reduction”, which can well be carried out during the cooling of the cell after the final sintering step. Based on this simplified approach, the infiltrated cell exhibited significantly enhanced long-term durability at high current densities, with cell voltage degradation rates of 0.028 V kh^{-1} (2% kh^{-1}) at -1.25 A cm^{-2} and 0.010 V kh^{-1} (0.8% kh^{-1}) at -1.00 A cm^{-2} for steam electrolysis at 750 $^{\circ}\text{C}$. These degradation rates are ~ 14 times and ~ 25 times smaller than those of the non-infiltrated cell, respectively. The infiltrated cell also showed superior durability to the non-infiltrated cell during reversible operation at ± 0.50 A cm^{-2} and ± 1.00 A cm^{-2} .
- By applying the infiltration in a novel manner, not only the composition of the introduced coating but also the morphology of coating can be well controlled (**Chapter 5**). Considering that cobalt-containing materials often suffer from various problems when employed as oxygen electrodes and the high cost of cobalt, a highly active and robust $\text{La}_{0.6}\text{Sr}_{0.4}\text{FeO}_{3-\delta}$ (LSF)-based oxygen electrode was developed by applying a nanoengineered hybrid catalyst coating composed of nanoparticles of

CGO and PrO_x . Different from the conventional infiltration with a precursor of metal nitrate, here a mixture solution of colloidal CGO nanocrystals and $\text{Pr}(\text{NO}_3)_3$ was used for infiltration to enable this designed nanoengineered architecture. The resulting hybrid-catalyst coated LSF electrode displayed a very low R_p of $0.017 \Omega \text{ cm}^2$ at $750 \text{ }^\circ\text{C}$. Applying this oxygen electrode on a CGO-modified Ni/YSZ fuel-electrode-supported cell, stable operation at $650 \text{ }^\circ\text{C}$ under -0.5 A cm^{-2} with a cell voltage close to 1.3 V was achieved.

In summary, the findings reported in this thesis demonstrate the potential of designing high-performance and robust SOCs by nanoengineering electrodes through infiltration and have significant implications for the practical integration of the SOC technology into the future sustainable energy system.

6.2 Outlook

While this work has achieved several important advances toward the development of high-performance and stable SOCs, there is of course much more work to be done. Possible directions for future studies can be:

- Reducing the ohmic resistance (R_{ohm}) of the cell to further improve performance – The EIS results showed that the R_{ohm} values of the fuel-electrode-supported cells reported in this thesis are higher than expected. For example, the cell developed in **Chapter 2** demonstrated a R_{ohm} of $0.25 \Omega \text{ cm}^2$ at $700 \text{ }^\circ\text{C}$ with 50% H_2O -50% H_2 fed to the fuel electrode. This R_{ohm} is 5 times higher than that of expected resistance ($\sim 0.05 \Omega \text{ cm}^2$) for $5 \mu\text{m}$ thick YSZ electrolyte and $6 \mu\text{m}$ thick CGO barrier based upon the ionic conductivities of 0.02 S cm^{-1} for YSZ and 0.03 S cm^{-1} for CGO [117]. This can be attributed to the interdiffusion of elements at the YSZ electrolyte – CGO barrier interface during the co-sintering process leading to the formation of solid solution phases with lower ionic conductivity [118-120]. Furthermore, the R_{ohm} actually constitutes $\sim 60 \%$ of the overall resistance ($0.43 \Omega \text{ cm}^2$), and the R_p is only $0.18 \Omega \text{ cm}^2$. In addition, for the cell reported in **Chapter 5** with the hybrid-catalyst

coated LSF oxygen electrode and the CGO-modified Ni/YSZ fuel-electrode, the measured R_{ohm} is also higher than R_p and constitute more than 50 % of the total resistance at a temperature range of 650–750 °C with 50% H₂O-50% H₂ fed to the fuel electrode. These results suggest that there is still room for further improvement of the cell performance by reducing R_{ohm} . This may be achieved by the following approaches: i) limiting the YSZ – CGO inter-diffusion via, e.g., lowering the sintering temperature, or more preferably sintering the half-cell (NiO/YSZ support | NiO/YSZ fuel electrode | YSZ electrolyte) first and then sintering the CGO barrier layer at lower temperature, such as <1200 °C; ii) reducing the thickness of electrolyte and barrier layer; iii) introducing a better oxygen ion conducting electrolyte materials like scandium-stabilized zirconia (SSZ).

- Further insights into the degradation mechanism of Ni/YSZ electrode during electrolysis operation and the effects of CGO modification – This may be achieved by preparing the model electrodes and applying in operando experiments on the electrodes to investigate active surface oxidation state and composition of electrode materials under electrolysis conditions, such as using ambient pressure X-ray photoelectron and near edge X-ray absorption fine structure spectroscopies (APXPS and NEXAFS, respectively). Combining with theoretical calculation based on density functional theory (DFT) may also be a good choice.
- More thorough optimization of the infiltration – Noted that the observed performance and durability of cells developed in this thesis were achieved without the optimization of the basic infiltration parameters such as catalyst loading and heat treatment temperature. For example, the R_p of the hybrid-catalyst-coated LSF electrode (in **Chapter 5**) may be further decreased by using CGO nanocrystals with smaller size or optimizing the component ratio or loading of the hybrid catalyst.

Bibliography

- [1] International energy outlook 2019 database, US Energy Information Administration (EIA), https://www.eia.gov/outlooks/ieo/tables_ref.php, (2019).
- [2] Global Energy & CO2 Status Report, International Energy Agency: Paris, France, (2019).
- [3] H.E. Murdock, Gibb, D., André, T., Appavou, F., Brown, A., Epp, B., Kondev, B., McCrone, A., Musolino, E., Ranalder, L. and Sawin, J.L., Renewables 2019 Global Status Report, (2019).
- [4] T.M. Gür, Energy Environ. Sci., 11 (2018) 2696-2767.
- [5] C. Duan, R. Kee, H. Zhu, N. Sullivan, L. Zhu, L. Bian, D. Jennings, R. O'Hayre, Nat. Energy, 4 (2019) 230-240.
- [6] J.T.S. Irvine, D. Neagu, M.C. Verbraeken, C. Chatzichristodoulou, C. Graves, M.B. Mogensen, Nat. Energy, 1 (2016) 15014.
- [7] C. Graves, S.D. Ebbesen, S.H. Jensen, S.B. Simonsen, M.B. Mogensen, Nat. Mater., 14 (2015) 239-244.
- [8] S. Choi, T.C. Davenport, S.M. Haile, Energy Environ. Sci., 12 (2019) 206-215.
- [9] N. Ai, N. Li, S. He, Y. Cheng, M. Saunders, K. Chen, T. Zhang, S.P. Jiang, J. Mater. Chem. A, 5 (2017) 12149-12157.
- [10] Q. Fu, C. Mabilat, M. Zahid, A. Brisse, L. Gautier, Energy Environ. Sci., 3 (2010) 1382.
- [11] A. Galadima, O. Muraza, Journal of Natural Gas Science and Engineering, 25 (2015) 303-316.
- [12] J.W. Fergus, J Power Sources, 162 (2006) 30-40.
- [13] E.D. Wachsman, K.T. Lee, Science, 334 (2011) 935-939.
- [14] J. Hartvigsen, S. Elangovan, J. O'Brien, C. Stoots, J.S. Herring, P. Lessing, in: 6th European Solid Oxide Fuel Cell Forum, Lucerne, Switzerland, 2004, pp. 378-387.
- [15] K.F. Chen, N. Ai, S.P. Jiang, Int. J. Hydrogen Energy, 37 (2012) 10517-10525.
- [16] Y.K. Tao, S.D. Ebbesen, M.B. Mogensen, J Power Sources, 328 (2016) 452-462.
- [17] M.A. Laguna-Bercero, J.A. Kilner, S.J. Skinner, Chem. Mater., 22 (2010) 1134-1141.
- [18] J. Kim, H.I. Ji, H.P. Dasari, D. Shin, H. Song, J.H. Lee, B.K. Kim, H.J. Je, H.W. Lee, K.J. Yoon, Int. J. Hydrogen Energy, 38 (2013) 1225-1235.

- [19] G.A. Hughes, J.G. Railsback, K.J. Yakal-Kremiski, D.M. Butts, S.A. Barnett, *Faraday Discuss.*, 182 (2015) 365-377.
- [20] G.A. Hughes, K. Yakal-Kremiski, S.A. Barnett, *Phys Chem Chem Phys*, 15 (2013) 17257-17262.
- [21] R. Knibbe, M.L. Traulsen, A. Hauch, S.D. Ebbesen, M. Mogensen, *J. Electrochem. Soc.*, 157 (2010) B1209-B1217.
- [22] M. Keane, M.K. Mahapatra, A. Verma, P. Singh, *Int. J. Hydrogen Energy*, 37 (2012) 16776-16785.
- [23] M.J. Lopez-Robledo, M.A. Laguna-Bercero, A. Larrea, V.M. Orera, *J Power Sources*, 378 (2018) 184-189.
- [24] W. Wang, M. Mogensen, *Solid State Ionics*, 176 (2005) 457-462.
- [25] G.M. Rupp, A.K. Opitz, A. Nenning, A. Limbeck, J. Fleig, *Nat Mater*, 16 (2017) 640-645.
- [26] F. He, T. Wu, R. Peng, C. Xia, *J Power Sources*, 194 (2009) 263-268.
- [27] Z. Shao, S.M. Haile, *Nature*, 431 (2004) 170-173.
- [28] A. Jun, J. Kim, J. Shin, G. Kim, *Angew. Chem. Int. Ed.*, 55 (2016) 12512-12515.
- [29] S.-i. Lee, J. Kim, J.-W. Son, J.-H. Lee, B.-K. Kim, H.-J. Je, H.-W. Lee, H. Song, K.J. Yoon, *J Power Sources*, 250 (2014) 15-20.
- [30] B. Koo, K. Kim, J.K. Kim, H. Kwon, J.W. Han, W. Jung, *Joule*, 2 (2018) 1476-1499.
- [31] A.U. Rehman, M. Li, R. Knibbe, M.S. Khan, V.K. Peterson, H.E.A. Brand, Z. Li, W. Zhou, Z. Zhu, *ACS Appl Mater Interfaces*, 11 (2019) 26909-26919.
- [32] Y.L. Huang, A.M. Hussain, I.A. Robinson, E.D. Wachsman, *ACS Appl Mater Interfaces*, 10 (2018) 28635-28643.
- [33] N. Tsvetkov, Q. Lu, L. Sun, E.J. Crumlin, B. Yildiz, *Nat Mater*, 15 (2016) 1010-1016.
- [34] M.A. Laguna-Bercero, H. Monzón, A. Larrea, V.M. Orera, *J. Mater. Chem. A*, 4 (2016) 1446-1453.
- [35] Y.-S. Yoo, M. Choi, J.-H. Hwang, H.N. Im, B. Singh, S.-J. Song, *Ceramics International*, 41 (2015) 6448-6454.
- [36] B. Philippeau, F. Mauvy, C. Mazataud, S. Fourcade, J.-C. Grenier, *Solid State Ionics*, 249-250 (2013) 17-25.
- [37] T. Ogier, F. Mauvy, J.-M. Bassat, J. Laurencin, J. Mougín, J.-C. Grenier, *Int. J. Hydrogen Energy*, 40 (2015) 15885-15892.
- [38] X. Tong, F. Zhou, S. Yang, S. Zhong, M. Wei, Y. Liu, *Ceramics International*, (2017).
- [39] M. Trini, A. Hauch, S. Angelis, X. Tong, P.V. Hendriksen, M. Chen, unpublished work.

- [40] X. Sun, M. Chen, Y.L. Liu, P.V. Hendriksen, *ECS Trans.*, 68 (2015) 3359-3368.
- [41] J.T.S. Irvine, D. Neagu, M.C. Verbraeken, C. Chatzichristodoulou, C. Graves, M.B. Mogensen, *Nat. Energy*, 1 (2016) 15014.
- [42] M. Chen, Y.L. Liu, J.J. Bentzen, W. Zhang, X. Sun, A. Hauch, Y. Tao, J.R. Bowen, P.V. Hendriksen, *J. Electrochem. Soc.*, 160 (2013) F883-F891.
- [43] M. Chen, X. Sun, C. Chatzichristodoulou, S. Koch, P.V. Hendriksen, M.B. Mogensen, *ECS Trans.*, 78 (2017) 3077-3088.
- [44] A. Hauch, K. Brodersen, M. Chen, M.B. Mogensen, *Solid State Ionics*, 293 (2016) 27-36.
- [45] D. The, S. Grieshammer, M. Schroeder, M. Martin, M. Al Daroukh, F. Tietz, J. Schefold, A. Brisse, *J Power Sources*, 275 (2015) 901-911.
- [46] A. Hauch, M. Marchese, A. Lanzini, C. Graves, *J Power Sources*, 377 (2018) 110-120.
- [47] P. Hjalmarrsson, X. Sun, Y.-L. Liu, M. Chen, *J Power Sources*, 262 (2014) 316-322.
- [48] A. Nechache, B.A. Boukamp, M. Cassir, A. Ringuedé, *J Solid State Electr*, 23 (2018) 109-123.
- [49] F. Tietz, D. Sebold, A. Brisse, J. Schefold, *J Power Sources*, 223 (2013) 129-135.
- [50] S. Ovtar, X. Tong, J.J. Bentzen, K.T.S. Thyden, S.B. Simonsen, M. Chen, *Nanoscale*, 11 (2019) 4394-4406.
- [51] A. Hauch, S.r.H.j. Jensen, J.r.B. Bilde-Sørensen, M. Mogensen, *J. Electrochem. Soc.*, 154 (2007) A619.
- [52] S.D. Ebbesen, C. Graves, A. Hauch, S.r.H. Jensen, M. Mogensen, *J. Electrochem. Soc.*, 157 (2010) B1419.
- [53] K. Lillmaa, M. Maide, R. Kanarbik, G. Nurk, E. Lust, *J. Electrochem. Soc.*, 163 (2016) F3190-F3196.
- [54] X. Yang, J.T.S. Irvine, *J Mater Chem*, 18 (2008) 2349.
- [55] C. Jin, C.H. Yang, F. Zhao, D. Cui, F.L. Chen, *Int. J. Hydrogen Energy*, 36 (2011) 3340-3346.
- [56] S. Li, Y. Li, Y. Gan, K. Xie, G. Meng, *J Power Sources*, 218 (2012) 244-249.
- [57] G. Tsekouras, D. Neagu, J.T.S. Irvine, *Energy Environ. Sci.*, 6 (2013) 256-266.
- [58] J.H. Myung, D. Neagu, D.N. Miller, J.T. Irvine, *Nature*, 537 (2016) 528-531.
- [59] Y. Wang, T. Liu, M. Li, C. Xia, B. Zhou, F. Chen, *J. Mater. Chem. A*, 4 (2016) 14163-14169.
- [60] Y.H. Li, P. Li, B.B. Hu, C.R. Xia, *J. Mater. Chem. A*, 4 (2016) 9236-9243.
- [61] P.A. Connor, X.L. Yue, C.D. Savaniu, R. Price, G. Triantafyllou, M. Cassidy, G. Kerherve, D.J. Payne, R.C. Maher, L.F. Cohen, R.I. Tomov, B.A. Glowacki, R.V. Kumar, J.T.S. Irvine, *Adv. Energy Mater.*, 8 (2018) 1800120.

- [62] J.M. Vohs, R.J. Gorte, *Adv. Mater.*, 21 (2009) 943-956.
- [63] D. Ding, X.X. Li, S.Y. Lai, K. Gerdes, M.L. Liu, *Energy Environ. Sci.*, 7 (2014) 552-575.
- [64] Z. Zhan, D. Han, T. Wu, X. Ye, S. Wang, T. Wen, S. Cho, S.A. Barnett, *Rsc Adv*, 2 (2012) 4075.
- [65] H. Da, X. Liu, F. Zeng, J. Qian, T. Wu, Z. Zhan, *Scientific reports*, 2 (2012) 462.
- [66] X. Tong, T. Luo, X. Meng, H. Wu, J. Li, X. Liu, X. Ji, J. Wang, C. Chen, Z. Zhan, *Small*, 11 (2015) 5581-5588.
- [67] A.J. Samson, M. Sogaard, N. Bonanos, *Electrochem Solid St*, 15 (2012) B54-B56.
- [68] R. Küngas, F. Bidrawn, J.M. Vohs, R.J. Gorte, *Electrochem. Solid-State Lett.*, 13 (2010) B87.
- [69] A.J. Samson, M. Sjøgaard, P. Hjalmarsen, J. Hjelm, N. Bonanos, S.P.V. Foghmoes, T. Ramos, *Fuel Cells*, 13 (2013) 511-519.
- [70] A. Chrzan, S. Ovtar, P. Jasinski, M. Chen, A. Hauch, *J Power Sources*, 353 (2017) 67-76.
- [71] A.J. Samson, P. Hjalmarsen, M. Sjøgaard, J. Hjelm, N. Bonanos, *J Power Sources*, 216 (2012) 124-130.
- [72] Y. Huang, K. Ahn, J.M. Vohs, R.J. Gorte, *J. Electrochem. Soc.*, 151 (2004) A1592.
- [73] Y. Huang, J.M. Vohs, R.J. Gorte, *J. Electrochem. Soc.*, 151 (2004) A646.
- [74] A. Samson, M. Sjøgaard, R. Knibbe, N. Bonanos, *J. Electrochem. Soc.*, 158 (2011) B650.
- [75] S. Ovtar, M. Chen, A.J. Samson, R. Kiebach, *Solid State Ionics*, 304 (2017) 51-59.
- [76] Y. Chen, S. Yoo, K. Pei, D. Chen, L. Zhang, B. deGlee, R. Murphy, B. Zhao, Y. Zhang, Y. Chen, M. Liu, *Adv. Funct. Mater.*, 28 (2018) 1704907.
- [77] Y. Chen, S. Yoo, Y. Choi, J.H. Kim, Y. Ding, K. Pei, R. Murphy, Y.X. Zhang, B.T. Zhao, W.L. Zhang, H.J. Chen, Y. Chen, W. Yuan, C.H. Yang, M.L. Liu, *Energy Environ. Sci.*, 11 (2018) 2458-2466.
- [78] Y. Chen, Y. Chen, D. Ding, Y. Ding, Y. Choi, L. Zhang, S. Yoo, D. Chen, B. deGlee, H. Xu, Q. Lu, B. Zhao, G. Vardar, J. Wang, H. Bluhm, E.J. Crumlin, C. Yang, J. Liu, B. Yildiz, M. Liu, *Energy Environ. Sci.*, 10 (2017) 964-971.
- [79] Y. Chen, Y.M. Choi, S. Yoo, Y. Ding, R.Q. Yan, K. Pei, C. Qu, L. Zhang, I. Chang, B.T. Zhao, Y.X. Zhang, H.J. Chen, Y. Chen, C.H. Yang, B. deGlee, R. Murphy, J. Liu, M.L. Liu, *Joule*, 2 (2018) 938-949.
- [80] Y.-L. Huang, A.M. Hussain, E.D. Wachsman, *Nano Energy*, 49 (2018) 186-192.
- [81] K. Joong Yoon, M. Biswas, H.-J. Kim, M. Park, J. Hong, H. Kim, J.-W. Son, J.-H. Lee, B.-K. Kim, H.-W. Lee, *Nano Energy*, 36 (2017) 9-20.

- [82] Instruments, Gamry, Complex impedance in Corrosion, (2007) 1-30.
- [83] A. Nechache, M. Cassir, A. Ringuede, *J Power Sources*, 258 (2014) 164-181.
- [84] A. Leonide, V. Sonn, A. Weber, E. Ivers-Tiffée, *J. Electrochem. Soc.*, 155 (2008) B36.
- [85] H. Schichlein, A.C. Muller, M. Voigts, A. Krugel, E. Ivers-Tiffée, *Journal of Applied Electrochemistry*, 32 (2002) 875-882.
- [86] V. Sonn, A. Leonide, E. Ivers-Tiffée, *J. Electrochem. Soc.*, 155 (2008) B675.
- [87] A. Hauch, S.H. Jensen, S. Ramousse, M. Mogensen, *J. Electrochem. Soc.*, 153 (2006) A1741.
- [88] M.A. Laguna-Bercero, R. Campana, A. Larrea, J.A. Kilner, V.M. Orera, *Fuel Cells*, 11 (2011) 116-123.
- [89] C. Yang, J. Li, J. Newkirk, V. Baish, R. Hu, Y. Chen, F. Chen, *J. Mater. Chem. A*, 3 (2015) 15913-15919.
- [90] C.H. Yang, A. Coffin, F.L. Chen, *Int. J. Hydrogen Energy*, 35 (2010) 3221-3226.
- [91] P. Kim-Lohsoontorn, D.J.L. Brett, N. Laosiripojana, Y.M. Kim, J.M. Bae, *Int. J. Hydrogen Energy*, 35 (2010) 3958-3966.
- [92] N. Zhou, Y.-M. Yin, J. Li, L. Xu, Z.-F. Ma, *J Power Sources*, 340 (2017) 373-379.
- [93] Z. Zhan, W. Kobsiriphat, J.R. Wilson, M. Pillai, I. Kim, S.A. Barnett, *Energy Fuels*, 23 (2009) 3089-3096.
- [94] S.D. Ebbesen, S.H. Jensen, A. Hauch, M.B. Mogensen, *Chemical reviews*, 114 (2014) 10697-10734.
- [95] A.R. Hanifi, M.A. Laguna-Bercero, N.K. Sandhu, T.H. Etsell, P. Sarkar, *Scientific reports*, 6 (2016) 27359.
- [96] S.-L. Zhang, H. Wang, M.Y. Lu, A.-P. Zhang, L.V. Mogni, Q. Liu, C.-X. Li, C.-J. Li, S.A. Barnett, *Energy Environ. Sci.*, 11 (2018) 1870-1879.
- [97] X. Meng, Y. Shen, M. Xie, Y. Yin, N. Yang, Z.-F. Ma, J.C. Diniz da Costa, S. Liu, *J Power Sources*, 306 (2016) 226-232.
- [98] K. Hosoi, T. Sakai, S. Ida, T. Ishihara, *Electrochim. Acta*, 194 (2016) 473-479.
- [99] G. Tsekouras, J.T.S. Irvine, *J Mater Chem*, 21 (2011) 9367.
- [100] Q.A. Liu, C.H. Yang, X.H. Dong, F.L. Chen, *Int. J. Hydrogen Energy*, 35 (2010) 10039-10044.
- [101] C. Yang, Z. Yang, C. Jin, M. Liu, F. Chen, *Int. J. Hydrogen Energy*, 38 (2013) 11202-11208.
- [102] F. Bidrawn, G. Kim, G. Corre, J.T.S. Irvine, J.M. Vohs, R.J. Gorte, *Electrochem. Solid-State Lett.*, 11 (2008) B167.
- [103] K. Hosoi, H. Hagiwara, S. Ida, T. Ishihara, *J. Phys. Chem. C*, 120 (2016) 16110-16117.

- [104] L.J. Zhang, X.B. Zhu, Z.Q. Cao, Z.H. Wang, W.Y. Li, L. Zhu, P.Z. Li, X.Q. Huang, Z. Lu, *Electrochim. Acta*, 232 (2017) 542-549.
- [105] R. Xing, Y. Wang, S. Liu, C. Jin, *J Power Sources*, 208 (2012) 276-281.
- [106] M. Torrell, S. Garcia-Rodriguez, A. Morata, G. Penelas, A. Tarancon, *Faraday discussions*, 182 (2015) 241-255.
- [107] S. Chu, A. Majumdar, *Nature*, 488 (2012) 294-303.
- [108] V.A.C. Haanappel, J. Mertens, D. Rutenbeck, C. Tropartz, W. Herzhof, D. Sebold, F. Tietz, *J Power Sources*, 141 (2005) 216-226.
- [109] T. Tsai, S.A. Barnett, *Solid State Ionics*, 93 (1997) 207-217.
- [110] C. Nicollet, A. Flura, V. Vibhu, A. Rougier, J.-M. Bassat, J.-C. Grenier, *Int. J. Hydrogen Energy*, 41 (2016) 15538-15544.
- [111] H. Fan, M. Keane, N. Li, D. Tang, P. Singh, M. Han, *Int. J. Hydrogen Energy*, 39 (2014) 14071-14078.
- [112] J. Chen, F. Liang, D. Yan, J. Pu, B. Chi, S.P. Jiang, L. Jian, *J Power Sources*, 195 (2010) 5201-5205.
- [113] S. Ovtar, A. Hauch, S. Veltzé, M. Chen, *Electrochim. Acta*, 266 (2018) 293-304.
- [114] S.D. Ebbesen, C. Graves, A. Hauch, S.H. Jensen, M. Mogensen, *J. Electrochem. Soc.*, 157 (2010) B1419-B1429.
- [115] C. Graves, Ravdav, *Data Analysis Software*, Ver 0.97, 2012.
- [116] S. Liu, Q. Liu, J.-L. Luo, *Acs Catal*, 6 (2016) 6219-6228.
- [117] A. Tsoga, *Solid State Ionics*, 135 (2000) 403-409.
- [118] A. Tsoga, A. Gupta, A. Naoumidis, P. Nikolopoulos, *Acta Mater.*, 48 (2000) 4709-4714.
- [119] A. Tsoga, A. Naoumidis, A. Gupta, D. Stöver, *Mater. Sci. Forum*, 308-311 (1999) 794-799.
- [120] H. Xu, K. Cheng, M. Chen, L. Zhang, K. Brodersen, Y. Du, *J Power Sources*, 441 (2019) 227152.
- [121] H. Fan, M. Han, *Faraday Discuss.*, 182 (2015) 477-491.
- [122] A. Chrzan, S. Ovtar, P. Jasinski, M. Chen, A. Hauch, *J Power Sources*, 353 (2017) 67-76.
- [123] T. Chen, M. Liu, C. Yuan, Y. Zhou, X. Ye, Z. Zhan, C. Xia, S. Wang, *J Power Sources*, 276 (2015) 1-6.
- [124] C. Graves, S.D. Ebbesen, M. Mogensen, *Solid State Ionics*, 192 (2011) 398-403.
- [125] P. Hjalmarsson, X. Sun, Y.-L. Liu, M. Chen, *J Power Sources*, 223 (2013) 349-357.

- [126] A. Hauch, S.D. Ebbesen, S.H. Jensen, M. Mogensen, J. Electrochem. Soc., 155 (2008) B1184.
- [127] X. Tong, S. Ovtar, K. Brodersen, P.V. Hendriksen, M. Chen, ACS Appl Mater Interfaces, 11 (2019) 25996-26004.
- [128] M.B. Mogensen, A. Hauch, X. Sun, M. Chen, Y. Tao, S.D. Ebbesen, K.V. Hansen, P.V. Hendriksen, Fuel Cells, (2017).
- [129] M.P. Hoerlein, M. Riegraf, R. Costa, G. Schiller, K.A. Friedrich, Electrochim. Acta, 276 (2018) 162-175.
- [130] M. Trini, P.S. Jørgensen, A. Hauch, J.J. Bentzen, P.V. Hendriksen, M. Chen, J. Electrochem. Soc., 166 (2019) F158-F167.
- [131] G. Glenk, S. Reichelstein, Nat. Energy, 4 (2019) 216-222.
- [132] M.A. Laguna-Bercero, J Power Sources, 203 (2012) 4-16.
- [133] S.D. Ebbesen, X. Sun, M.B. Mogensen, Faraday Discuss., 182 (2015) 393-422.
- [134] J. Paier, C. Penschke, J. Sauer, Chem. Rev., 113 (2013) 3949-3985.
- [135] C.B. Gopal, F. El Gabaly, A.H. McDaniel, W.C. Chueh, Adv. Mater., 28 (2016) 4692-4697.
- [136] C.W. Sun, H. Li, L.Q. Chen, Energy Environ. Sci., 5 (2012) 8475-8505.
- [137] C. Yang, Z. Yang, C. Jin, M. Liu, F. Chen, Int. J. Hydrogen Energy, 38 (2013) 11202-11208.
- [138] Y. Tan, A. Wang, L. Jia, D. Yan, B. Chi, J. Pu, J. Li, Int. J. Hydrogen Energy, 42 (2017) 4456-4464.
- [139] R. Barfod, M. Mogensen, T. Klemenso, A. Hagen, Y.L. Liu, P.V. Hendriksen, J. Electrochem. Soc., 154 (2007) B371-B378.
- [140] S.H. Jensen, A. Hauch, P.V. Hendriksen, M. Mogensen, J. Electrochem. Soc., 156 (2009) B757-B764.
- [141] T. Wood, H. He, T. Joia, K. Mark, D. Steedman, E. Tang, C. Brown, K. Luc, in: 12th European SOFC & SOE Forum, Lucerne/Switzerland, 2016, pp. 184-191.
- [142] A. Leonide, V. Sonn, A. Weber, E. Ivers-Tiffée, J. Electrochem. Soc., 155 (2008) B36-B41.
- [143] X. Zhang, L. Liu, Z. Zhao, B. Tu, D. Ou, D. Cui, X. Wei, X. Chen, M. Cheng, Nano Lett., 15 (2015) 1703-1709.
- [144] K.V. Hansen, M. Chen, T. Jacobsen, K. Thydén, S.B. Simonsen, S. Koch, M.B. Mogensen, J. Electrochem. Soc., 163 (2016) F1217-F1227.
- [145] K. Thyden, Solid State Ionics, 178 (2008) 1984-1989.
- [146] A. Le Gal, S. Abanades, J. Phys. Chem. C, 116 (2012) 13516-13523.
- [147] T. Wu, Q. Deng, H.A. Hansen, T. Vegge, J. Phys. Chem. C, 123 (2019) 5507-5517.

- [148] W.C. Chueh, C. Falter, M. Abbott, D. Scipio, P. Furler, S.M. Haile, A. Steinfeld, *Science*, 330 (2010) 1797-1801.
- [149] V. Papaefthimiou, D.K. Niakolas, F. Paloukis, D. Teschner, A. Knop-Gericke, M. Haevecker, S. Zafeiratos, *J. Catal.*, 352 (2017) 305-313.
- [150] X. Xu, W. Wang, W. Zhou, Z. Shao, *Small Methods*, 2 (2018) 1800071.
- [151] R. Kiebach, P. Zielke, J.V.T. Høgh, K. Thydén, H.J. Wang, R. Barford, P.V. Hendriksen, *Fuel Cells*, 16 (2016) 80-88.
- [152] A. Hagen, M. Menon, R. Barford, P.V. Hendriksen, S. Ramousse, P.H. Larsen, *Fuel Cells*, 6 (2006) 146-150.
- [153] B.A. Boukamp, A. Rolle, *Solid State Ionics*, 314 (2018) 103-111.
- [154] M.B. Mogensen, S.D. Ebbesen, S.H. Jensen, X. Sun, A. Hauch, M. Chen, *ECS Trans.*, 78 (2017) 2133-2139.
- [155] P.V. Hendriksen, X.F. Tong, M. Chen, S. Ovtar, H.L. Frandsen, P. Khajavi, K. R., in 13th European SOFC & SOE Forum, A1506, Lucerne/Switzerland, (2018).
- [156] N.A. Baharuddin, A. Muchtar, M.R. Somalu, *Int. J. Hydrogen Energy*, 42 (2017) 9149-9155.
- [157] G. Yang, W. Zhou, M. Liu, Z. Shao, *ACS Appl Mater Interfaces*, 8 (2016) 35308-35314.
- [158] Y. Niu, J. Sunarso, F. Liang, W. Zhou, Z. Zhu, Z. Shao, *J. Electrochem. Soc.*, 158 (2011) B132.
- [159] Y. Chen, Y. Bu, Y. Zhang, R. Yan, D. Ding, B. Zhao, S. Yoo, D. Dang, R. Hu, C. Yang, M. Liu, *Adv. Energy Mater.*, 7 (2017) 1601890.
- [160] J.G. Lee, J.H. Park, Y.G. Shul, *Nat Commun*, 5 (2014) 4045.
- [161] Y. Chen, S. Yoo, X. Li, D. Ding, K. Pei, D. Chen, Y. Ding, B. Zhao, R. Murphy, B. deGlee, J. Liu, M. Liu, *Nano Energy*, 47 (2018) 474-480.
- [162] D. Ding, M. Liu, Z. Liu, X. Li, K. Blinn, X. Zhu, M. Liu, *Adv. Energy Mater.*, 3 (2013) 1149-1154.
- [163] E. Dogdibegovic, R. Wang, G.Y. Lau, A. Karimaghloo, M.H. Lee, M.C. Tucker, *J Power Sources*, 437 (2019) 226935.
- [164] Y. Xu, N. Farandos, M. Rosa, P. Zielke, V. Esposito, P. Vang Hendriksen, S.H. Jensen, T. Li, G. Kelsall, R. Kiebach, *International Journal of Applied Ceramic Technology*, 15 (2018) 315-327.
- [165] G. Perin, C. Gadea, M. Rosa, S. Sanna, Y. Xu, R. Kiebach, A. Glisenti, V. Esposito, *J Phys Chem Solids*, 132 (2019) 162-171.
- [166] X. Ding, W. Zhu, G. Hua, J. Li, Z. Wu, *Electrochim. Acta*, 163 (2015) 204-212.

[167] Y. Chen, S. Yoo, W. Zhang, J.H. Kim, Y. Zhou, K. Pei, N. Kane, B. Zhao, R. Murphy, Y. Choi, M. Liu, *Acs Catal*, (2019) 7137-7142.

[168] Đ. Tripković, R. Küngas, M.B. Mogensen, P.V. Hendriksen, *J. Mater. Chem. A*, 7 (2019) 11782-11791.